NASA CR-152072

LOW SPEED TEST OF A HIGH-BYPASS-RATIO PROPULSION SYSTEM WITH AN ASYMMETRIC INLET DESIGNED FOR A TILT-NACELLE V/STOL AIRPLANE

(NASA-CR-152072) LOW SPEED TEST OF A HIGH-BYPASS-RATIO PROPULSION SYSTEM WITH AN ASYMMETRIC INLET DESIGNED FOR A TILT-NACELLE V/STOL AIRPLANE (Boeing Co., Seattle, Wash.) 115 p HC A06/MF A01 CSCL 21E G3/07

N78-17062

Unclas 04788

By J. Syberg

January 1978

Distribution of this report is provided in the interest of information exchange. Responsibility for the contents resides in the author or organization that prepared it.

Prepared under Contract No. NAS2-9640 by
Boeing Military Airplane Development
Seattle, Washington

for

AMES RESEARCH CENTER
NATIONAL AERONAUTICS AND SPACE ADMINISTRATION

REPRODUCED BY
NATIONAL TECHNICAL
INFORMATION SERVICE
U. S. DEPARTMENT OF COMMERCE
SPRINGFIELD, VA. 22161

CONTENTS

		PAGE
	LIST OF TABLES	
	LIST OF FIGURES	
1.0	SUMMARY	1
2.0	INTRODUCTION	3
3.0	SYMBOLS AND ABBREVIATIONS	4
4.0	PROGRAM SCOPE AND OBJECTIVES	7
5.0	TEST APPARATUS	9
	5.1 Lift/Cruise-Fan Inlet	9
	5.2 Model Description	9
	5.3 Instrumentation	10
	5.4 Test Facility	11
	5.5 Test Conditions and Procedures	12
	5.6 Data Reduction	12
6.0	TEST RESULTS	15
	6.1 Inlet Separation Boundaries	15
	6.2 Operating Limits	16
	6.3 Performance	19
	6.3.1 Performance at Design Conditions	19
	6.3.2 Effects of Angle of Attack	20
	6.3.3 Effects of Fan Blade Angle	21
	6.4 Nacelle Forces	21
	6.5 Comparison with Small Scale Inlet Tests	23
	6.6 Streamtube Offset at 0^{o} Angle-of-Attack	24
7.0	CONCLUSIONS AND RECOMMENDATIONS	25
	REFERENCES	27

LIST OF TABLES

		PAGE
1.	Force Data	28-29

LIST OF FIGURES

		PAGE
1.	V/STOL Inlet Low Speed Design Points	30
2.	Effects of Flow Separation on Inlet Performance	31
3.	LCF Inlet Schematic	32
4.	LCF Inlet Contours	33
5.	Nacelle Schematic	34
6.	Cowl Static Pressure Instrumentation	35
7.	Fan Face Instrumentation	36
8.	Fan Duct Instrumentation	37
9.	Compressor Face Instrumentation	38
10.	Nacelle Installed in 40-by 80-foot Wind Tunnel	39
11.	Wind Tunnel Installation Schematic	40
12.	Data Acquisition and Reduction System Diagram	41
13.	On-Line Display of Inlet Boundary Layer Separation	42
14.	Fan Face Total Pressure Profiles, Windward Rake, Run No. 4, Conditions 2 and 3.	43
15.	Fan Face Total Pressure Profiles, Windward Rake, Run No. 6, Conditions 10 and 11.	44
16.	Fan Face Total Pressure Profiles, Windward Rake Run No. 32, Conditions 14 and 16.	45
17.	Inlet Separation Boundaries, Low Airflows	46
18.	Inlet Separation Boundaries, Medium and High Airflows	47
19.	Inlet Separation Boundaries	48
20.	Inlet Separation Boundaries. Comparison with Empirical Prediction	49
21.	Separation Boundaries	50

LIST OF FIGURES (Continued)

		PAGE
22.	Performance Characteristics during Separation V_o = 45 m/s, WK1A = 100 kg/sm^2	51
23.	Windward Cowl Static Pressure Profiles, V_o = 45 m/s, WK1A = 100 kg/sm^2	52
24.	Fan Face Total Pressure Profiles, Windward Rake, V_o = 45 m/s, WK1A = 100 kg/sm^2	53
25.	Fan Face Total Pressure Maps, V_o = 45 m/s, WK1A = 100 kg/sm^2	54
26.	Fan Nozzle Total Pressure Profiles, V_o = 45 m/s, WK1A = 100 kg/sm^2	55
27.	Compressor Face Rake Total Pressure Maps, V_o = 45 m/s WK1A = 100 kg/sm^2	56
28.	Fan Blade Vibratory Stress During Lip Separation	57
29.	Windward Plane Inlet Station for Leading Edge of Separation	58
30.	Static Pressure Profiles with Diffuser Separation V_o = 45 m/s, WK1A = 100 kg/sm^2	59
31.	Static Pressure Profiles with Diffuser Separation V_o = 39 m/s, α= 90^o	60
32.	Fan Face Total Pressure Profiles with Diffuser Separation, V_o = 45 m/s, WK1A = 100 kg/sm^2	61
33.	Fan Face Total Pressure Profiles with Diffuser Separation, V_o = 39 m/s, α= 90^o	62
34.	Diffuser Separation Characteristics in Small and Large Scale Inlet Models	63
35.	Inlet Performance Characteristics, V_o = 72 m/s, α= 45^o	64
36.	Inlet Performance Characteristics, V_o = 64 m/s, α= 60^o	65
37.	Inlet Performance Characteristics, V_o = 54 m/s, α= 75^o	66
38.	Inlet Performance Characteristics, V_o = 39 m/s, α= 90^o	67
39.	Inlet Performance Characteristics, V_o = 20 m/s, α= 120^o	68
40.	Inlet Static Pressure Profiles, Windward Side, V_o = 72 m/s, α= 45^o	69
41.	Inlet Static Pressure Profiles, Windward Side, V_o = 64 m/s, α= 60^o	70

PAGE

42. Inlet Static Pressure Profiles, Windward Side, V_0 = 54 m/s, α= 75° 71
43. Inlet Static Pressure Profiles, Windward Side, V_0 = 39 m/s, α= 90° 72
44. Inlet Static Pressure Profiles, Windward Side, V_0 = 20 m/s, α= 120° 73
45. Fan Face Total Pressure Profiles, Windward Side Rake, V_0 = 72 m/s, α= 45° 74
46. Fan Face Total Pressure Profiles, Windward Side Rake, V_0 = 64 m/s, α= 60° 75
47. Fan Face Total Pressure Profiles, Windward Side Rake, V_0 = 54 m/s, α= 75° 76
48. Fan Face Total Pressure Profiles, Windward Side Rake, V_0 = 39 m/s, α= 90° 77
49. Fan Face Total Pressure Profiles, Windward Side Rake, V_0 = 20 m/s, α= 120° 78
50. Fan Face Total Pressure Maps, V_0 = 72 m/s, α= 45° 79
51. Fan Face Total Pressure Maps, V_0 = 64 m/s, α= 60° 80
52. Fan Face Total Pressure Maps, V_0 = 54 m/s, α= 75° 81
53. Fan Face Total Pressure Maps, V_0 = 39 m/s, α= 90° 82
54. Fan Face Total Pressure Maps, V_0 = 20 m/s, α= 120° 83
55. Engine Performance Characteristics, V_0 = 72 m/s, α= 45° 84
56. Engine Performance Characteristics, V_0 = 64 m/s, α= 60° 85
57. Engine Performance Characteristics, V_0 = 54 m/s, α= 75° 86
58. Engine Performance Characteristics, V_0 = 39 m/s, α= 90° 87
59. Engine Performance Characteristics, V_0 = 20 m/s, α= 120° 88
60. Engine Performance Characteristics at Design Conditions 89
61. Effects of Angle of Attack on Inlet and Core Engine Performance, V_0 = 39 m/s 90
62. Effect of Angle of Attack on Fan Operation, V_0 = 39 m/s 91
63. Effects of Angle of Attack on Windward Fan Face Rake Total Pressure Profile, V_0 = 39 m/s, WKlA = 138 kg/sm^2 92

PAGE

64. Fan Nozzle Static Pressure vs. Inlet Angle of Attack 93
65. Windward Cowl Static Pressure Profiles with Different Fan Fan Blade Angles, V_o = 39 m/s, α= 90° 94
66. Windward Fan Face Rake Total Pressure Profiles with Different Fan Blade Angles, V_o = 39 m/s, α= 90° 95
67. Windward Cowl Static Pressure Profiles near Onset of Diffuser Separation with Different Fan Blade Angles, V_o = 39 m/s, α= 90° 96
68. Windward Fan Face Rake Total Pressure Profiles near Onset of Diffuser Separation with Different Fan Blade Angles, V_o = 39 m/s, α= 90° 97
69. Lip Separation with Different Fan Blade Angles 98
70. Effect of Lip Separation on Inlet Airflow and Nacelle Net Thrust 99
71. Nacelle Pitching Moment using Test Model Center-of-Moment as Reference Center 100
72. Nacelle Pitching Moment using Airplane Nacelle Pivot Point as Reference Center 101
73. Photographs of Model during Angle-of-Attack Operation 102
74. Fan Face Recovery at Design Conditions for Three Different Scale Models of the LCF Inlet 103
75. Fan Face Distortion at Design Conditions for Three Different Scale Models of the LCF Inlet 104
76. Static Pressure Distributions on Upper Cowl Lip, V_o = 72 m/s, α= 0° 105
77. Static Pressure Distribution on Lower Cowl Lip, V_o = 72 m/s, α= 0° 106
78. Stagnation Points on Upper and Lower Cowl Lip of 0° Angle of Attack 107
79. Off-Set of Stagnation Plane from Engine Centerline at 0° Angle of Attack 108

1.0 SUMMARY

A large scale model of a lift/cruise-fan inlet designed for a tilt-nacelle V/STOL airplane was tested with engine in the NASA Ames 40- by 80-foot wind tunnel. To provide high angle-of-attack capability during take-off and landing while maintaining low cruise drag the lift/cruise-fan inlet features an asymmetric design with a high-contraction-ratio lip on the lower part and a conventional thin lip on the upper part of the inlet. The ratio of hilite area to throat area is 1.50, and the local area contraction ratio for the lower lip in the windward plane is 1.76. The inlet length from hilite plane to fan face is 82 percent of the fan face diameter.

The engine used for the test consists of a Hamilton Standard 1.4 m (55 in.) variable pitch fan driven by a Lycoming T55-L-11A 2800 KW (3750 hp) gas turbine core engine. Appropriate cowlings and fairings were provided to assemble the propulsion system components into a wind tunnel test article that simulated the tilting nacelle on a proposed NAVY V/STOL airplane. Performance and force balance data were obtained at free stream velocities ranging from 0 to 82 m/s (0-160 knots) and inlet angles of attack ranging from 0 to 120 degrees. Design goals ranged from 45 degrees at 72 m/s (140 knots) to 120 degrees at 21 m/s (40 knots).

High performance and stable operation was verified at all of the design forward-speed and angle-of-attack conditions. At some of these, however, operation near the lower end of the inlet design airflow range is not feasible. The largest discrepancy from the design goals were found at 60 degrees angle of attack and 64 m/s (125 knots) forward speed. While the design airflow range at this condition is 78 - 151 kg/sm^2 (16 - 31 lb/sec ft^2), safe operation was possible only at inlet airflow rates greater than approximately 107 kg/sm^2 (22 lb/sec ft^2).

Within the operating envelope the inlet generally provides high total pressure recovery and low distortion to the fan. Only small increases in distortion are observed as the angle of attack is increased towards the upper limit. Prior to reaching this limit, the fan and engine operating characteristics are also nearly insensitive to angle of attack.

The operating limits for the inlet/nacelle were found to be determined by a sudden change in the inlet flow pattern, which caused a significant drop in the measured net thrust as well as a sharp increase in the fan blade vibratory stresses. This change in flow pattern is associated with boundary layer separation in the inlet. When the angle of attack is increased at constant free-stream velocity and inlet airflow, a value is reached where a small separation is formed in the diffuser of the inlet. When the angle of attack is increased beyond this point the separation grows in size and moves forward in the inlet. As the angle of attack is further increased, the flow suddenly becomes very unsteady and the separation now appears to originate at or near the hilite of the inlet lip. This sudden change is associated with high fan blade stresses and a loss in thrust and thus constitutes the operating limit.

The angle of attack at which the onset of inlet diffuser separation occurs was found to vary linearly with inlet throat to free stream velocity ratio within a given range of inlet throat Mach number, or inlet corrected airflow. The boundaries for onset of diffuser separation for the 1.4 m (55-inch) inlet model are significantly improved over those previously established for a 0.38 m (15-inch) and a 0.50 m (20-inch) model of the LCF inlet. In addition, the inlet total pressure recovery is generally higher and the distortion lower on the large scale inlet than on the two smaller inlets. However, it appears that the lip separation on the large scale inlet occurs at less severe operating conditions than the lip separation on the smaller inlets, such that the large scale inlet operating limits are more restrictive than expected. It was determined that the fan blade angle for the range available on the variable pitch Q-fan has little or no effect on the inlet separation boundaries.

A correlation for the nacelle pitching moment was developed. The nacelle drag contributes significantly to this moment during high angle-of-attack operation. Data recorded at zero degrees angle of attack were analyzed to define the stagnation points on the upper and lower cowl lip. This information can be used to simplify future cruise drag predictions for the asymmetric inlet.

ORIGINAL PAGE IS
OF POOR QUALITY

2.0 INTRODUCTION

The development of V/STOL airplanes for both civilian and military applications requires propulsion data in technology areas where relatively little experimental work has been done to date. An asymmetric inlet design for a tilt-nacelle lift/cruise fan (LCF) propulsion system was developed by The Boeing Company to be tested in an experimental program funded by NASA-Ames Research Center under Contract NAS2-9215. The program included wind tunnel testing of a 0.38 m (15-inch) inlet model with a cold-flow duct and a 1.4 m (55-inch) model with fan. The objectives of the program were to determine the range of nacelle tilt angles, freestream velocities, and engine airflows for which a fixed lip inlet can provide pressure recoveries and distortion levels that result in acceptable engine core/fan operating characteristics (stall tolerance) and fan blade stress levels.

The large scale inlet model was designed and fabricated to fit the existing Hamilton Standard Variable pitch Q-Fan. The fan has a 1.4 m tip diameter and is driven by a Lycoming T-55L-11A gas turbine engine. Appropriate cowlings, fairings, etc. were designed and fabricated to develop a nacelle suitable for wind tunnel testing. Testing was conducted in the 40- by 80-foot wind tunnel at NASA Ames Research Center. However, the planned test program was not completed due to a mechanical failure which resulted in partial destruction of the T-55 core engine and Q-fan gear box. An analysis of the small and large scale inlet test results obtained under Contract NAS2-9215 is presented in reference 1.

The Q-fan/T-55 propulsion system was rebuilt in the early part of 1977. Verification testing of the redesigned fan gearbox was successfully completed in April 1977. In the present program the rebuilt propulsion system was tested in the 40- by 80-foot wind tunnel with the primary objective of completing the originally planned test.

While the large scale propulsion system was being rebuilt, a small scale model of the LCF inlet was tested with a 0.5 m fan at NASA Lewis Research Center under Contract NAS3-20597, reference 2. A comparison of the large scale and small scale test results is included in this report.

ORIGINAL PAGE IS
OF POOR QUALITY

3.0 SYMBOLS AND ABBREVIATIONS

A	Flow area
A_{FAN}	Fan face area - 1.206 m^2 (12.98 ft^2)
AR	Flow area at fan nozzle rake = 1.064 m^2 (11.45 ft^2)
D_H	Hilite diameter
DISC	Max-min total pressure differential at compressor face divided by average total pressure
DISF	Max-min total pressure differential at fan face divided by average total pressure using all fan face rake total pressures
DISF2	Max-min total pressure differential at fan face divided by average total pressure ignoring the outer probe on each of the fan face rakes.
F_N	Net thrust measured by the force balance system
F_R	Inlet ram drag
F_S	Component of F_X and F_Y in the direction normal to the engine centerline
F_X	Force measured in tunnel streamwise direction
F_Y	Nacelle lift force measured in the tunnel horizontal plane perpendicular to the streamwise direction
FPR	Fan pressure ratio
H,H'	Moment arm referenced to hilite plane
KN2	Power turbine speed (rpm) corrected to standard temperature
L	Radial distance measured from inlet wall at fan face rake station
LCF	Lift/Cruise - Fan
M_Z	Nacelle pitching moment referenced to model center-of-moment
M_Z'	Nacelle pitching moment referenced to airplane nacelle pivot point
N2	Power turbine speed (rpm)
P	Static pressure
P_C,P_S	Static pressure

PDF Dynamic total pressure on fan face rake

PDS Dynamic static pressure on inlet wall

PM Prandtl static pressure on fan nozzle rake

PP Prandtl static pressure on fan face rake

PT Total pressure

PTCA Area weighted average total pressure at compressor face

PTF Total pressure on fan face rake

PTFA Area weighted average total pressure at fan face

PTM Total pressure on fan nozzle rake

PTO Free stream total pressure

QF2 Axisymmetric inlet model tested previously

R Radius

R_L Inlet radius measured from fan centerline

R_{FAN} Fan tip radius = 0.699 m (27.5 in)

R_H Hilite radius

S Surface distance along cowl wall measured from hilite

TTM Total temperature on fan nozzle rake

V_H/V_o Hilite velocity ratio

V_o Tunnel velocity

V_o/V_H Inlet velocity ratio based on hilite area

$V_o/\sqrt{\theta}$ Tunnel velocity corrected to standard temperature

V_{TH} Inlet throat velocity

W1 Fan face airflow calculated from WK1A

W2 Fan face airflow calculated from fan face rake total and static pressure measurements

ORIGINAL PAGE IS
OF POOR QUALITY

W3	Sum of fan nozzle airflow calculated from fan nozzle rake data and core engine airflow calculated from compressor face rake data
WK1A	Fan face airflow corrected to standard sea-level conditions and divided by fan face area; based on small scale model airflow calibration curve
$WK1A_{SEP}$	WK1A-value corresponding to on-set of diffuser separation
X	Inlet axial station referenced to hilite plane
Y	Radial distance at the fan nozzle rake station
α	Inlet angle of attack
α_{SEP}	α-value corresponding to onset of diffuser separation
β	Fan blade angle
θ	Ratio of total temperature to standard day temperature
Ψ	Circumferential position
$+\Delta W$	Increasing inlet airflow
$-\Delta W$	Decreasing inlet airflow

Subscripts

H	Hilite
TH	Throat

4.0 PROGRAM SCOPE AND OBJECTIVES

On a tilting nacelle V/STOL airplane the inlet is exposed to much more demanding operating conditions at low speeds than on a conventional subsonic airplane. The combinations of freestream velocity and angle of attack are particularly severe during the landing transient as illustrated in figure 1. The main function of the inlet is to supply flow with low total pressure distortion and high total pressure recovery to the fan since nacelle drag is generally not a major factor during these low speed maneuvers.

The primary source of distortion (localized total pressure loss) in a subsonic inlet is flow separation. At high airflow rates (near choking conditions) local pockets of supersonic flow tend to develop on the inlet cowl. Total pressure is lost when the flow, through shocks, decelerates to subsonic speeds. More importantly, when the shock waves, or adverse pressure gradients, become sufficiently strong, the flow separates away from the cowl (in the absence of boundary layer control) leading to increases in distortion and reductions in recovery. We shall refer to this flow phenomenon as the "+ΔW separation," since for a given freestream velocity and angle of attack it occurs as the airflow increases beyond a limiting value. When the inlet is separated in the +ΔW mode, the distortion increases rapidly with increasing airflow.

For the present program another type of separation, which we shall call a "-ΔW separation" is more significant. At a given freestream velocity and angle of attack the -ΔW separation occurs when the airflow is decreased below a limiting value. This seems to be contradictory to the fact that the adverse pressure gradients in the inlet decrease with decreasing airflow. However, the local velocity (and the local boundary layer Reynolds number) is also decreasing with decreasing airflow making the boundary layer more sensitive to an adverse pressure gradient. Apparently, this increased sensitivity can, under certain free stream conditions, dominate the favorable change in pressure gradient such that the inlet boundary layer eventually separates.

The effects of the two types of separation on inlet performance are shown schematically in figure 2. One measure often used as an indicator of the severity of separation is distortion. It is most simply defined as the difference between the maximum and minimum total pressures at the fan face divided by the average total pressure at the same station. When separated flow is present at the fan face, the minimum total pressure is approximately equal to the local static pressure. Low airflow rates imply a small difference between the total and static pressures. Thus for a -ΔW separation the distortion tends to be relatively low. It follows that if the separation can be restricted to very low airflow rates, the fan performance may not be significantly degraded and the blade stresses may be acceptable while operating with separated flow in the inlet since the distortion will be low.

As stated in the Introduction, the objectives of the program were to determine the limits of operating conditions where a fixed lip inlet can provide recoveries and distortion levels that are compatible with fan and core engine operating characteristics. The nominal design goal conditions for the present

program were established from analysis of estimated mission requirements for the Navy Type A V/STOL airplane. These design conditions are tabulated in figure 1.

5.0 TEST APPARATUS

5.1 LIFT/CRUISE - FAN INLET

A schematic of the LCF inlet is shown in figure 3. The design incorporates some unique features. A cross-section taken in a radial plane at the upper (leeward during angle-of-attack operation) part of the inlet shows a fairly conventional cowl, while a similar cut at the lower (windward) part of the inlet reveals much thicker and blunter contours. The purpose of the asymmetry is to take advantage of the operating characteristics of the airplane; i.e., the inlet is subjected only to positive angles of attack. At a positive angle of attack the windward stagnation point moves outboard, increasing the internal pressure gradients, while the leeward stagnation point moves inboard reducing the internal pressure gradients. Thus for the windward cowl the operating condition becomes increasingly severe with angle of attack and freestream velocity. For the leeward cowl, the worst condition is ground static operation at maximum airflow.

Referenced to the fan centerline, the local contraction ratio $(R_H/R_{TH})^2$ for the leeward cowl is 1.30. This value is based on a review of the ground static performance of various existing inlets. For the windward cowl the local contraction ratio is 1.76. This latter value is based on results obtained from testing of a series of small scale axisymmetric inlet models, one of which is shown in figure 3. The overall area contraction ratio (A_H/A_{TH}) for the asymmetric design is 1.50. The complete inlet contours are listed in figure 4. Note that in any cross section normal to the fan centerline the cowl contours are circular. Another feature of the cowl is that the wall curvature is everywhere continuous. This is considered important since near the cowl lip the flow attains transonic velocities at angle of attack, and potential flow analysis have indicated that at such velocities a continuous wall curvature distribution helps to maintain smooth pressure gradients. Further details of the LCF inlet design are described in reference 1.

5.2 MODEL DESCRIPTION

The nacelle assembled for this test program contains the LCF inlet, a variable pitch fan, and a turboshaft core engine. Appropriate cowlings and fairings were provided to obtain a model suitable for wind tunnel testing. Figure 5 shows a schematic of the nacelle.

The major dimensions of the LCF inlet, when sized for the Hamilton-Standard Q-Fan demonstrator, are as follows:

hilite diameter, D_H	=	1.469 m (57.826 in)
throat diameter, D_{TH}	=	1.200 m (47.236 in)
fan face diameter, D_{FAN}	=	1.397 m (55 in)

ORIGINAL PAGE IS
OF POOR QUALITY

The Hamilton-Standard Q-Fan demonstrator is a 1.397 m (55 in), 13 bladed, variable pitch fan which utilizes a Lycoming T55-L-11A, 2800 KW (3750 hp) gas turbine as the core engine. The fan has a 17:1 bypass ratio and is driven through a 4.75:1 reduction gear to a maximum speed of 3365 rpm. The fan rotates clockwise when looking aft. Reference 3 contains further details of the Q-Fan/T-55 propulsion unit.

The primary supporting structure for the nacelle is contained in the fan duct cowling. This supporting ring houses the fan exit guide vanes. The vanes in turn support the fan/engine mounting structure. The fan duct support ring also provides the structural interface for attachment of the inlet and the fan exit nozzle, and for mounting the nacelle on the wind tunnel pylon. A detailed description of the test article is given in reference 4.

5.3 INSTRUMENTATION

The test model was instrumented extensively to provide detail aerodynamic data and to ensure safe operation of the propulsion system. This section describes the model performance instrumentation, which includes all parameters that were recorded during the test and processed off-line. Details of the instrumentation used for monitoring the fan/engine operation and health are described in references 5 and 6.

5.3.1 Inlet Instrumentation

The inlet cowl is provided with 18 surface static pressure taps at the top (0^o), 18 taps at the bottom (180^o) and one tap at each side (90^o and 270^o). Seven additional surface taps are distributed circumferentially at the fan face rake station. Model coordinates for these 45 surface static taps are listed in figure 6.

The inlet static pressure instrumentation includes a dynamic pressure transducer located at Station $X/R_{FAN} = 0.4445$ next to P_C 32. This transducer, PDS, was monitored on-line to determine the forward progression of the inlet separation.

The fan face rake has 7 arms spaced 51.43^o apart starting at 180^o. Each rake arm is provided with 10 steady state total pressure probes. The outer diameter and wall thickness of the probe tubing are 0.32 cm (0.125 inches) and 0.03 cm (0.012 inches), respectively. The probes have squared off faces. A Prandtl static probe is located midway between the two innermost pressure probes on each rake arm. The probe radii (referenced to the fan centerline) are listed in figure 7. The rake arm at 180^o also contains 3 close-coupled dynamic pressure transducers. These are mounted side-by-side with three of the steady state probes. The outermost dynamic probe was used to detect flow separation in the inlet, while the inner probes were used to monitor the turbulence level in and near the core engine flow.

5.3.2 Fan Duct Instrumentation

The fan duct contains two instrumentation rakes on diametrically opposite sides near the exit plane of the nozzle. Each rake contains 10 total pressure probes, 3 total temperature sensors, and 2 static pressure probes. The fan duct rakes are defined in figure 8.

5.3.3 Engine Instrumentation

The primary instrumentation in the core engine is an eight-arm total pressure rake located just upstream of the compressor. Each arm on the compressor face rake contains six total pressure probes and one static pressure tap. The third probe (from the outer end) on four of the rake arms is a high response (Kulite) total pressure sensor. The compressor face rake is shown in figure 9 A temperature probe (TTC) is located at 180° near the cowl at the same station.

Additional core engine instrumentation includes a three-probe total pressure rake with an adjacent surface static pressure tap located near the entry of the compressor inlet at the 0° circumferential position. Four static pressure taps near the core nozzle exit plane are also provided.

5.3.4 Fan/Engine Operation

Parameters recorded on the data system to define the basic system condition are fan blade angle, power lever angle, compressor speed, turbine speed, turbine interstage temperature, and engine torque. Five strain gauges installed on selected fan blades were monitored (and recorded on magnetic tape) to assure operation of the fan blades within their structural design envelope.

5.4 TEST FACILITY

The test was conducted in the NASA Ames 40- by 80-ft wind tunnel. Figure 10 shows the model installed in the wind tunnel.

The nacelle was mounted on a single, hollow column strut approximately 3.8 m (150 in) from the wind tunnel floor. The strut in turn was attached to the NASA floor mounted semispan model turntable. The turntable is located on the wind tunnel vertical centerline. The semispan turntable, strut and nacelle were "on balance" for measuring model forces. A large fairing or "wind shield", off balance, protected the turntable and strut surfaces from the wind tunnel aerodynamic forces.

The nacelle was yawed in the horizontal plane by means of the tunnel turntable to simulate operation at the various inlet angles of attack. The inlet top/bottom ($0^{\circ}/180^{\circ}$) plane was located on a wind tunnel horizontal plane, see figure 11.

ORIGINAL PAGE IS
OF POOR QUALITY

5.5 TEST CONDITIONS AND PROCEDURES

There were three basic test variables, namely tunnel speed (V_o), inlet angle of attack (α), and inlet airflow (WK1A). The test ranges for these variables are listed below:

V_o : 0-82 m/s (0-160 knots)

α : $0\text{-}120^o$

WK1A : 75-170 kg/sm^2 (15-35 lb/sec ft^2)

Note that 170 kg/sm^2 is the maximum airflow capability of the Q-Fan/T-55 engine.

The test was conducted using two basic procedures. In Procedure 1, the inlet angle of attack was varied at constant V_o and WK1A. In Procedure 2, the inlet airflow was varied at constant V_o and α.

Procedure 1 was used to determine the inlet separation boundaries and establish the operating limits. The operating limits were based on the following criteria:

(1) The fan blade stresses shall not exceed 38 x 10^6 N/m^2 (5500 psi) on the blade bending strain gauges or 20 x 10^6 N/m^2 (3000 psi) on the blade torsional strain gauges. (These limits were defined by Hamilton Standard.)

(2) The first sign of inlet-separation induced flow distortion at the compressor face, measured on-line as an increase in turbulence level, shall be defined as the operating limit. (This criterion was considered to be conservative since a small increase in turbulence should not increase the distortion to the upper limit for the core engine.)

Procedure 2 was used to obtain detail performance and force balance data. The basic procedure was to start the run at a high airflow and then reduce the inlet airflow in small increments. The number of data points to be recorded and the method of reducing the airflow (fan speed or fan blade angle) in a given run were varied with the forward-speed/angle-of-attack condition.

Further details of the test procedures are included in reference 5. A complete definition of the test conditions covered in the present wind tunnel test program is presented in reference 6.

5.6 DATA REDUCTION

The data acquisition and reduction system used in the 40- by 80-ft wind tunnel is diagrammed in figure 12. On-line data were available from various x-y plotters, meter panels, and oscilloscopes to assure safe operation of the propulsion system and to provide a comprehensive definition of the aerodynamic conditions in the inlet and at the compressor face.

Quick-look off-line data were processed on the NASA Ames 360 computer to provide maximum test visibility and testing efficiency. Final data and computer plots were processed at Boeing following the completion of the test.

Details of the data system, data reduction procedures, and data reduction equations are included in reference 6. To facilitate the reading of this report the definitions of the most significant aerodynamic parameters are presented below:

Inlet Airflow: It was of particular importance for the present test to obtain an accurate measurement of the inlet airflow. The airflow was therefore calculated by three independent methods. The first of these is based on a calibration of the small scale LCF inlet model tested under Contract NAS2-9215 (see ref. 1). It was shown in that program that the average value of four wall static pressures located in the inlet throat at circumferential positions of 0^{o}, 90^{o}, 180^{o}, and 270^{o} correlates with the inlet airflow and that this correlation is independent of inlet angle of attack or freestream velocity provided that no large separation is present in the inlet. The airflow derived from this correlation, which is considered to be the most accurate method of calculation for the present test, is denoted W1 (absolute airflow) or WK1A (corrected airflow per unit area at the fan face).

For the second method of calculation the fan face is divided into 70 area increments, each centered on one of the fan face rake total pressure probes. The local static pressure was interpolated for each total probe (extrapolated for the innermost probe on each rake) from the nearest cowl static and Prandtl static pressure values. Using these values and the tunnel total temperature the airflow was calculated for each area increment. Summation of the flow increments provided the second inlet airflow calculation (W2). The fan duct exit and compressor inlet airflows were calculated similarly from the respective rake instrumentation readings. When added together these provided a third independently calculated airflow measurement (W3). For conditions with large inlet separations, i.e., lip separations, the airflows presented in this report were estimated based on the W2 and W3 measurements.

Total Pressure Recovery: The total pressure recoveries computed from the fan face rakes (PTFA), compressor face rakes (PTCA) and fan duct exit rakes (PTMA) are all area weighted averages using all of the respective probes.

Distortion: The fan face distortion (DISF) and the compressor face distortion (DISC) are both computed as the difference between the maximum and minimum of all respective total pressure readings divided by the respective area weighted average total pressure. Since the fan face rakes are designed to provide detail information on the total pressure profile shape near the cowl wall, the distortion, DISF, is strongly influenced by the wall boundary layer even at low angle-of-attack conditions. Owing to the finite tip clearance of the fan blades and the high blade velocity near the tip the fan efficiency is relatively low near the cowl. Thus losses in the inlet flow close to the wall do not significantly affect the overall fan

ORIGINAL PAGE IS
OF POOR QUALITY

performance. Consequently, in the evaluation of flight hardware the flow contained in an annulus of some arbitrary height is often ignored. This height is typically 2.5 cm (1 inch) full scale. By ignoring the outermost total pressure probe on the fan face rakes a similar max-min distortion index (DISF2) was obtained for this test. Note from figure 7 that the outer 2.1 cm (.83 inches) of the boundary layer is ignored when using this distortion index. The corresponding height for DISF is .7 cm (.27 inches).

6.0 TEST RESULTS

6.1 INLET SEPARATION BOUNDARIES

As described in Section 4.0 the primary objective of the test program was to establish the range of nacelle tilt angles, freestream velocities, and inlet airflows for which the LCF inlet can provide pressure recoveries and distortion levels that result in acceptable fan/engine operating characteristics and fan blade stress levels. Since these limits are related to the size and intensity of inlet flow separation an important first step is to determine the conditions at which the initial onset of boundary layer separation occurs in the inlet.

The separation boundaries were determined primarily by using test procedure no. 1 (see Section 5.5). The root-mean-square (rms) value of the dynamic pressure output from the fan face rake Kulite transducer located closest to the windward side cowl wall (PDF1, see figure 7) was plotted on-line versus inlet angle of attack on an x-y plotter. A sudden increase in the RMS-level was usually indicative of the onset of separation. Steady state data points were then recorded at angles of attack near this point of increasing turbulence. Traces of PDF1 versus α for one of the forward speed conditions [V_o = 54 m/s (105 knots)] tested are shown in figure 13 to illustrate the test technique. Following the test the steady state data points were analyzed to determine which points indicate boundary layer separation and which points indicate attached flow. This judgment was based on the windward side fan face rake total pressure profiles. Samples of profiles recorded on either side of the separation boundary are shown in figures 14-16. It is evident from these figures that the onset of boundary layer separation is defined as the first indication of unusual shapes of the boundary layer profile as measured by the fan face rakes.

The data analysis showed that while PDF1 was an accurate on-line indicator of boundary layer separation at low inlet airflows [less than about 135 kg/sm^2 (28 lb/sec ft^2)], it was less precise when the separation occurred at high inlet airflows, i.e., at the most extreme angle-of-attack conditions (see fig. 13). For these conditions an increase in the rms-level was experienced prior to the onset of separation, apparently because the edge of the attached, but thicker, boundary layer had reached the location of the Kulite probe.

The analysis of the fan face rake profiles provided a large number of data points recorded near the onset of separation, i.e., either barely attached or just separated. The three significant parameters for defining the separation boundaries are freestream velocity (V_o), inlet angle of attack (α), and inlet airflow (WK1A). It was shown in reference 12 that similar data for a 0.5 m (20 inch) model of the LCF-inlet could be collapsed into a single curve by converting WK1A to throat velocity (V_{TH}) and plotting the throat velocity ratio V_{TH}/V_o against α. A similar approach was used on the present set of data. The results are shown in figures 17 and 18. The

ORIGINAL PAGE IS
OF POOR QUALITY

solid symbols correspond to separated boundary layer and the open symbols to attached boundary layer. By grouping the data set based on the inlet airflow (WK1A) it was possible for each airflow range to obtain a linear relationship between V_{TH}/V_0 and α_{SEP} (α corresponding to on-set of separation).

The α_{SEP}-lines for the four airflow ranges are compared in figure 19. For a given throat velocity ratio, α_{SEP} is nearly constant for values of $WK1A_{SEP}$ (WK1A corresponding to onset of separation) up to 140 kg/sm^2 (29 lb/sec ft^2) but decreases when $WK1A_{SEP}$ increases above 140 kg/sm^2.

Figure 20 compares the experimental α_{SEP}-lines with the predicted relationship between α_{SEP} and V_{TH}/V_0. This prediction, which is discussed in detail in reference 2, is based on data from the 0.5 m model test extrapolated to the full scale inlet. Since the prediction was valid only for airflows less than 150 kg/sm^2 (31 lb/sec ft^2) the α_{SEP}-line for the highest airflows in figure 19 has been deleted. The prediction, which was based purely on an empirical correlation, is apparently optimistic at the lowest and highest throat velocity ratios but agrees with the data in the mid-range velocity ratios.

The inlet separation boundaries from figure 19 are shown in a different format in figure 21. Note that the abscissa is $V_0/\sqrt{\theta}$, which implies that the separation boundaries in terms of V_0, α, and WK1A will vary with the total temperature. This temperature dependancy is a result of the assumption that the onset of separation can be determined from the throat velocity ratio as shown in figures 17-19. Thus, on a hot day the α_{SEP} for a given operating condition (V_0, WK1A) is higher than the corresponding α_{SEP} on a cold day.

6.2 OPERATING LIMITS

The operating limits for the LCF-inlet/Q-Fan nacelle were determined by reducing the airflow (or increasing α) beyond the separation value, $WK1A_{SEP}$ (or α_{SEP}), until excessive fan blade stresses and/or changes in the core engine flow distortion were observed. The results from these tests showed that the boundary layer separation in the LCF-inlet initially occurs downstream in the diffuser and then moves forward as the airflow is reduced (or α increased). This forward extension of the separation is associated with an increase in the size of the low-pressure region at the fan face and therefore a slight drop in fan face total pressure recovery. Small increases in fan blade stresses may also occur. These trends were also observed in the testing of the 0.5 m (20 inch) LCF-inlet model as discussed in reference 2. When the leading edge of the separated region reaches a certain location in the inlet diffuser, the flow suddenly becomes very unsteady and the separation now appears to originate at or near the hilite of the inlet. This discontinuity in the flow pattern is associated with a drop in both recovery and airflow and a significant increase in fan blade stresses. Several test runs were conducted to investigate this flow phenomenon and the results are presented in the following:

Figure 22 shows some of the inlet and engine parameters measured during a test run in which the angle of attack was varied at constant power setting and wind tunnel speed. The power setting was adjusted to provide an inlet airflow of approximately 100 kg/sm^2 (20.5 lb/sec ft^2). The tunnel speed was 45 m/s (87 knots) during this run. The procedure was to increase α until the safe operating limit was reached and then reduce α without changing the power setting until the flow conditions were back to normal.

Figure 22 clearly shows a discontinuity in all of the aerodynamic parameters when α reaches a value of 81^0, i.e., 8^0 beyond the onset of diffuser separation. The fan face recovery drops from about 0.996 PTO to 0.981 PTO while the fan face distortion increases from 6% to 9%. The core engine total pressure recovery and distortion also deteriorate at this condition. It is significant that the sudden change in flow pattern causes a large reduction (about 15%) in inlet airflow which is the primary reason for the 20% reduction in the thrust measured with the force balance system. As illustrated in figure 22 a rather large hysteresis is also associated with this flow phenomenon: It is necessary to reduce α to 75^0 before high-performance operation is restored.

The pressure profiles measured in the inlet provide a clue to the abrupt change in performance. The static pressure profiles for the windward side of the inlet lip and diffuser are shown in figure 23 for the data points recorded during increasing α, i.e., $\alpha = 70^0$, 73^0, 79^0, and 81^0. The corresponding fan face total pressure profiles on the windward rake are shown in figure 24. The discontinuity occurring at $\alpha = 81^0$ is caused by the diffuser separation suddenly changing into a lip separation originating at the inlet hilite region ($S/R_{FAN} = 0$), see figure 23. This lip separation results in a large low-pressure region at the fan face as evidenced by figure 24. It should be noted that the flow was observed to be very unsteady during conditions with lip separation explaining the non-uniform profiles measured during these conditions. The circumferential extent of the low-pressure region is illustrated by the fan face total pressure isobar plots in figure 25. Nearly 50% of the fan face area is affected by the lip separation.

The effect of the lip separation on the flow conditions downstream of the fan are illustrated in figures 26 and 27. The fan nozzle total pressure profiles on both the leeward and windward side are shown in figure 26. The effect of the diffuser separation ($\alpha = 79^0$) on the windward rake profile is quite small, whereas a large pressure drop is seen when the lip separation is present ($\alpha = 81^0$). The leeward side rake is not affected by the inlet separations. Total pressure isobar plots for the compressor face rakes are shown in figure 27. The flow pattern clearly changes when the lip separation occurs but the overall loss in total pressure is small, see figure 22.

The fan blade bending and torsional stresses were monitored and recorded with various strain gauges during the present wind tunnel test. Figure 28 shows a summary of the results obtained during the lip separation investigation. The blade vibratory stress increases as the angle of attack is increased beyond the value where the onset of diffuser separation occurs. A dramatic rise in stress is seen when the separation jumps forward to the

ORIGINAL PAGE IS
OF POOR QUALITY

lip. The high stress, which in this case is slightly above the endurance limit for the Q-fan blades, persists until the angle of attack is decreased sufficiently to remove the lip separation.

Due to the abrupt loss in thrust and increase in fan blade stresses associated with the lip separation phenomenon it appears that this flow condition should be avoided in flight. The operating limit can therefore be defined as the point where the separation jumps from the diffuser to the inlet cowl hilite. However, it should be noted that surge-and stall-free operation was demonstrated with the lip separation present on several occasions during the test. It was also demonstrated that the lip separation can be removed by reducing the angle of attack (see figure 22) or increasing the power setting, although a certain amount of hysteresis is present with either method.

Since the boundaries for the onset of diffuser separation have already been established (figure 21) the operating limits can be defined by determining the additional reduction in airflow (or increase in α) required for lip separation to occur. Figure 29 shows the results of this study. In this figure the estimated locations of the leading edge of the separation are plotted versus α (Test Procedure 1) or WK1A (Test Procedure 2). In two of the four runs shown lip separation was experienced at the conditions indicated. In the other two runs various on-line instrumentation had indicated that the last data points (lowest airflows) were recorded just prior to the occurrence of lip separation. The leading edge stations of the diffuser separations were obtained by studying the aft diffuser static pressure profiles as illustrated in figure 30 and 31. The leading edge may be defined as the point where the slope of the pressure profile deviates significantly from that of the attached pressure profile at the same station. Although this method is somewhat subjective, especially due to the relatively large spacing between the pressure taps in this region of the inlet, it does provide an indication of the location of the separation. A correlation between the leading edge station of the diffuser separation and the size of the low-pressure region at the fan face may be obtained by comparing figures 30 and 31 with figures 32 and 33, respectively.

Referring back to figure 29 it is interesting to note that the change in flow pattern from diffuser separation to lip separation always seems to take place when the separation reaches station S/R_{FAN} = .85 - .90. The change in inlet airflow from on-set of diffuser separation to on-set of lip separation is in the order of 10 kg/sm^2 (2 lb/sec ft^2). This is much less than that found on the 0.5 m LCF-inlet model tested in the NASA Lewis 9- by 15-foot wind tunnel, reference 2. Figure 34 shows a comparison between the present 1.4 m and the 0.5 m inlet models. On the smaller inlet the change in separation location per unit of airflow was smaller and the separation could be pushed farther forward before the lip separation occurred, thereby providing a much greater margin between the diffuser separation boundary and the lip separation boundary. Consequently, the operating limit, when defined as the point where lip separation occurs, is actually better for the small scale inlet even though the full scale inlet diffuser separation occurs at a lower airflow (due to the higher Reynolds number, see Ref. 1).

A possible explanation for the difference in separation growth between the two different scale models may be found in reference 7. This reference suggests that the lip separation may be caused by a "laminar separation" in

the boundary layer transition region near the hilite and that this laminar separation may occur independent of the diffuser separation. It is also shown in this reference that the laminar lip separation theoretically is more likely to occur on a large scale inlet. It should be noted, however, that the present test results indicate that the lip and diffuser separation phenomenon are interrelated since the large lip separation was always preceded by a diffuser separation and appeared to always occur when the diffuser separation reached a certain point in the diffuser.

Due to the relatively small margin between the diffuser-separation boundaries and the lip-separation boundaries it may be reasonable, although slightly conservative, to define the operating limits as being identical to the diffuser-separation boundaries established in Section 6.1. Thus, the operating limits for the present propulsion system, consisting of the LCF-inlet, the Q-fan, and the T-55 core engine, are shown in figure 21.

6.3 PERFORMANCE

The internal aerodynamic performance of the individual propulsion system components, i.e. inlet, fan, and core engine, is documented in this section. Results obtained at the design conditions are presented. Changes in some of the performance parameters with angle of attack are also shown to provide a more complete description of the operation of the nacelle in a high angle-of-attack environment.

6.3.1 Performance at Design Conditions

Five nominal design flight conditions and the corresponding airflow ranges are listed in figure 1. Figures 35-39 show the inlet performance measured at these conditions. The performance is shown in terms of fan face recovery and distortion (DISF2 and DISF, see Section 5.6 for definitions) versus inlet airflow. The turbulence level measured by PDF1 at the fan face, see figure 13, is plotted to indicate approximately where the diffuser separation takes place. The measured or estimated operating limit, i.e., the point where lip separation takes place, is shown along with the design goal airflow range at each condition. From these figures it is apparent that the inlet will provide high performance at the design forward-speed and angle-of-attack conditions, but that operation near the low end of the design airflow range is not always feasible due to the occurrence of lip separation. Note that the maximum airflow capability of the Q-fan/T-55 engine is approximately 170 kg/sm^2 (35 lb/sec ft^2). Consequently, the performance could not be verified above this airflow level. Test results obtained under Contract NAS2-9215 on a small scale model (approximately 1/4 scale) confirmed however, that the LCF inlet will provide high performance at all design goal conditions up to at least 205 kg/sm^2 (42 lb/sec ft^2), see reference 1.

Inlet static pressure profiles and fan face rake total pressure profiles (windward side) for selected data points from the five design conditions are shown in figures 40-44 and 45-49, respectively. Fan face maps for the highest airflow point, the diffuser separation point and the lowest airflow point recorded at each of the first four conditions are shown in figures 50-53. From these figures it is evident that the inlet boundary layer slowly deteriorates as the airflow is reduced even though the overall

ORIGINAL PAGE IS
OF POOR QUALITY

diffusion rate decreases. As described in Section 4.0, this is a result of a reduction in local velocity with airflow which causes the boundary layer to be more sensitive to adverse pressure gradients.

Fan face maps for the highest airflow point, an intermediate airflow point, and the lowest airflow point (which corresponds to the on-set of diffuser separation) recorded at V_0 = 20 m/s (40 knots) and α = 120° are shown in figure 54. This condition is unique in that low pressure regions are present in the upper half of the inlet. These pockets are largest at the high airflows resulting in relatively low inlet recoveries (compare figure 39 with 35-38). The same type of flow pattern was observed at this design condition on the small scale LCF-inlet, reference 1. Neither model was sufficiently instrumented, however, to allow a detailed analysis of this flow phenomenon.

The fan and core engine performance, in terms of fan pressure ratio, compressor face recovery, and compressor face distortion, are presented in figures 55-59 for the five design conditions. Figure 60 provides a comparison of the individual performance curves. The fan pressure ratio at a given airflow level is clearly a function of freestream condition. As a result the compressor face recovery varies slightly with freestream condition. The distortion, however, is primarily a function of airflow except for the α = 120° condition. The higher distortion level at this condition is apparently a result of the unique flow pattern at the fan face, see figure 54.

6.3.2 Effects of Angle of Attack

Sufficient data was obtained to allow an evaluation of the nacelle performance versus angle of attack at constant tunnel speed and inlet airflow. A detailed description of the performance trends for two different $V_0/WK1A$-conditions are presented in figures 61 and 62. As expected the fan face recovery decreases with increasing angle of attack, but the difference is less than 0.002 PTO between α = 0° and α = 90°. The increase in fan face distortion is more obvious and is a result of a thickening boundary layer in the windward plane as illustrated in figure 63. The compressor face recovery decreases slightly with α but the distortion is not influenced by the change in freestream condition.

The decrease in compressor face recovery is a result of a slight reduction in power turbine speed and the subsequent reduction in fan pressure ratio, see figure 62. This indicates that the power required to maintain a constant inlet airflow decreases when the angle of attack is increased, at least up to 90°. This somewhat surprising result was found to be a result of a reduction in the static pressure in the leeward side of the fan nozzle with increasing angle of attack, as illustrated in figure 64. It appears that an ejector effect is obtained at the fan nozzle exit during angle of attack operation.

6.3.3 Effects of Fan Blade Angle

For the proposed NAVY V/STOL aircraft the variable pitch fan feature is used as the primary means for controlling and adjusting the thrust, and thus the inlet airflow, while the fan rpm is constant. With the present test set-up it was more convenient to change fan rpm through a power lever angle change while maintaining fixed blade angle. However, the effect of varying the fan blade was evaluated at several conditions to determine if the onset of diffuser separation or the onset of lip separation is a function of fan blade angle. Some of the results are presented in the following.

Figures 65 and 66 show the windward side inlet static and fan face total pressure profiles, respectively, for two points recorded at the same inlet airflow but with different blade angles. It may be concluded that the inlet pressure profiles are independent of the blade angle when the boundary layer is attached.

Figures 67 and 68 show similar plots for data points recorded near the onset of diffuser separation. A small separation is apparently present in both data points, and since the points were recorded at exactly the same airflow level it can be concluded that also the onset of diffuser separation is independent of fan blade angle.

The onset of lip separation was also investigated with different settings of the fan blade angle. Figure 69 shows the results. At each blade angle, β, a datapoint was recorded immediately following the onset of lip separation. As shown on the figure, the lip separation occurred at approximately the same engine power setting for both blade angles, indicating that it also occurred at the same inlet airflow. It is therefore concluded, that the fan blade angle does not significantly influence the onset of lip separation.

6.4 NACELLE FORCES

Nacelle forces and moments were measured with a six-component balance system connected to the 40- by 80-foot wind tunnel semispan turntable. The primary purpose of the force measurements was to determine the effects of inlet separation on fan thrust at various airflow levels.

It was shown in figure 22 that the lip separation phenomenon causes a significant drop in the measured net thrust primarily due to the sudden change in inlet airflow. This result was confirmed at several test conditions as shown in figure 70. Here the inlet operating characteristics and the nacelle net thrust are plotted versus engine power for three test runs during which lip separation was encountered while reducing the power setting. In all three cases an abrupt change in nacelle operation is apparent. Also shown in figure 70 are the power settings required to remove the lip separation and restore normal operation. The hysteresis loop is very large at the $\alpha = 105^{o}$ condition and very small at the $\alpha = 90^{o}$ condition. Sufficient data is not available to determine which parameters control the hysteresis. However, it was established that the hysteresis can be very significant, again indicating that this condition should be avoided in flight.

ORIGINAL PAGE IS
OF POOR QUALITY

For flight control purposes it is necessary to establish the various forces and moments acting on the nacelle during low speed maneuvering. To aid in this work the measured forces in the streamwise and lift directions as well as the nacelle pitching moments are tabulated in table 1 for various inlet massflows and freestream conditions. The computed inlet velocity ratio (V_O/V_H) and ram drag (F_R = W1 x V_O) are included in the table. An analysis of the pitching moment data is presented in the following.

The pitching moment is a result of three basically different forces acting on the nacelle during operation at angle of attack: (1) the change in direction of the incoming flow causes an asymmetric pressure distribution on the internal and external nacelle surfaces. The resultant side force (i.e., force normal to the nacelle centerline) is theoretically equal to the ram-drag (F_R) component normal to the engine centerline, i.e., F_R sin α. (2) the external flow separation due to the crosswind over the nacelle results in a drag force (F_S) normal to the engine centerline. Although the external flow pattern and thus F_S are affected by the amount of flow being captured by the inlet this side force is not included in the ram-drag components. (3) As shown in section 6.3.2 the fan thrust is not symmetrical during high angle-of-attack operation. Thus a negative pitching moment will be created by the higher thrust on the leeward side of the nozzle.

In reference 1 it was assumed that the contributions of the two latter forces to the pitching moment are small. The pitching moment was then divided by the ram-drag of the captured streamtube to define a moment arm H/D_H. It was shown that H/D_H reasonably well correlates with inlet velocity ratio and angle of attack. Thus, knowing the location of this force relative to the inlet the pitching moment can easily be calculated for a similar configuration, indepedent of the location of the reference center-of-moment. Figure 71 shows the results of a similar study conducted on the present set of wind tunnel data. These results agree with the data shown in reference 1.

A more comprehensive study of the present data revealed, however, that the results from figure 71 (and figure 50 of reference 1) cannot be directly applied to another configuration if the center-of-moment is offset in the axial direction from that of the present nacelle. It was found that the side force, F_S, resulting from the non-ideal external flow contributes significantly to the measured pitching moment. (The side force is obtained by subtracting the ram drag component F_R sin α from the measured side force.) To illustrate the significance of the location of the reference center-of-moment a different location on the nacelle centerline was considered. The nacelle pivot point on the proposed NAVY V/STOL airplane was chosen as an example. This pivot point is located approximately 0.48 m (19 inches) forward of the wind tunnel model reference center-of-moment. The pitching moment at the pivot point resulting from the side force F_S will therefore reduce the overall pitching moment by 0.48 x F_S (Nm if F_S in Newton) relative to the test model. Figure 72 shows the results when this moment is subtracted from the measured pitching moment. It is evident from figures 71 and 72 that the side force contribution to the pitching moment is significant. Note that the third moment-producing force, i.e., the asymmetric fan thrust, is considered small in the present analysis.

Typical photographs of the test model taken during operation at a high angle-of-attack condition are shown in figure 73. The divergence of the tufts near the leeward plane indicates flow separation. As the inlet airflow is reduced (or V_0/V_H is increased) the separation seems to move closer to the inlet hilite, but the side force F_S does not change significantly with velocity ratio. Note that the lower half of the nacelle is not representative of a flight nacelle due to the fairing around the Q-Fan support structure. Thus the side force resulting from the external flow will probably be lower on the airplane than measured with the present model.

6.5 COMPARISON WITH SMALL SCALE INLET TESTS

Three different scale models of the LCF-inlet have been tested under NASA contracts. A 0.38 m (15-inch) model installed on a cold-flow duct was tested under Contract NAS2-9215. Results from this test are presented in reference 1. A 0.50 m (20-inch) model was tested with a NASA Lewis fan and engine simulator under Contract NAS3-20597. This test is described in reference 2. Finally, the present test was conducted with a 1.4 m (55-inch) inlet model in front of a variable pitch fan driven by a gas turbine engine. The inlet flow characteristics during operation with diffuser and lip separation were compared in section 6.2 for the 1.4 m and the 0.50 m models. A comparison of the inlet performance obtained at the design conditions in the three tests is discussed in this section.

Figure 74 shows the inlet recovery as a function of inlet airflow for the three models at the five design goal conditions. The solid symbols indicate the first points recorded after onset of diffuser separation. The 1.4 m inlet model provides higher recovery and separates at lower airflows than the two small scale inlets. It was shown in reference 1 that these improvements are attributable to the difference in Reynolds number which provides a more favorable boundary layer development on the large inlet model. The separation points on the two small scale inlets are almost identical at the $\alpha = 45^o$ and $\alpha = 90^o$ conditions, but differ considerably at the $\alpha = 60^o$ and 75^o design conditions. It is possible however, that the $\alpha = 60^o$ and 75^o test results for the 0.38 m model were influenced by a wind tunnel blockage effect which seemed to be particulary severe at these conditions. Therefore, the local freestream velocity may have been higher than the indicated tunnel speed.

The onset of diffuser separation is followed by a significant recovery loss in the 0.38 m inlet/cold-flow-duct test model, whereas the 0.50 m inlet/fan model maintains high performance well below the separation point. This difference is probably associated with the fan suction in the 0.50 m inlet which will tend to preserve uniform flow at the fan face and thereby control the size of the separation.

The fan face distortion trends for the three inlet models are shown in figure 75. In general, the distortion trends for the 0.50 m and 1.40 m models are similar while the 0.38 m cold-flow-duct model shows very high distortion values following the onset of diffuser separation. At $\alpha = 120^o$

ORIGINAL PAGE IS
OF POOR QUALITY

the large scale inlet model shows the highest distortion values at the higher airflow levels. Apparently, the low-pressure regions present in the upper half of the inlet at this extreme angle-of-attack condition are more severe on the large scale inlet then on any of the small scale inlets.

6.6 STREAMTUBE OFFSET AT 0^{o} ANGLE-OF-ATTACK

As described in section 5.1 the LCF-inlet features a fat lower lip and a conventional upper lip, see figure 3. The purpose of the asymmetric design is to minimize the nacelle cruise drag while maintaining the high angle-of-attack capability of the lower lip for approach and landing conditions. Unfortunately, the asymmetric design makes the cruise drag predictions extremely difficult since a fully three-dimensional transonic flow program is required for a complete definition of the flow field around the nacelle. A simplified approach to the cruise drag prediction is to use an axisymmetric potential flow program for individual cross-sections of the inlet, for example the top, bottom, and side, and then combine the results into a single drag value. This approach is believed to be valid if the stagnation stream lines are properly located, i.e., the velocity ratio for the axisymmetric inlet representing one cross-section of the inlet should be such that the stagnation point coincides with the actual stagnation point on that cross-section on the asymmetric inlet for the condition simulated. This means that the velocity ratios used in the axisymmetric program should be properly varied between the individual cross-sections in order to represent one velocity ratio on the asymmetric inlet. To aid in future drag predictions with the axisymmetric flow field program an analysis of the test data was made to determine the stagnation points on the upper and lower cross-sections of the inlet lip. These results are discussed in the following.

Figure 76 shows the static pressure profiles measured on the upper cowl lip at three different velocity ratios during 0^{o} angle-of-attack operation. The estimated stagnation points are also indicated. Similar profiles for the lower lip are shown in figure 77. The locations of the stagnation points for the upper and lower lip are compared in figure 78. Also shown in this figure are typical velocity ratios at cruise. The difference between the locations of the stagnation points on the upper and lower lip is illustrated in figure 79 for a velocity ratio $V_H/V_0 = 0.55$. The center of the stagnation plane, which may coincide with the center of the captured streamtube, is offset from the engine centerline by $0.057\ R_H$. In comparison, the center of the circular hilite plane is offset by $0.072\ R_H$.

The stagnation points for a given velocity ratio may change as the free-stream Mach number is increased due to compressibility effects. It is believed, however, that the center of the stagnation plane will remain fixed since the upper and lower stagnation points should change in the same direction and by approximately the same amount. The results shown in figure 79 should therefore be applicable to the cruise conditions.

7.0 CONCLUSIONS AND RECOMMENDATIONS

A large scale model of an asymmetric, fixed geometry inlet designed for a tilt-nacelle V/STOL airplane was tested with a high-bypass-ratio, variable-pitch fan and a gas turbine core engine in the NASA Ames 40- by 80-foot wind tunnel. Performance and force balance data were obtained at freestream velocities ranging from 0 to 82 m/s (0-160 knots) and inlet angles of attack ranging from 0 to 120 degrees. Design goals ranged from 45 degrees at 72 m/s (140 knots) to 120 degrees at 21 m/s (40 knots). Major conclusions drawn from analysis of the test results are described in the following:

- o High performance and stable operation was verified at all of the design forward-speed and angle-of-attack conditions. At some of these, however, operation near the lower end of the design airflow range is not feasible due to the occurrence of lip separation.

- o The operating limits for the propulsion system are reached when the boundary layer suddenly separates at the hilite of the inlet lip. This lip separation causes a significant drop in the net thrust as well as a sharp increase in the fan blade vibratory stresses.

- o The lip separation is always preceded by boundary layer separation in the diffuser of the inlet. It appears that the separation changes from a diffuser separation to a lip separation when the leading edge of the diffuser separation reaches a certain location downstream of the inlet throat. This finding differs from the results from the testing of a 0.50 m (20-inch) inlet model with fan. In the small scale test it was possible to maintain a stable diffuser separation with the leading edge of the separation located farther forward, thus providing a larger margin between onset of diffuser separation and onset of lip separation.

- o The angle of attack at which the onset of diffuser separation occurs appears to vary linearly with inlet throat velocity ratio within a given range of inlet throat Mach number, or inlet corrected airflow.

- o The boundaries for onset of diffuser separation for the 1.4 m (55-inch) inlet model are significantly improved over those previously established for a 0.38 m (15-inch) and a 0.50 m (20-inch) model of the LCF-inlet. This improvement is believed to be a result of the higher Reynolds number which provides a more favorable boundary layer development.

- o The lip separation on the large scale inlet appears to occur at less severe operating conditions than the lip separation on the smaller inlets.

- o The fan blade angle has little or no effect on the inlet diffuser- and lip-separation boundaries.

- o The nacelle drag during high angle-of-attack operation contributes significantly to the nacelle pitching moment.

The operating limits of the tilt-nacelle propulsion system with the LCF inlet can be improved if the on-set of lip separation can be delayed. To accomplish this it will be necessary to first understand why the diffuser

separation jumps forward to the hilite on the large scale inlet when this was not the case on the small scale inlet. Comprehensive studies of the inlet static pressure profiles for the different model scales tested coupled with potential flow and boundary layer analyses are recommended to provide this understanding. Changes in contours and/or addition of boundary layer control systems can then be studied to provide the desired improvement.

REFERENCES

1. J. Syberg and J. L. Koncsek, "Low Speed Tests of a Fixed Geometry Inlet for a Tilt Nacelle V/STOL Airplane," NASA CR-151922, January 1977.

2. J. L. Koncsek and R. J. Shaw, "Operating Characteristics of an Inlet Model Tested with a 0.5 m Powered Fan at High Angles of Attack," NASA CR-135270, September 1977.

3. W. J. Demers, et al., "Testing of the Hamilton Standard Q-Fan Demonstrator (Lycoming T55-L-11A Core Engine)," NASA CR-121265, March, 1973.

4. W. M. Shain, "Test Data Report - Low Speed Wind Tunnel Test of a Full Scale Fixed Geometry Inlet With Engine at High Angles of Attack," NASA CR-151927, November 1976.

5. J. Syberg, "Test Planning and Coordination. Lift/Cruise Fan Inlet Test Program," Boeing Document D-180-20725-1, July 1977.

6. W. M. Shain, "Test Data Report - Low Speed Wind Tunnel Test of a Full Scale Lift/Cruise Fan Inlet, With Engine, at High Angles of Attack," NASA CR-152055, January 1978.

7. D. C. Chou, R. W. Luidens, and N. O. Stockman, "Prediction of Laminar and Turbulent Boundary Layer Flow Separation in V/STOL Engine Inlets," NASA TM X-73575, January 1977.

ORIGINAL PAGE IS
OF POOR QUALITY

Table 1. Force Data

V_o (m/s)	α (degrees)	WK1A (kg/sm^2)	V_o/V_H	Ram drag F_R (N)	Streamwise force F_X (N)	Lift force F_Y (N)	Pitching moment M_Z (Nm)
20	90	156.2	0.214	3,805	6,120	25,385	12,276
		120.9	0.275	2,885	4,902	15,101	8,874
		79.6	0.430	1,927	4,066	7,299	6,072
	120	163.2	0.200	3,897	19,331	23,361	11,020
		148.2	0.226	3,605	16,733	19,718	10,047
		133.5	0.249	3,182	13,949	16,191	8,584
		114.1	0.305	2,840	11,240	11,841	7,451
		92.9	0.369	2,262	8,456	8,091	6,088
39	0	151.0	0.421	6,951	-16,338	-236	-178
		138.6	0.454	6,275	-13,308	-156	-152
		121.1	0.528	5,536	-9,105	-178	-267
		105.4	0.611	4,829	-6,067	-169	-240
		72.0	0.896	3,292	-2,193	-151	-117
	20	152.4	0.403	6,812	-15,141	9,719	7,466
		115.4	0.518	4,929	-7,393	6,094	5,697
		67.6	0.862	2,767	-1,588	3,065	3,819
	60	152.2	0.419	7,047	102	24,090	19,044
		139.1	0.456	6,365	1,326	20,536	17,391
		117.9	0.541	5,364	2,945	15,435	14,698
		94.9	0.676	4,309	4,195	11,089	12,134
		73.4	0.883	3,346	4,968	8,376	10,222
	75	138.4	0.459	6,335	8,104	21,880	19,181
		115.9	0.557	5,302	8,198	16,191	16,027
		85.1	0.760	3,883	7,819	10,622	12,214
	90	161.1	0.390	7,384	15,052	27,956	22,473
		147.8	0.431	6,837	14,216	23,561	20,358
		132.8	0.485	6,174	13,273	19,678	18,565
		115.0	0.557	5,279	11,667	14,954	15,720
		100.7	0.649	4,608	10,689	12,272	14,126

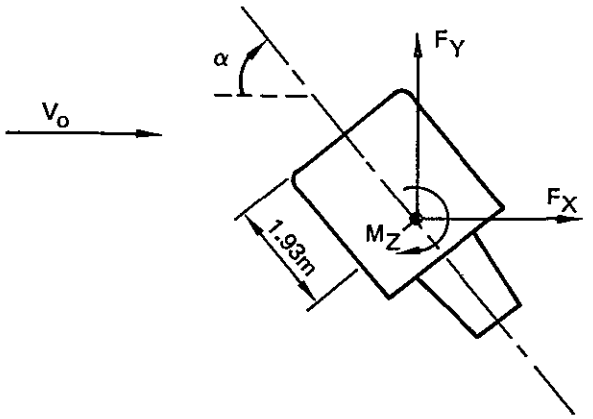

Table 1. Force Data (Concluded)

V_o (m/s)	α (degrees)	WK1A (kg/sm^2)	V_o/V_H	Ram drag F_R (N)	Streamwise force F_X (N)	Lift force F_Y (N)	Pitching moment M_Z (Nm)
54	0	138.5	0.642	8,916	-10,466	-374	-431
		120.8	0.743	7,752	-6,650	-307	-355
		90.9	0.991	5,800	-2,046	-351	-439
	20	145.8	0.590	9,084	-10,328	10,435	10,735
		115 8	0.739	7,077	-4,893	7,410	8,741
		60.7	1.404	3,634	992	4,030	5,829
	60	155.7	0.565	10,001	6,748	28,285	27,694
		141.9	0.625	9,137	7,909	23,966	25,448
		118.0	0.753	7,547	9,127	18,179	21,273
		97.4	0.931	6,299	10,119	14,456	18,442
	75	162.0	0.537	10,268	15,893	32,275	30,997
		149.4	0.587	9,462	15,786	28,289	28,834
		131.7	0.672	8,362	15,501	23,526	25,574
		122.0	0.728	7,729	15,194	21,084	23,905
72	0	164.6	0.714	14,094	-13,090	-214	-583
		152.5	0.775	13,014	-10,199	-325	-608
		133.8	0.893	11,486	-6,116	-467	-692
		115.2	1.045	9,891	-2,615	-525	-807
		96.3	1.259	8,254	-209	-534	-917
		79.6	1.524	6,803	1,241	-512	-810
	20	149.6	0.787	12,770	-6,668	13,384	16,352
		117.2	1.006	9,907	-845	9,906	13,660
		75.5	1.566	6,332	3,176	6,908	10,521
	45	168.4	0.698	14,463	3,701	31,781	35,280
		151.7	0.781	12,991	5,907	27,680	32,441
		137.6	0.852	11,603	7,126	24,242	29,466
		119.6	0.990	10,109	9,434	20,390	26,336
		102.9	1.154	8,686	11,098	17,685	23,555
		89.4	1.343	7,570	12,010	16,275	21,902
	60	158.1	0.708	12,918	13,771	32,684	36,543
		137.0	0.823	11,178	14,870	26,608	32,345
		122.9	0.920	9,989	15,568	22,845	29,519

ORIGINAL PAGE IS
OF POOR QUALITY

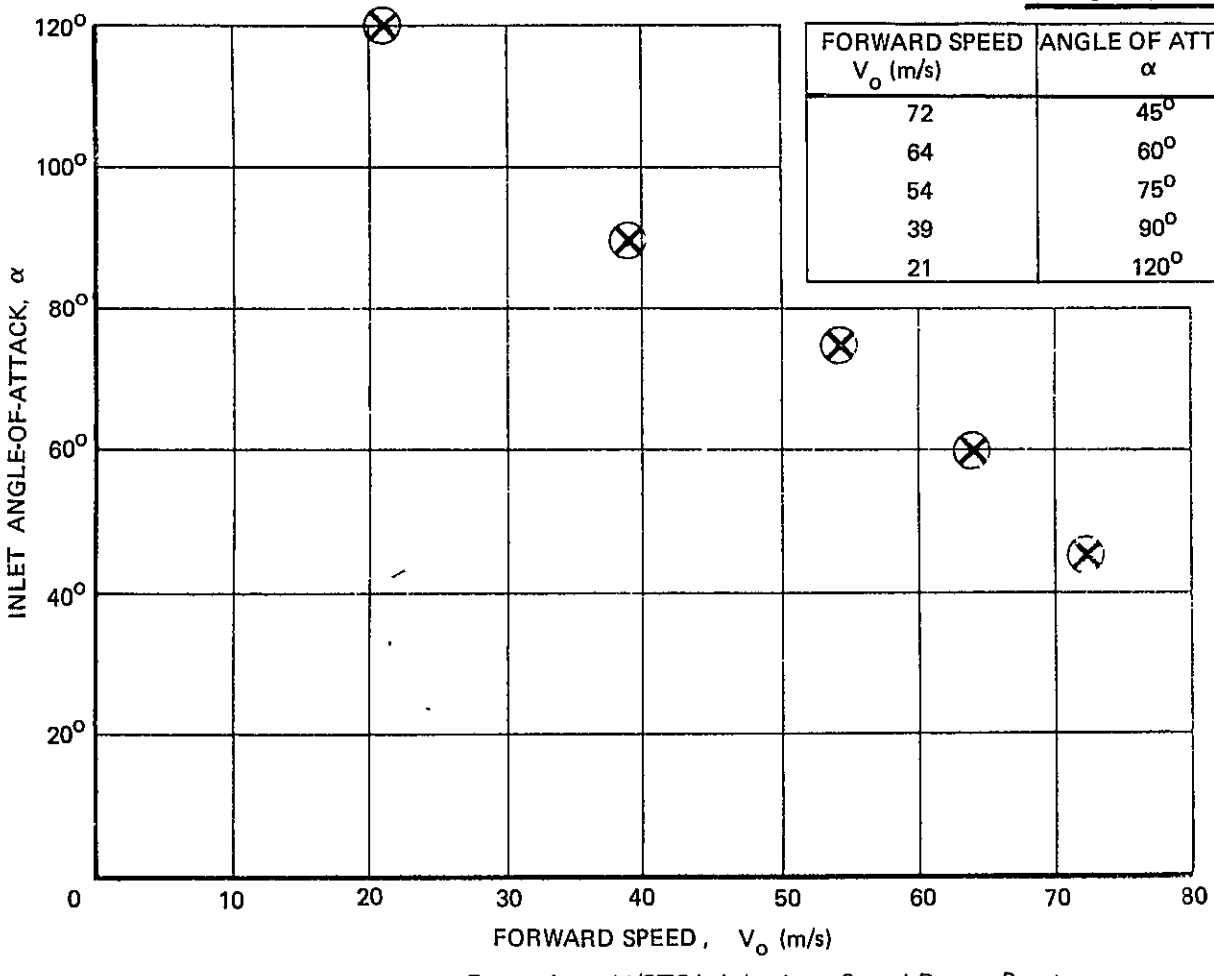

DESIGN CONDITIONS

FORWARD SPEED V_o (m/s)	ANGLE OF ATTACK α	AIRFLOW RANGE WKIA (kg/sm^2)
72	45°	73 - 146
64	60°	78 - 151
54	75°	103 - 176
39	90°	127 - 205
21	120°	132 - 205

Figure 1 V/STOL Inlet Low Speed Design Points

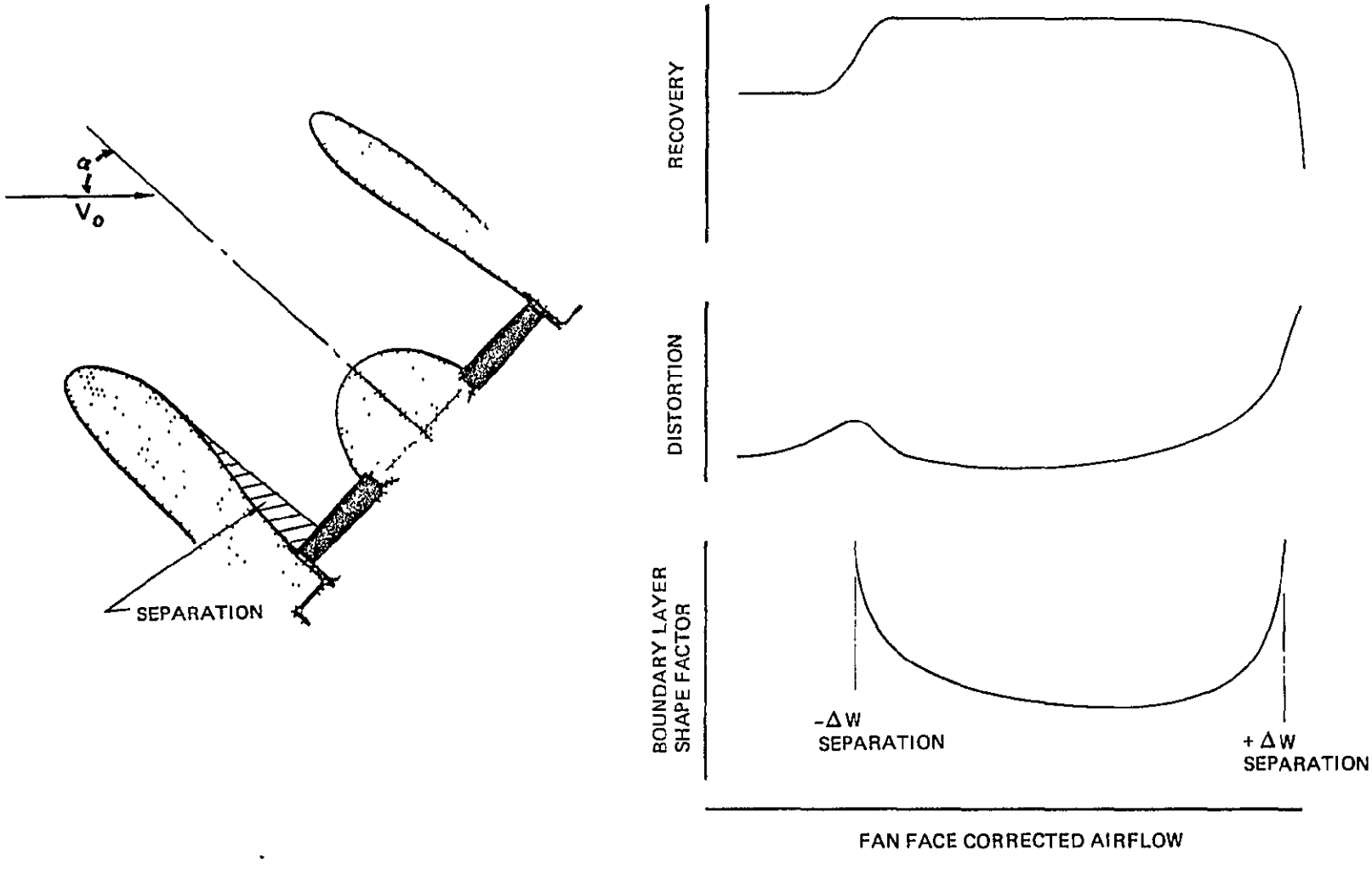

Figure 2. Effects of Flow Separation on Inlet Performance

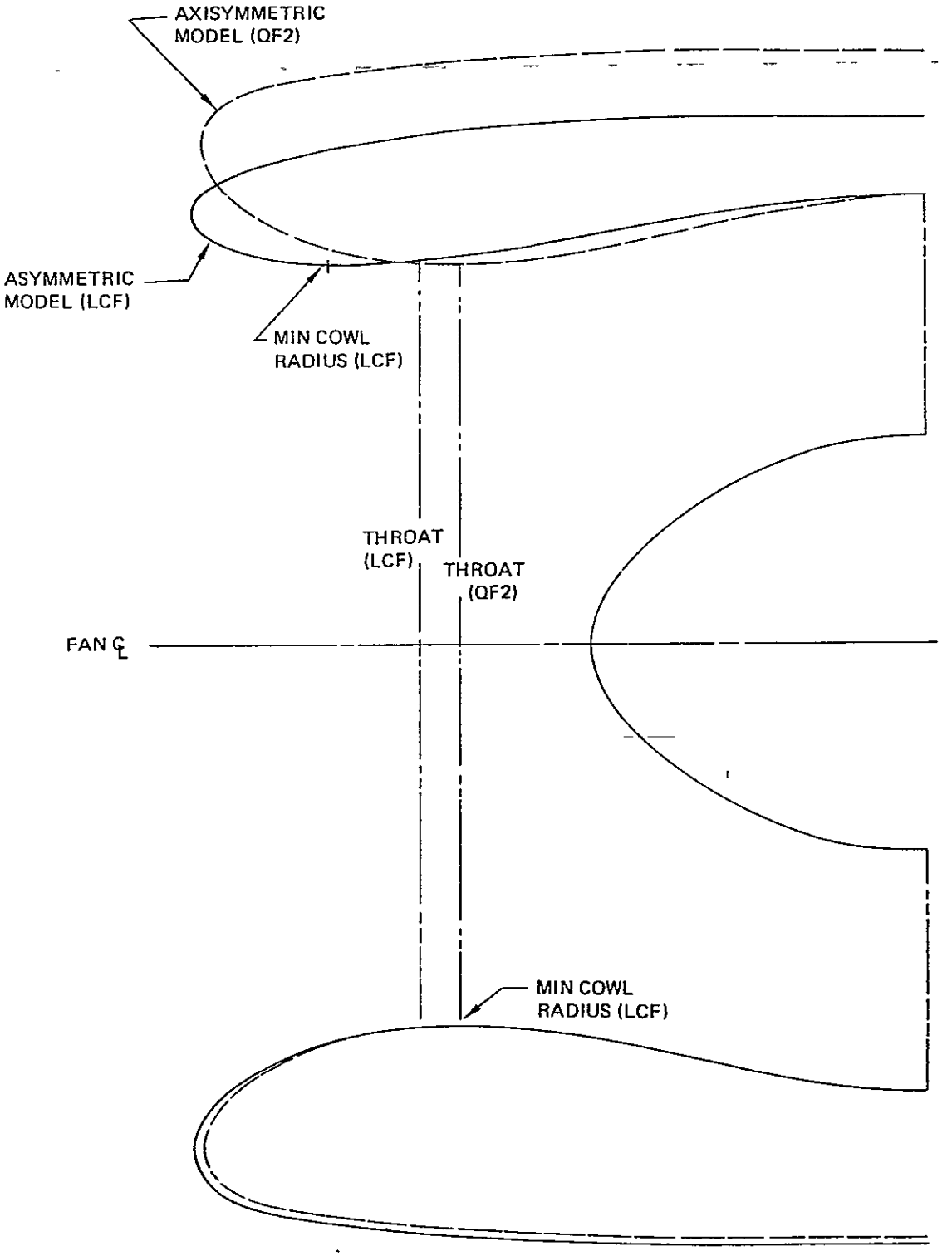

Figure 3. LCF Inlet Schematic

ORIGINAL PAGE IS
OF POOR QUALITY

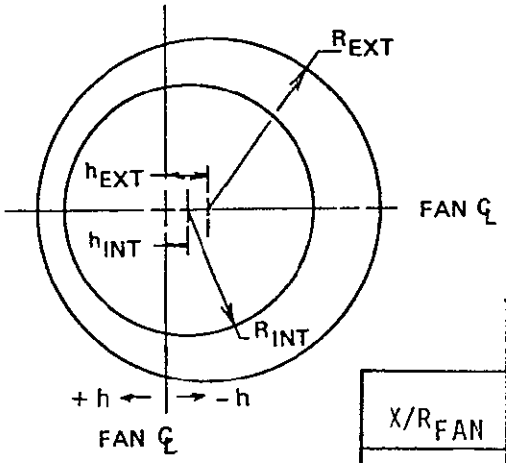

R_{FAN} = .6985 m , X = 0 at hilite

HAMILTON STANDARD SPINNER CONTOURS	
X/R_{FAN}	R/R_{FAN}
.8863	0
.8877	.0222
.8892	.0306
.8921	.0431
.8936	.0479
.9008	.0680
.9154	.0992
.9299	.1247
.9590	.1668
.9954	.2092
1.0317	.2434
1.1045	.2997
1.1772	.3452
1.2499	.3819
1.3227	.4115
1.3954	.4339
1.4681	.4496
1.5408	.4597
1.6136	.4618
1.6368	.4618

	EXTERNAL COWL		INTERNAL COWL	
X/R_{FAN}	R_{EXT}/R_{FAN}	h_{EXT}/R_{FAN}	R_{INT}/R_{FAN}	h_{INT}/R_{FAN}
0	1.0514	-.0759	1.0514	-.0759
.0025	1.0700	-.0845	1.0316	-.0752
.0082	1.0848	-.0883	1.0160	-.0719
.0157	1.0971	-.0913	1.0023	-.0687
.0346	1.1172	-.0951	.9793	-.0632
.0535	1.1308	-.0968	.9622	-.0585
.0817	1.1460	-.0978	.9425	-.0528
.1100	1.1576	-.0978	.9269	-.0476
.1384	1.1672	-.0973	.9140	-.0429
.1667	1.1751	-.0964	.9032	-.0384
.2232	1.1882	-.0943	.8864	-.0301
.2799	1.1977	-.0925	.8748	-.0221
.3364	1.2084	-.0909	.8671	-.0144
.3931	1.2165	-.0896	.8622	-.0077
.4497	1.2237	-.0885	.8595	-.0019
.5063	1.2300	-.0875	.8588	.0031
.5629	1.2357	-.0867	.8601	.0073
.6195	1.2406	-.0860	.8632	.0106
.6761	1.2449	-.0855	.8680	.0131
.7327	1.2487	-.0849	.8742	.0148
.7839	1.2519	-.0845	.8816	.0158
.8459	1.2545	-.0842	.8901	.0162
.9591	1.2585	-.0837	.9093	.0155
1.0723	1.2605	-.0834	.9301	.0132
1.1463	1.2609	-.0833	.9439	.0112
1.1640			.9471	.0107
1.2731			.9659	.0073
1.3822			.9819	.0041
1.4913			.9937	.0015
1.6004			.9996	.0001
1.6368			1.0000	.0000

Figure 4. LCF Inlet Contours

ORIGINAL PAGE IS
OF POOR QUALITY

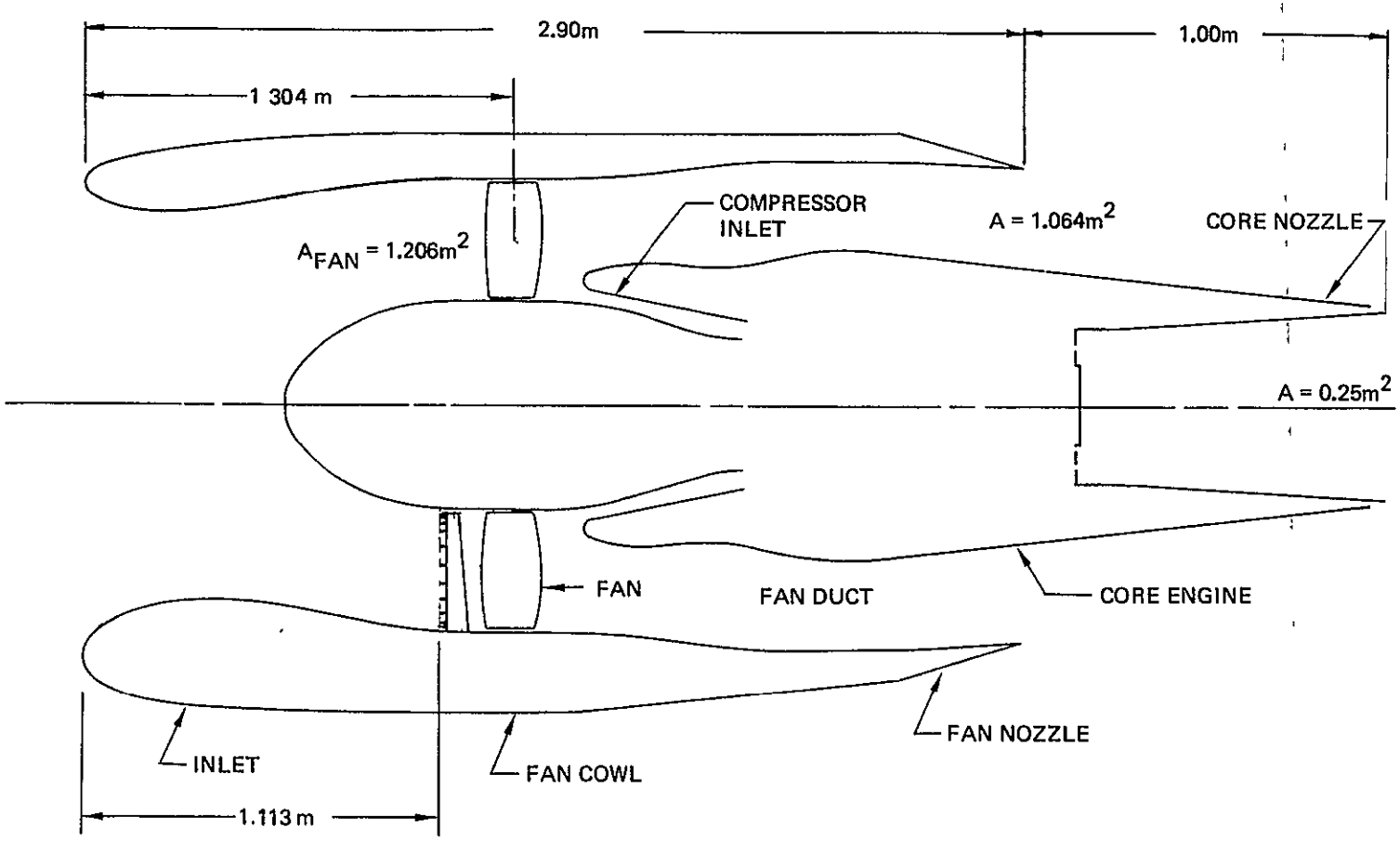

Figure 5. Nacelle Schematic

ORIGINAL PAGE IS
OF POOR QUALITY

LEEWARD (0°) COWL STATIC PRESSURES			
P_C NO.	X/R_{FAN}	R_L/R_{FAN}	S/R_{FAN}
1	.1242	1.0650	-.1628
2	.0466	1.0300	-.0775
3	.0137	1.0036	-.0352
4	.0021	.9844	-.0127
5	0	.9719	0
6	.0007	.9640	.0079
7	.0042	.9519	.0205
8	.0109	.9399	.0343
9	.0209	.9280	.0499
10	.0500	.9057	.0865
11	.1048	.8810	.1468
12	.1817	.8620	.2261
13	.2987	.8524	.3436
14	.4445	.8573	.4895
15	.5954	.8709	.6410
16	.8136	.9011	.8613
17	1.0317	.9368	1.0824
18	1.3590	.9836	1.4130

WINDWARD (180°) COWL STATIC PRESSURES			
P_C NO.	X/R_{FAN}	R_L/R_{FAN}	S/R_{FAN}
19	.1242	1.2602	- 1932
20	.0466	1.2227	-.1067
21	.0137	1.1849	- 0563
22	.0021	1 1527	- 0220
23	0	1.1308	0
24	.0007	1.1183	.0125
25	.0042	1.0999	0313
26	.0109	1.0811	.0513
27	.0209	1.0619	.0729
28	.0500	1.0244	1204
29	.1048	.9781	.1923
30	.1817	.9342	.2809
31	.2936	.8927	4003
32	.4445	.8619	.5545
33	.5954	.8524	.7058
34	.8136	.8691	.9248
35	1.0317	.9084	1.1465
36	1.3590	9741	1.4803
PDS	.4445	.8619	5545

SIDE COWL STATIC PRESSURES			
P_C NO.	X/R_{FAN}	R_L/R_{FAN}	ψ
37	4982	8588	90°
38	4982	8588	270°

FAN FACE COWL STATIC PRESSURES			
P_C NO.	X/R_{FAN}	R_L/R_{FAN}	ψ
39	1.5931	1.0	15.7°
40	↓	↓	67.1
41			118.6
42			170.0
43			221.4
44			272 9
45			324.3

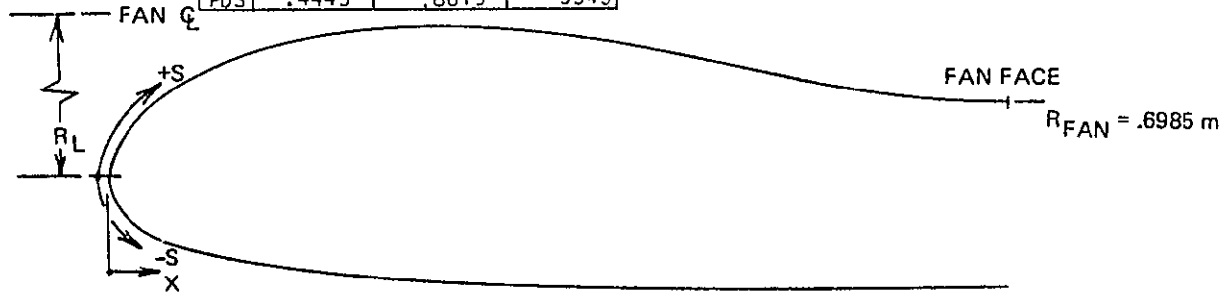

Figure 6 Cowl Static Pressure Instrumentation

FAN FACE RAKE PROBE COORDINATES
AND NUMBERING

	RAKE 1	RAKE 2	RAKE 3	RAKE 4	RAKE 5	RAKE 6	RAKE 7	RING RADIUS R/R_{FAN}	% AREA FOR RING
RING 1	PTF 1	PTF 11	PTF 21	PTF 31	PTF 41	PTF 51	PTF 61	.9901	5%
RING 2	2	12	22	32	42	52	62	.9700	5%
RING 3	3	13	23	33	43	53	63	.9286	15%
RING 4	4	14	24	34 [1]	44	54	64	.8627	15%
RING 5	5	15	25	35	45	55	65	.7914	15%
RING 6	6	16	26	36	46	56	66	.7129	15%
RING 7	7	17	27	37	47	57	67	.6247	15%
RING 8	8	18	28	38	48	58	68	.5582	5%
RING 9	9	19	29	39 [2]	49	59	69	.5218	5%
	PP1	PP2	PP3	PP4	PP5	PP6	PP7	.5017	--
RING 10	10	20	30	40 [3]	50	60	70	.4813	5%
RAKE ANGLE (deg)	25.7	77.1	128.6	180.0	213.4	282.3	334.3		

1 PDF 1
2 PDF 2
3 PDF 3

} Dynamic total pressure probe mounted side by side with steady state probe

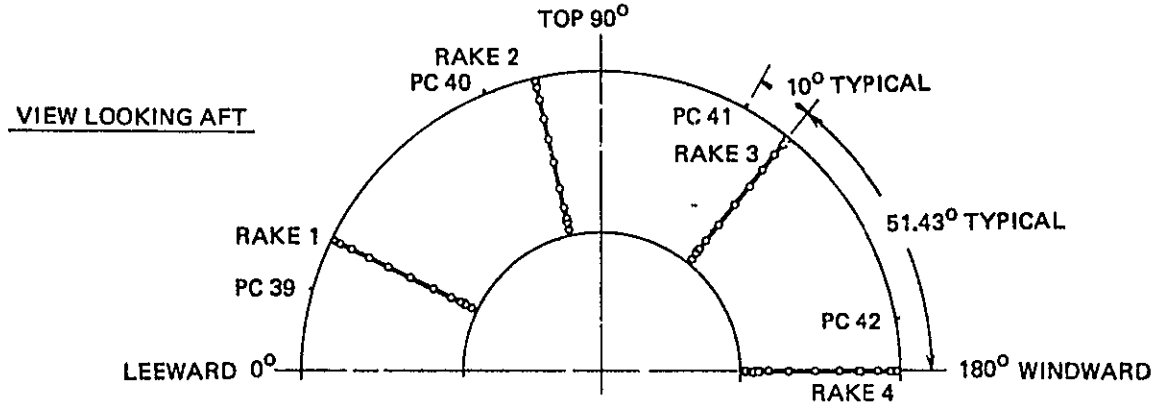

Figure 7. Fan Face Instrumentation

0° PROBES	180° PROBES	RADIUS R/R_{FAN}	ΔA/AR
NOZZLE WALL	NOZZLE WALL	1.0676	
PM1	PM3	1.0640	
PTM1	PTM11	1.0447	.142
PTM2	PTM12	.9964	.134
TTM1	TTM4	.9738	
PTM3	PTM13	.9513	.121
PTM4	PTM14	.9084	.110
PTM5	PTM15	.8676	.100
PTM6	PTM16	.8287	.091
TTM2	TTM5	.8102	
PTM7	PTM17	.7916	.083
PTM8	PTM18	.7556	.077
PTM9	PTM19	.7211	.071
TTM3	TTM6	.7044	
PTM10	PTM20	.6876	.073
PM2	PM4	.6767	
CORE CASE	CORE CASE	.6676	

ΔA: Area assigned to total pressure probe

AR: Flow area at rake face = 1.064 m^2

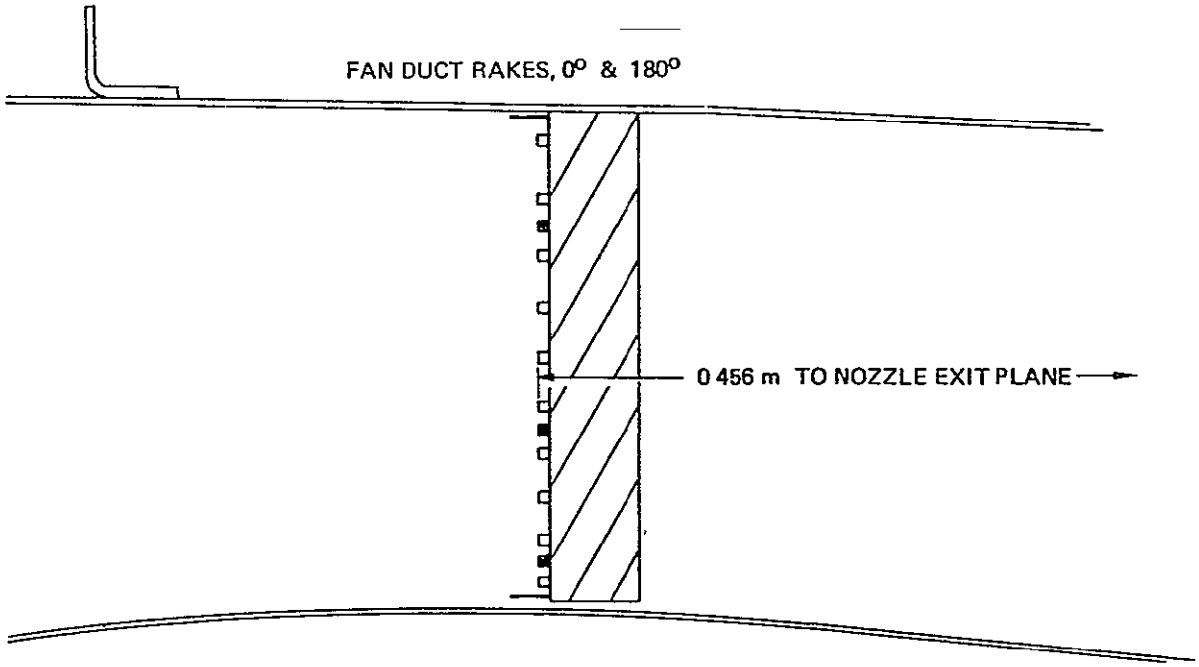

Figure 8. Fan Duct Instrumentation

ORIGINAL PAGE IS
OF POOR QUALITY

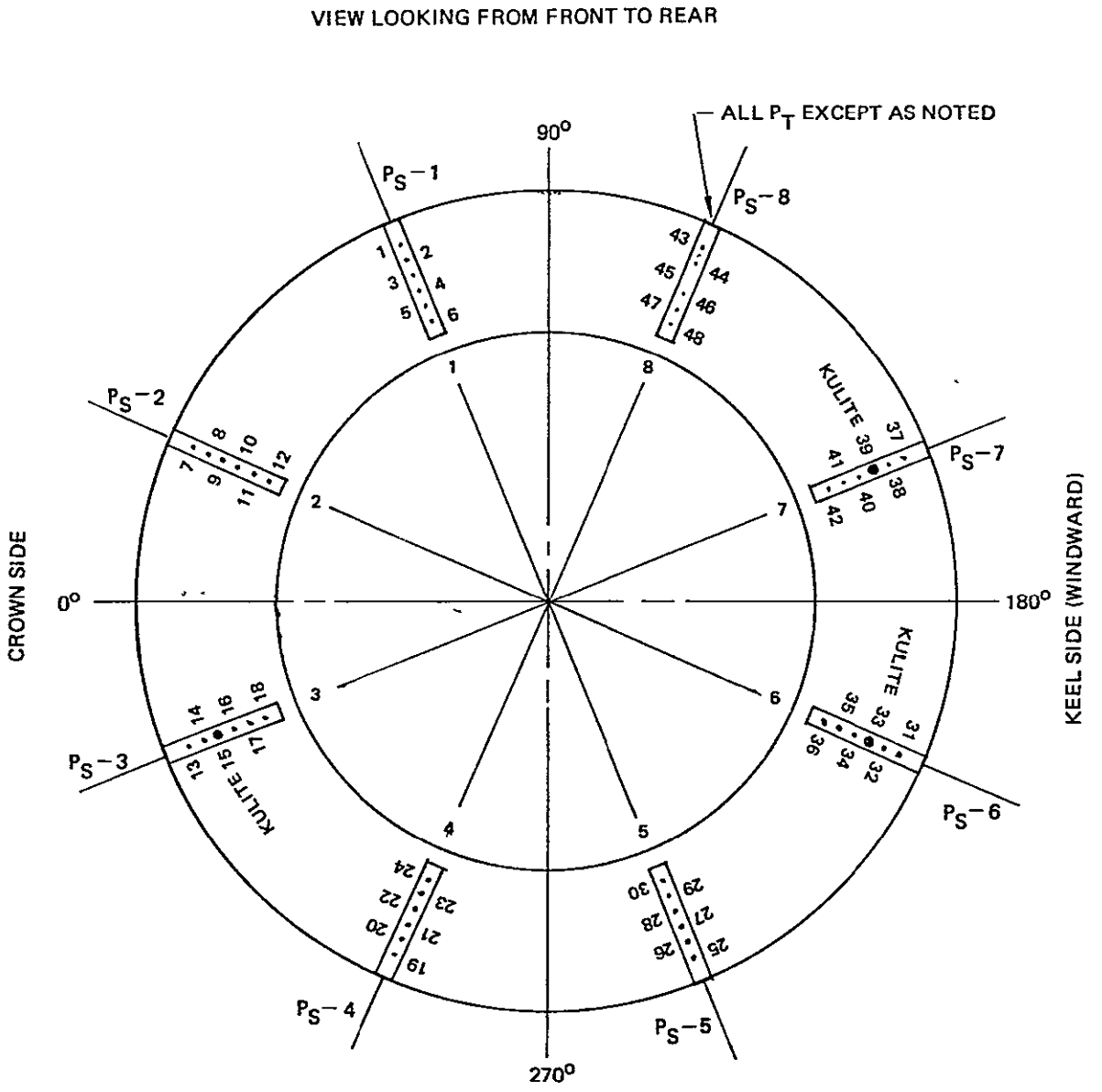

Figure 9. Compressor Face Instrumentation

ORIGINAL PAGE IS
OF POOR QUALITY

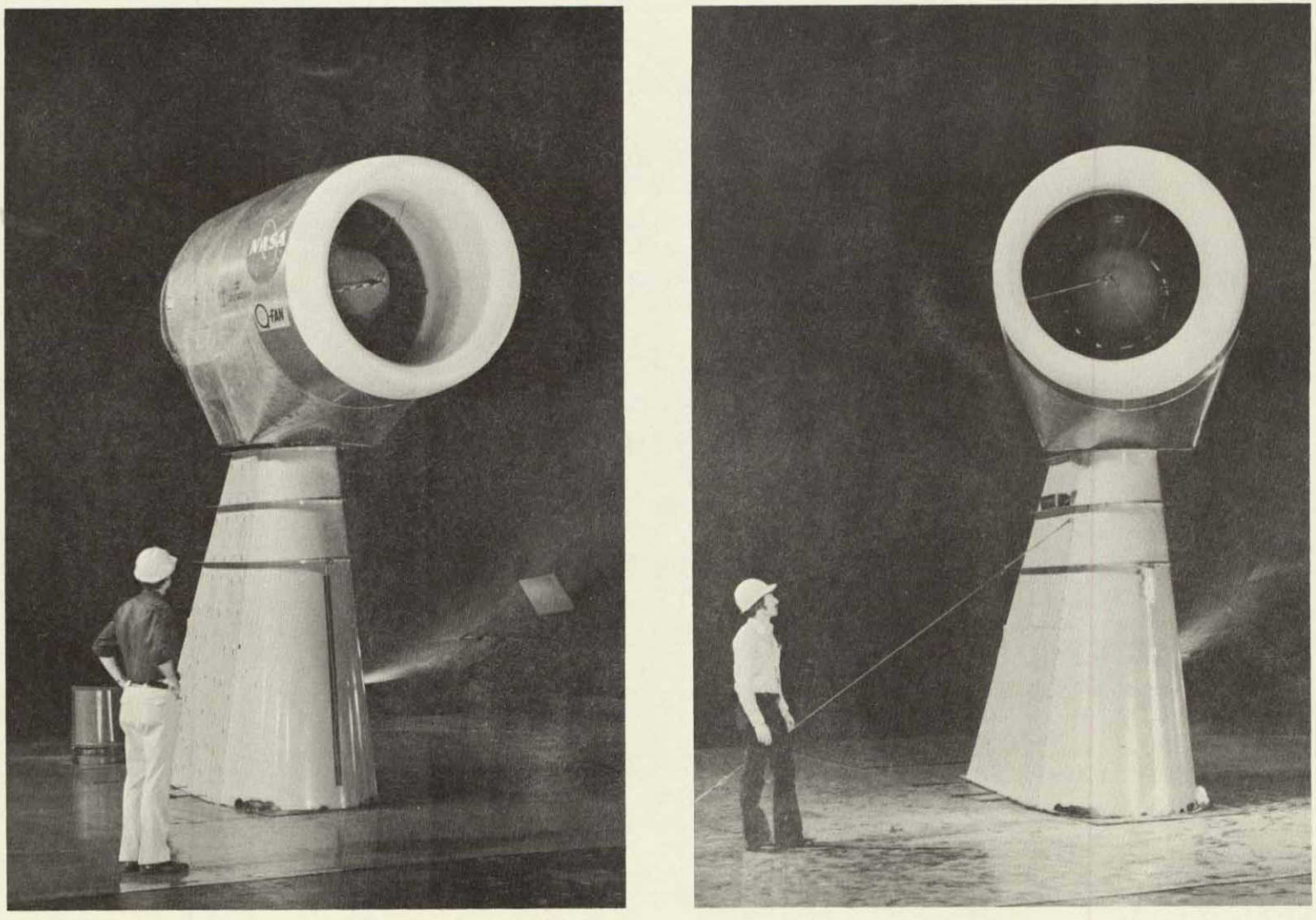

Figure 10. Nacelle Installed in 40-by80-ft Wind Tunnel

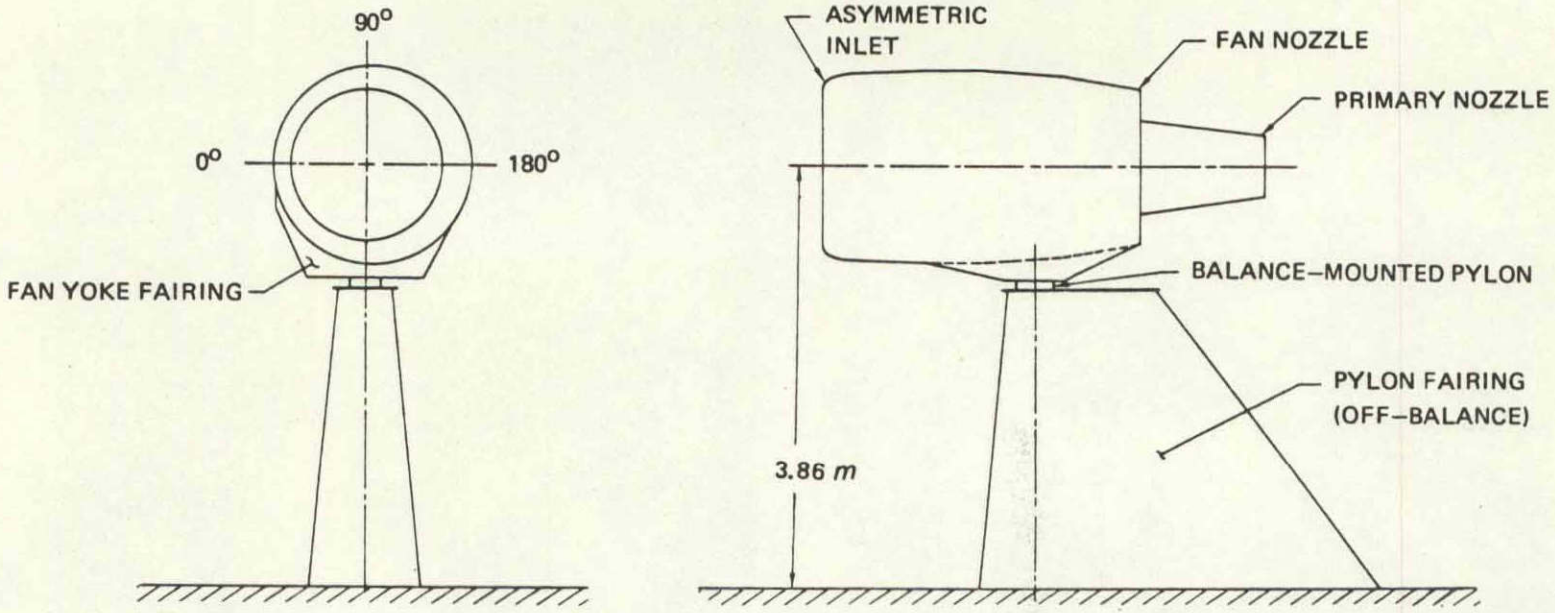

Figure 11. Wind Tunnel Installation Schematic

RUN, C.P.	V_o (m/s)	WKIA (kg/sm^2)
6–1	55.5	90
2	55.2	90
3	55.0	86
4	54 5	106
5	54.2	105
6	54.1	105
7	53.2	127
8	52.9	126
9	52.3	142
10	51.9	140
11	51.6	140

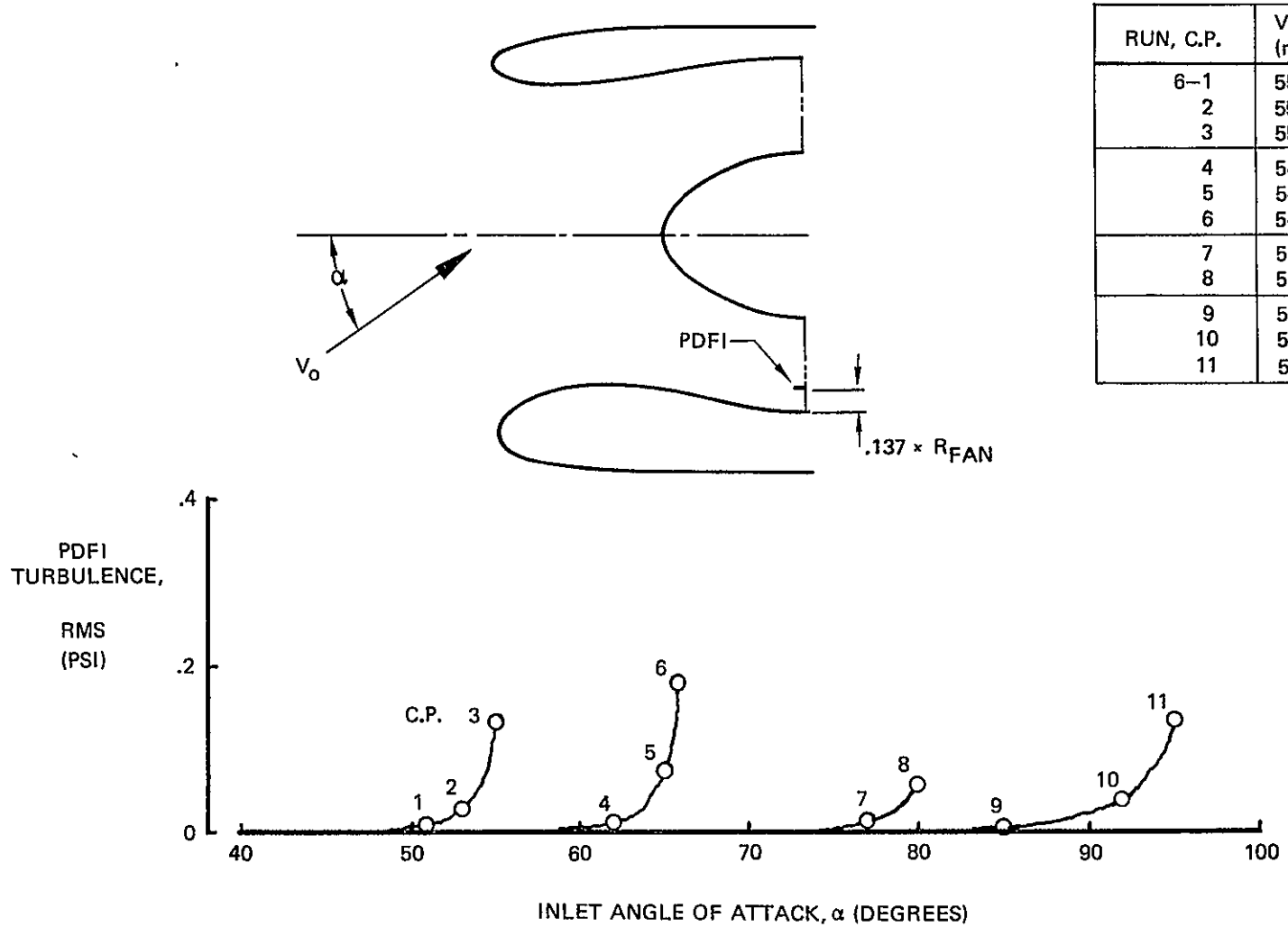

Figure 13. On-Line Display of Inlet Boundary Layer Separation

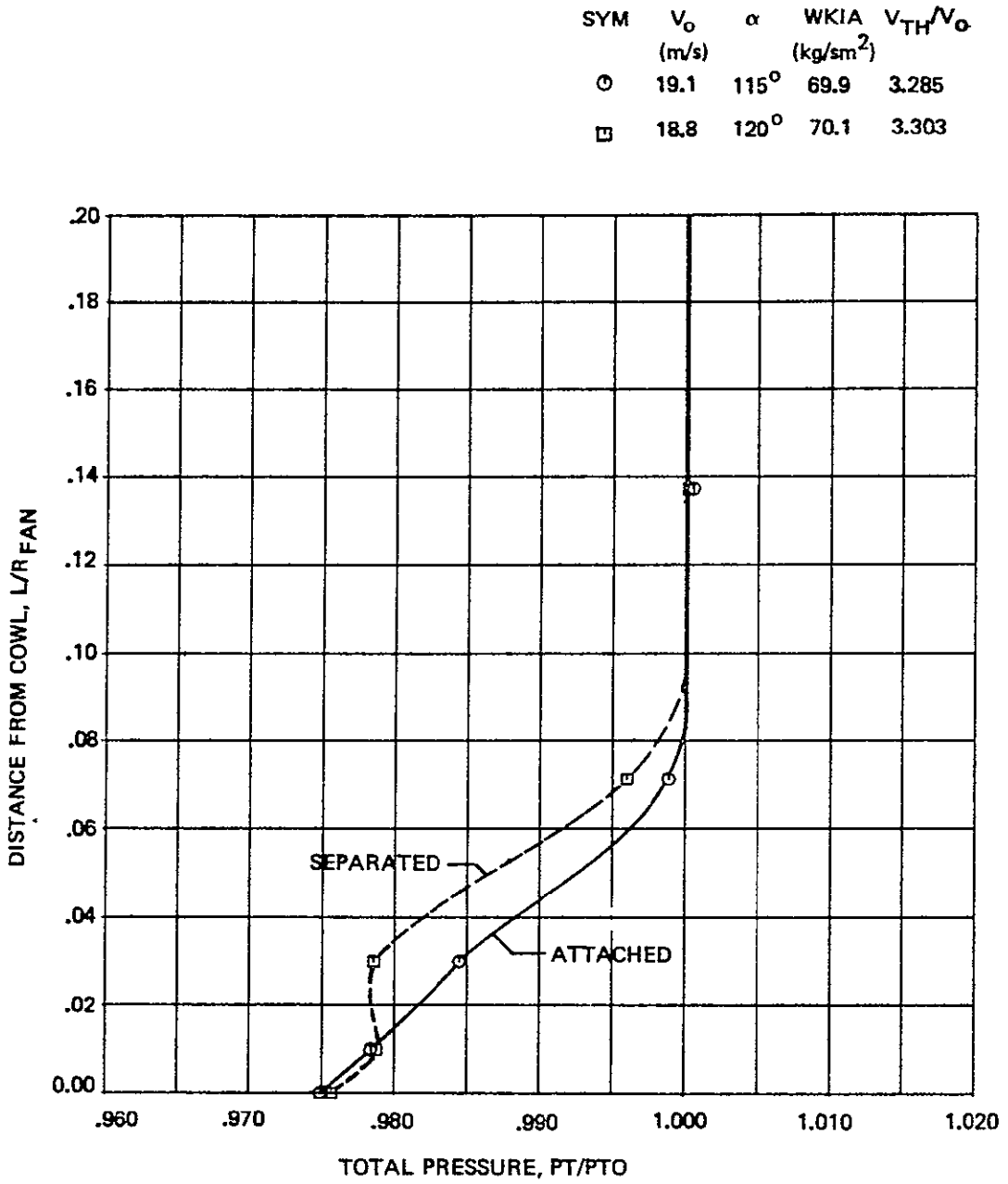

Figure 14. Fan Face Total Pressure Profiles, Windward Rake. Run No. 4, Conditions 2 and 3

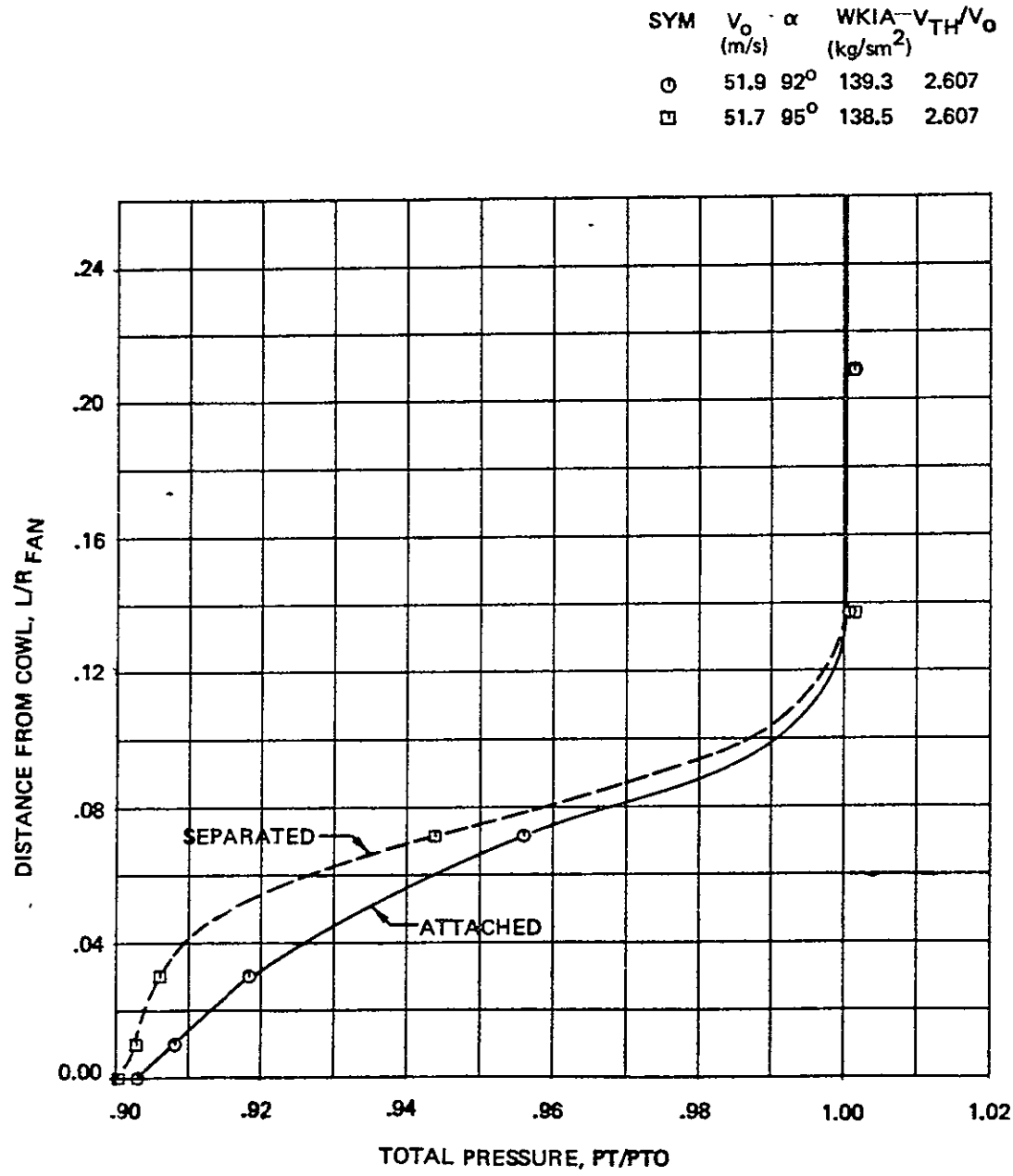

Figure 15. Fan Face Total Pressure Profiles. Windward Rake, Run No. 6, Conditions 10 and 11

ORIGINAL PAGE IS
OF POOR QUALITY

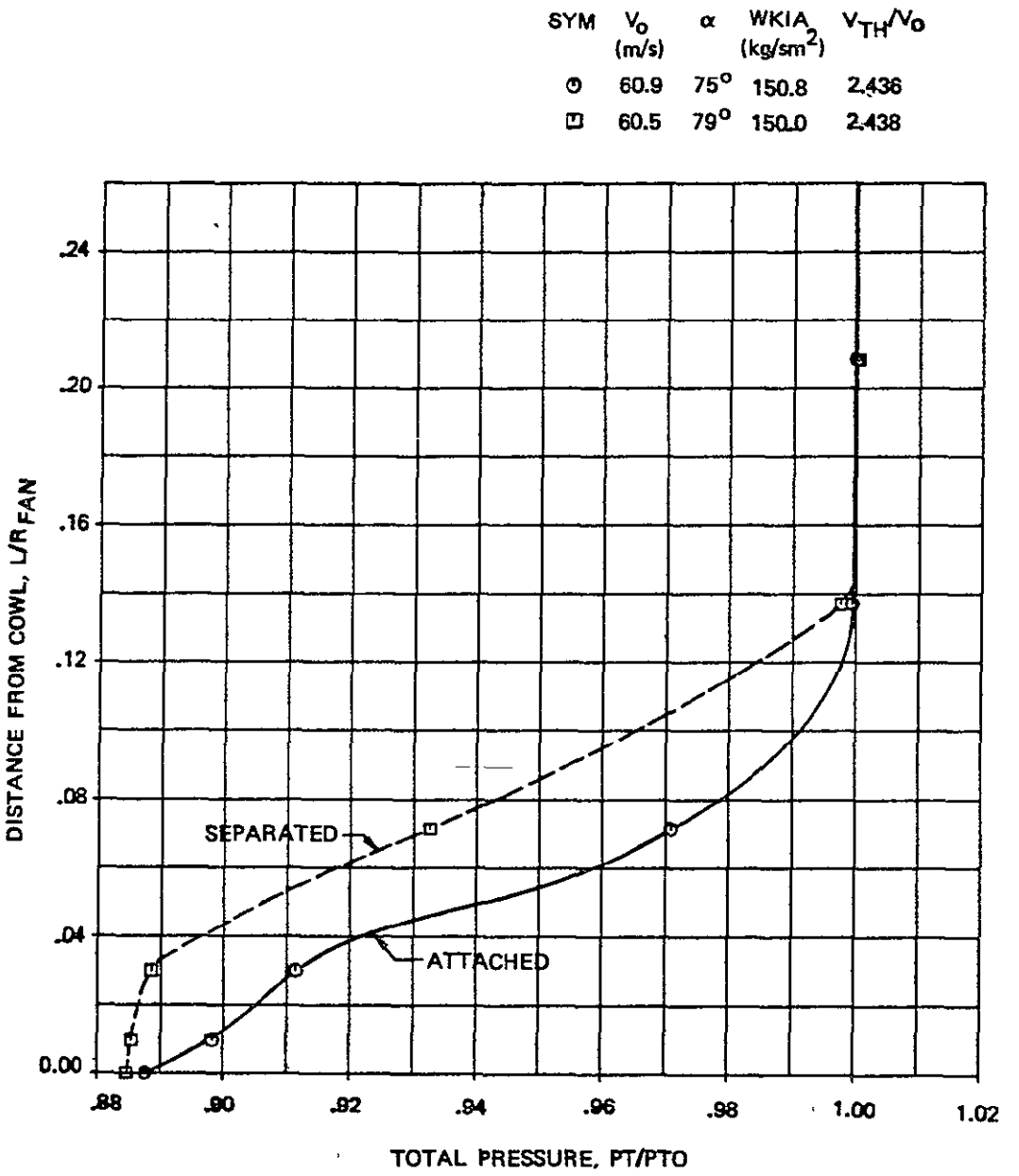

Figure 16. Fan Face Total Pressure Profiles, Windward Rake Run No. 32 Conditions 14 and 16

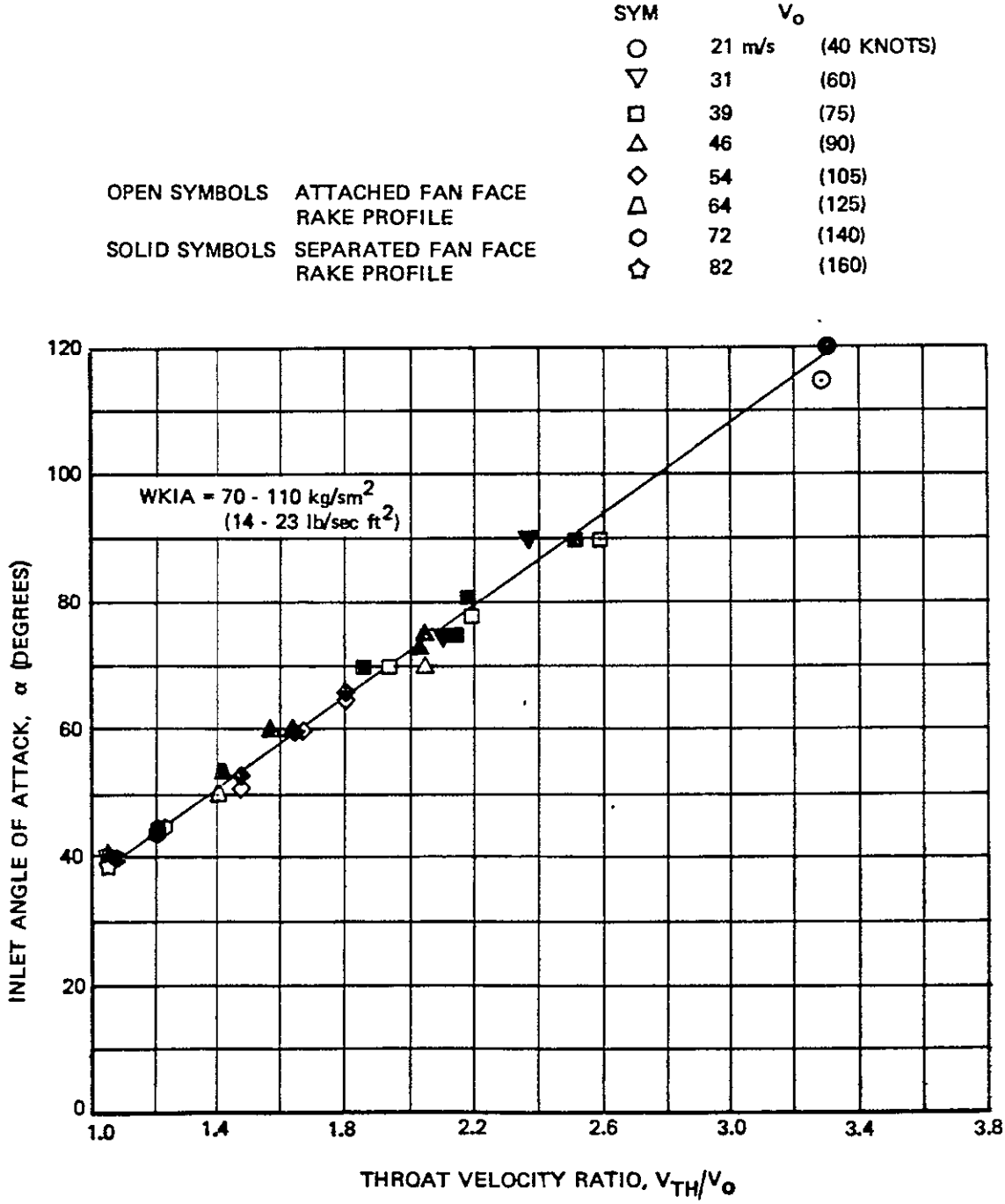

Figure 17. Inlet Separation Boundaries, Low Airflows

ORIGINAL PAGE IS
OF POOR QUALITY

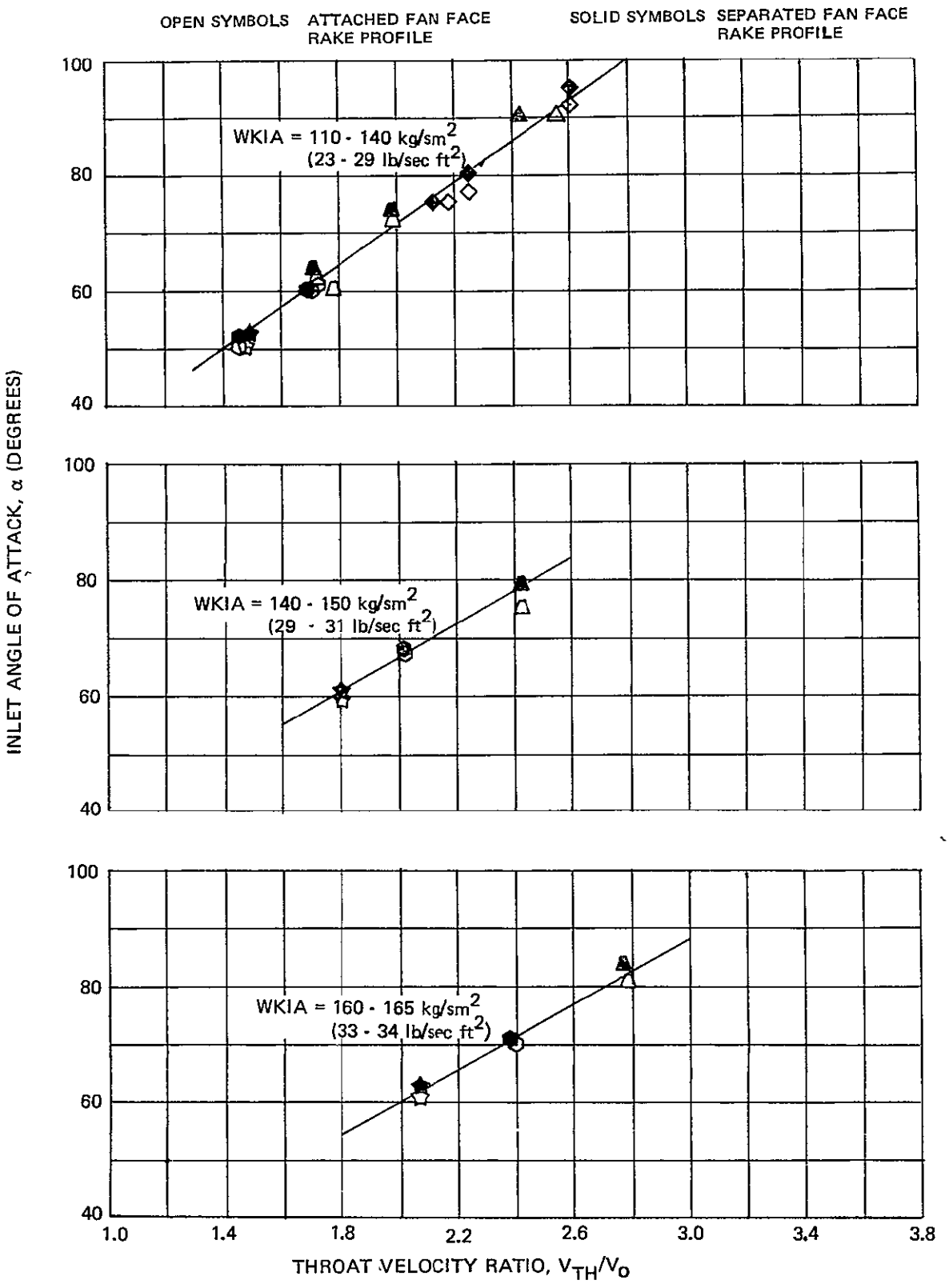

Figure 18. Inlet Separation Boundaries, Medium and High Airflows

ORIGINAL PAGE IS
OF POOR QUALITY

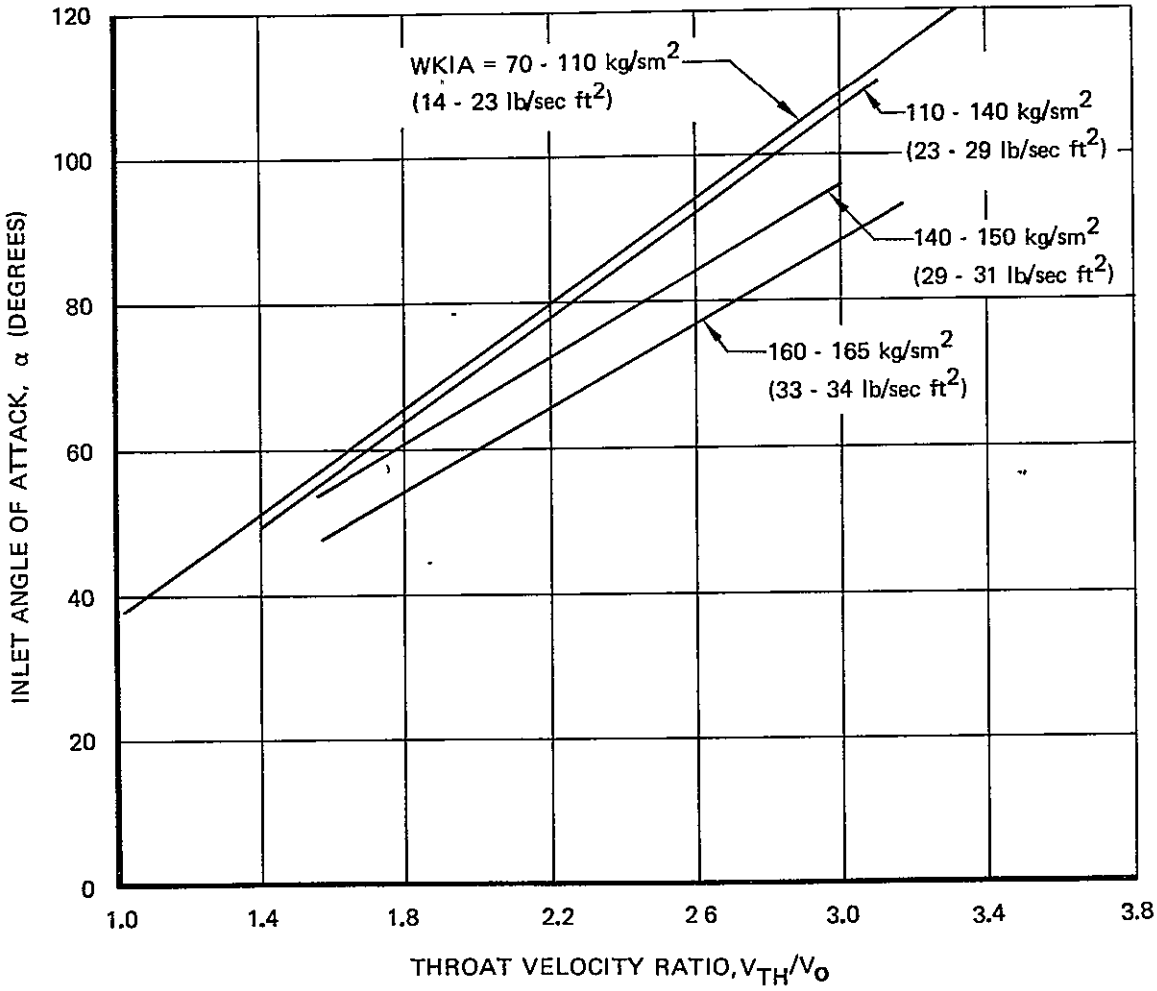

Figure 19. Inlet Separation Boundaries

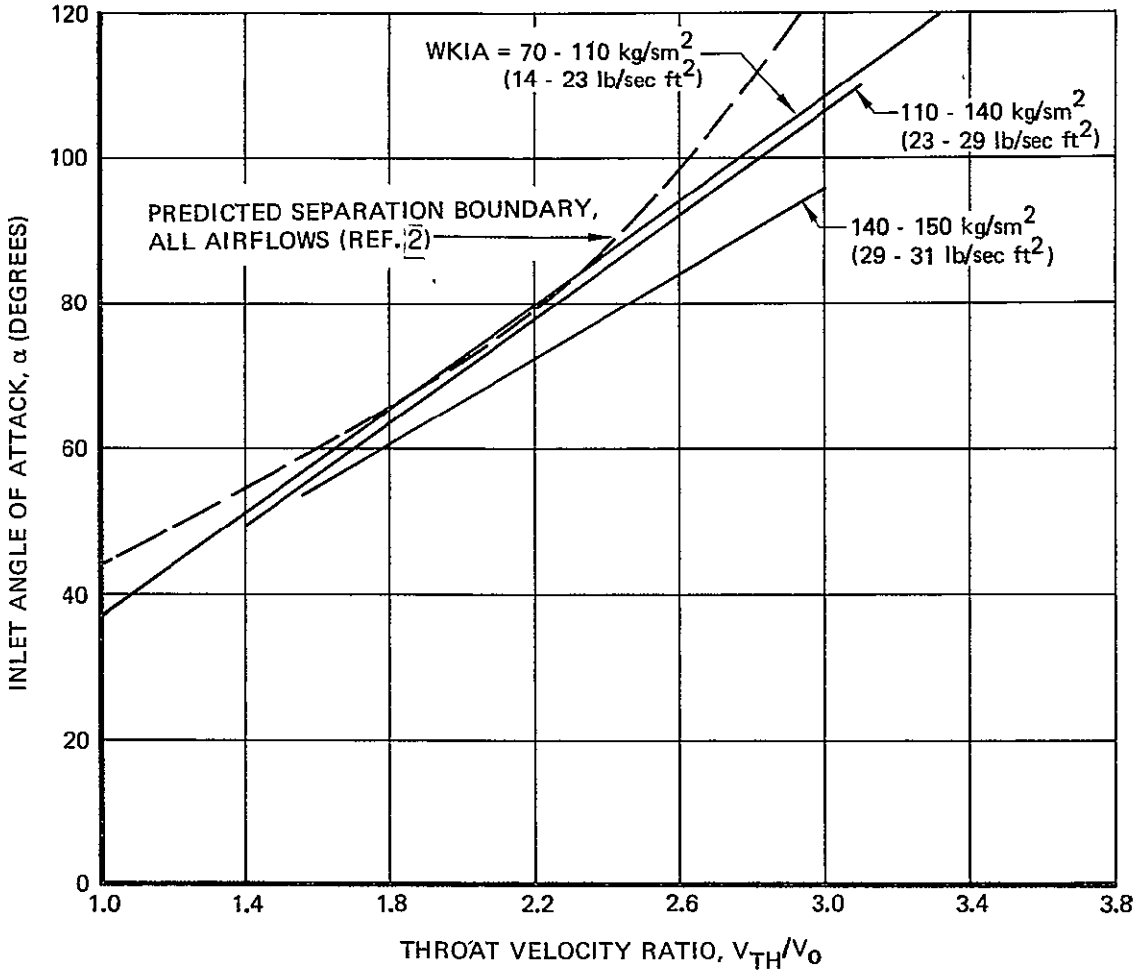

Figure 20 Inlet Separation Boundaries. Comparison with Empirical Prediction.

ORIGINAL PAGE IS
OF POOR QUALITY

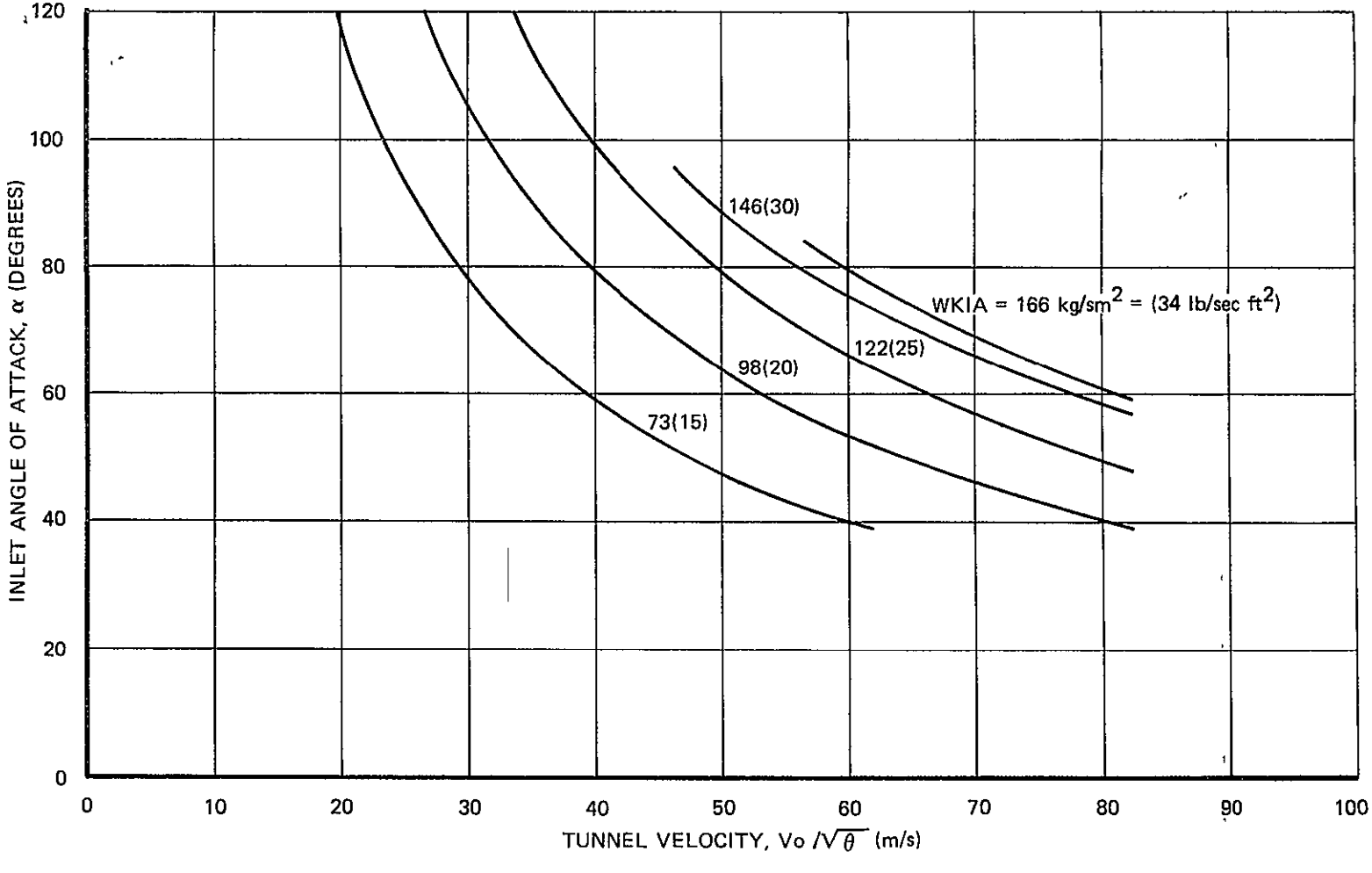

Figure 21. Separation Boundaries

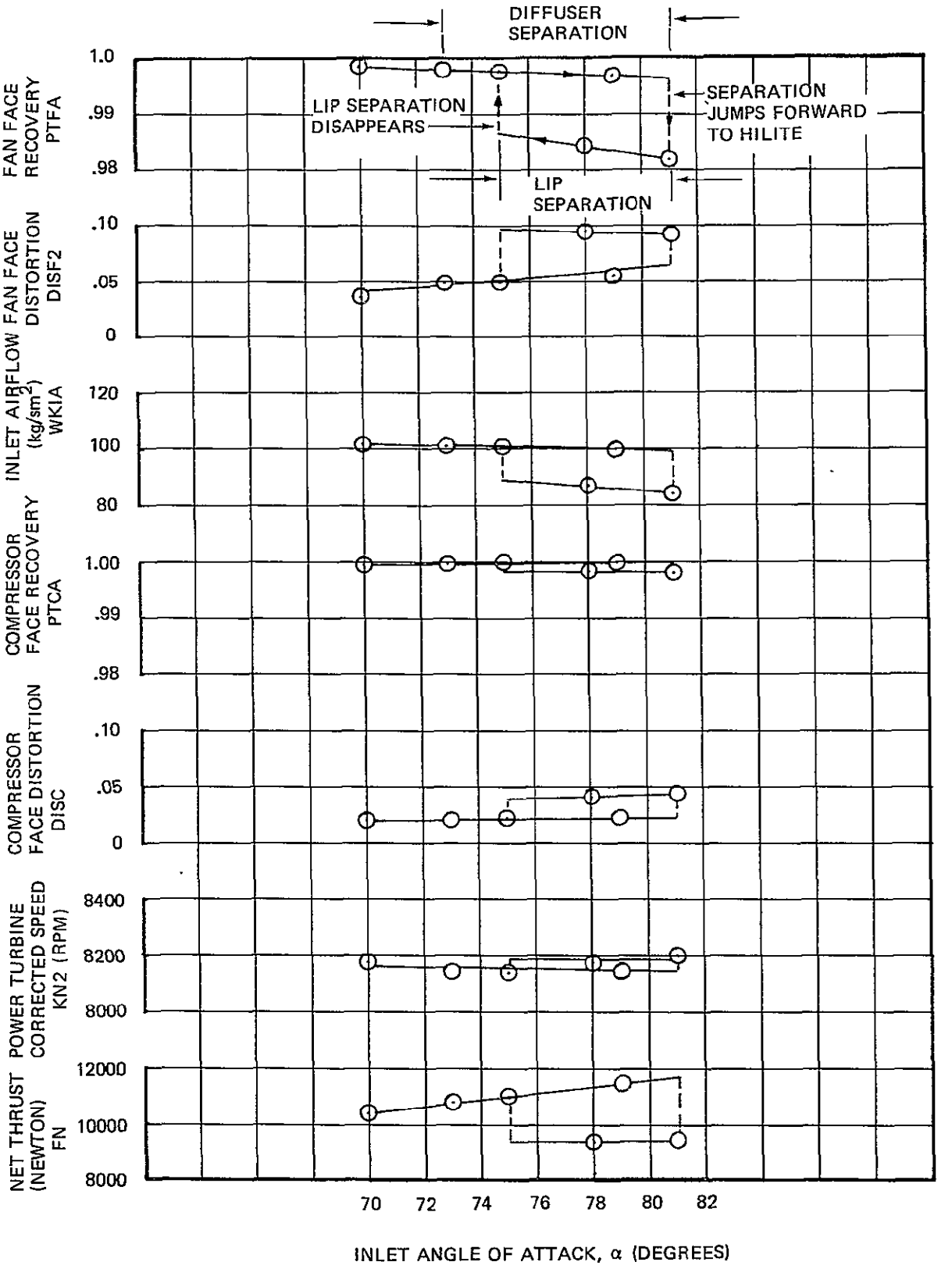

Figure 22. Performance Characteristics During Separation
V_0 = 45 m/s, WKIA = 100 kg/sm²

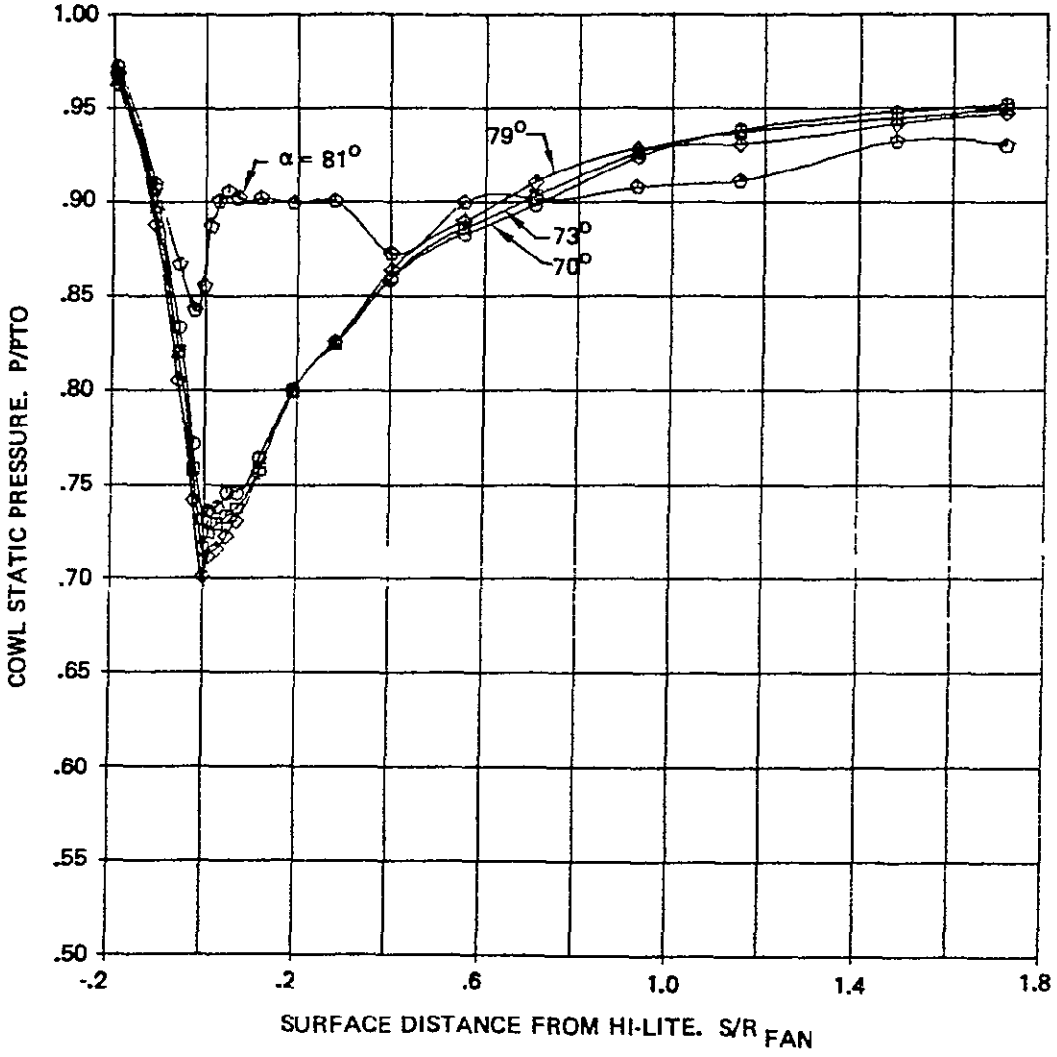

Figure 23. Windward Cowl Static Pressure Profiles. V_o *= 45 m/s, WKIA = 100 kg/sm*^{2}

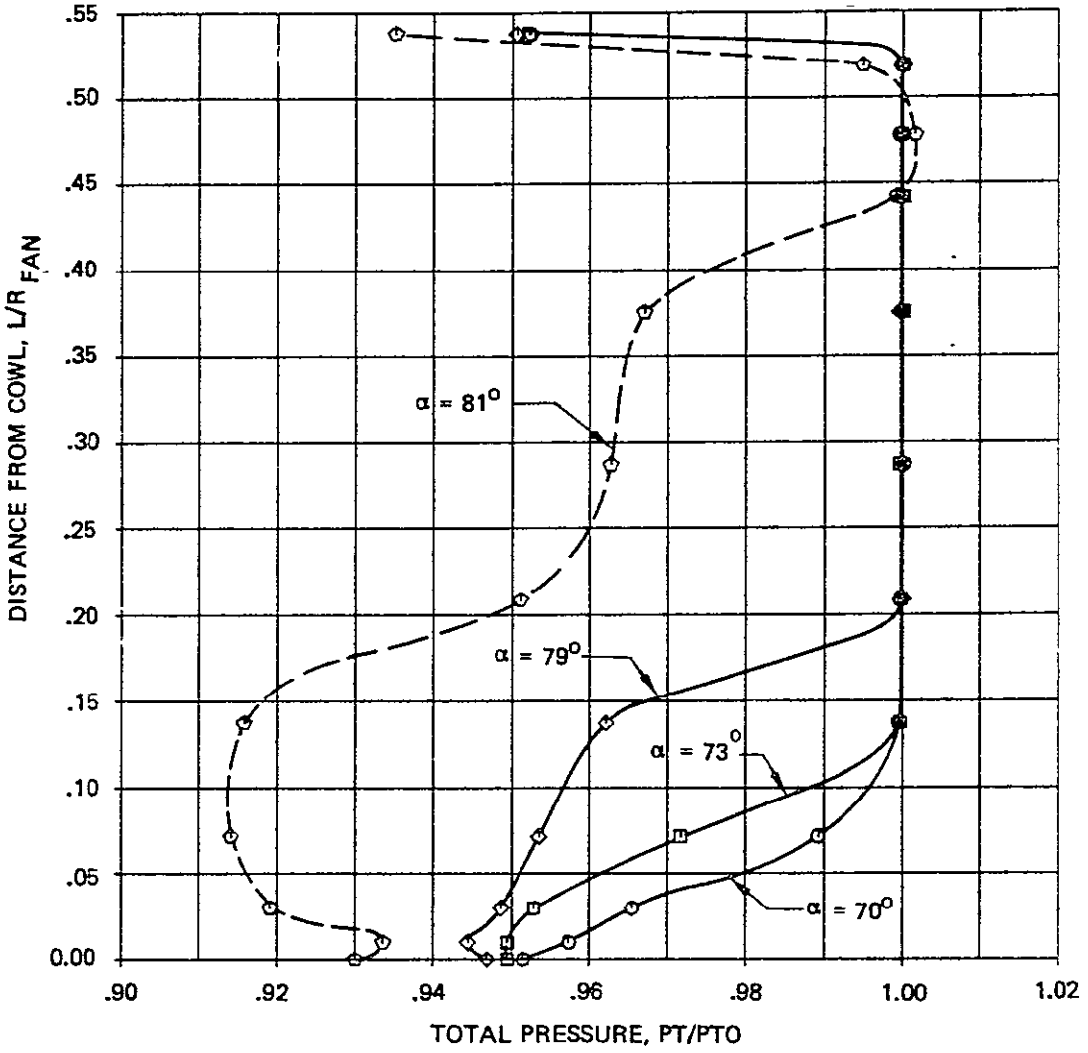

Figure 24. Fan Face Total Pressure Profiles, Windward Rake, V_o = 45 m/s, WKIA = 100 kg/sm²

ORIGINAL PAGE IS
OF POOR QUALITY

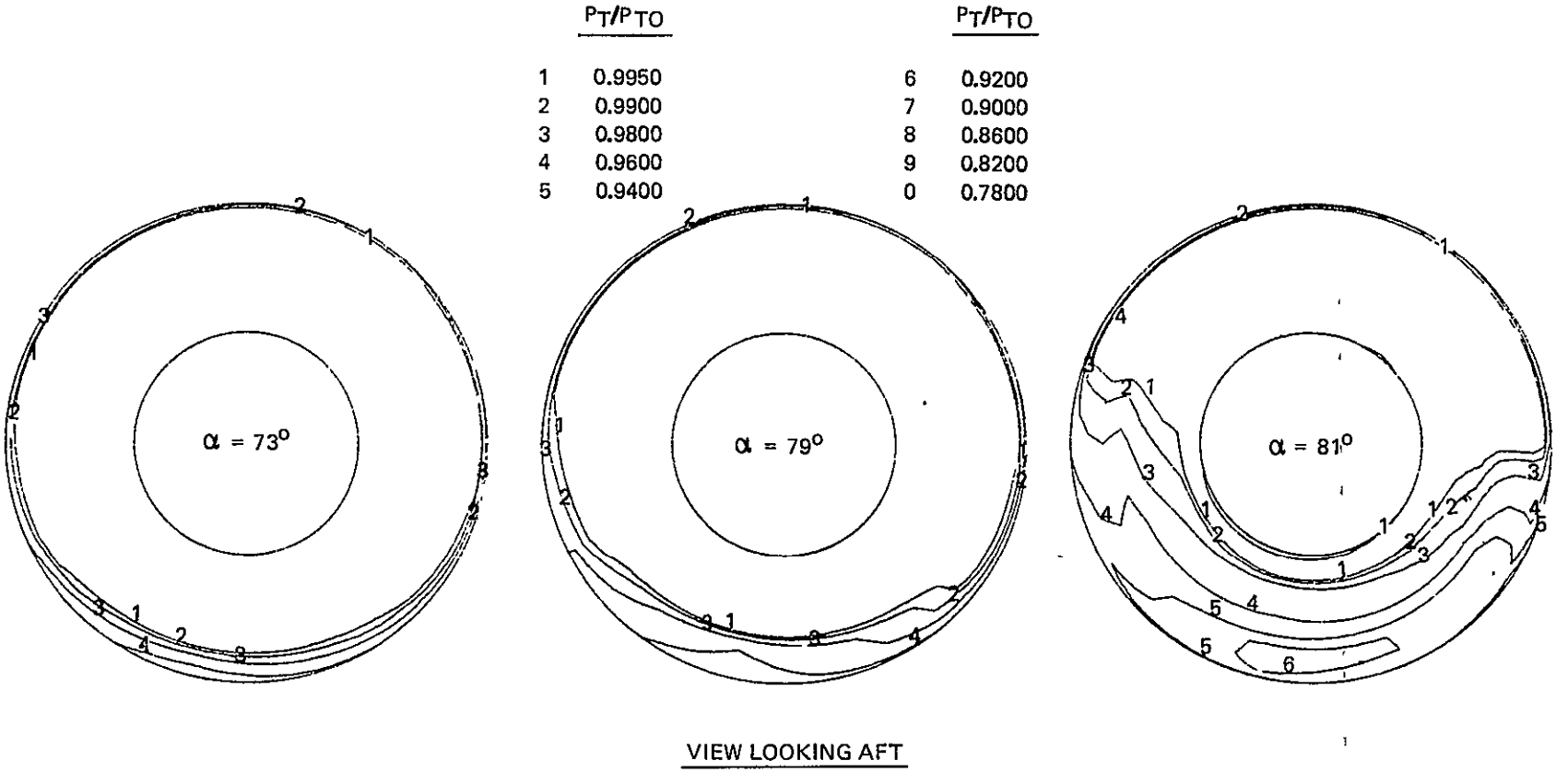

Figure 25. Fan Face Total Pressure Maps. V_o = 45 m/s, WKIA = 100 kg/sm^2

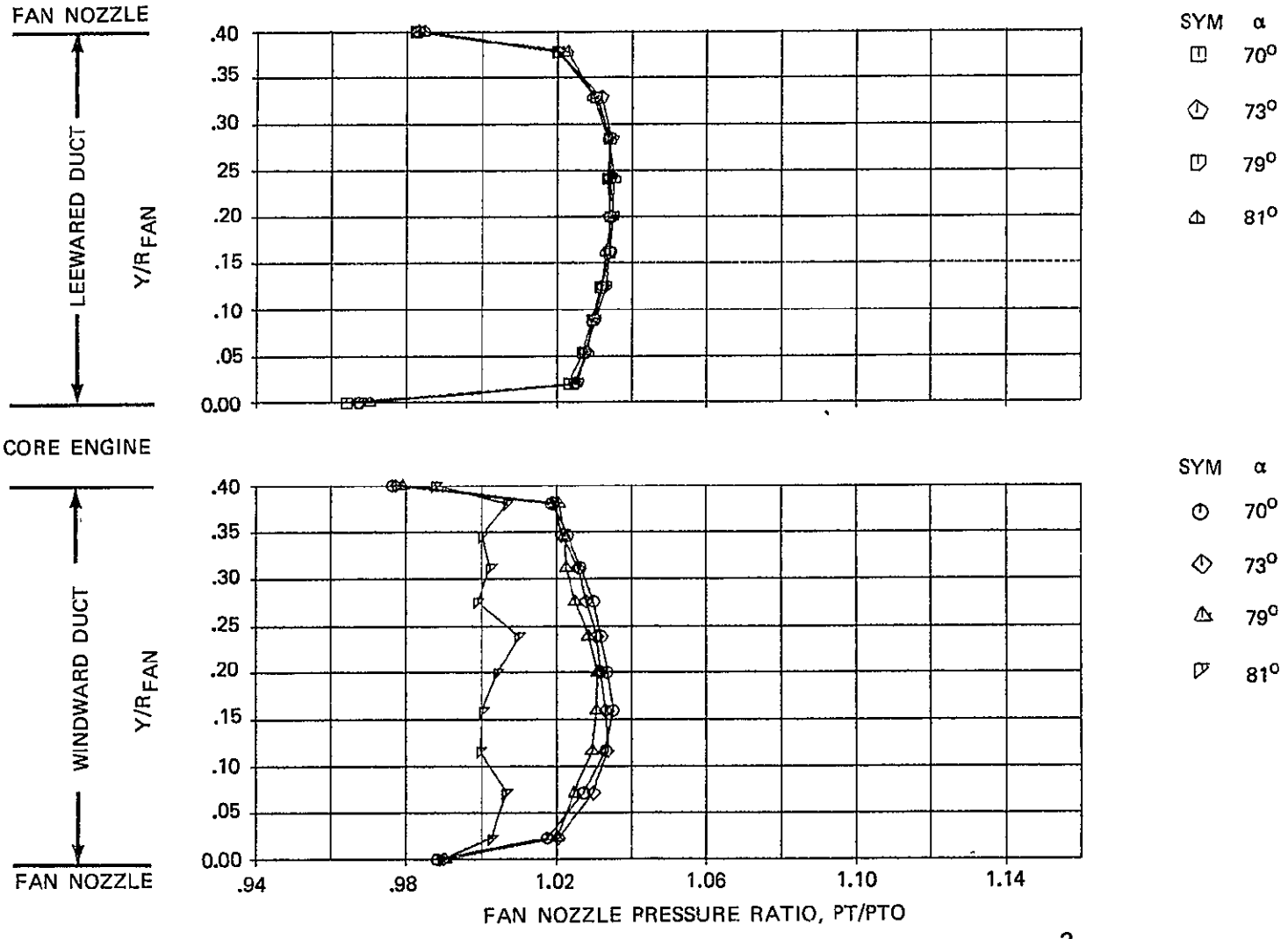

Figure 26. Fan Nozzle Total Pressure Profiles, V_o = 45 m/s, WKIA = 100 kg/sm^2

ORIGINAL PAGE IS
OF POOR QUALITY

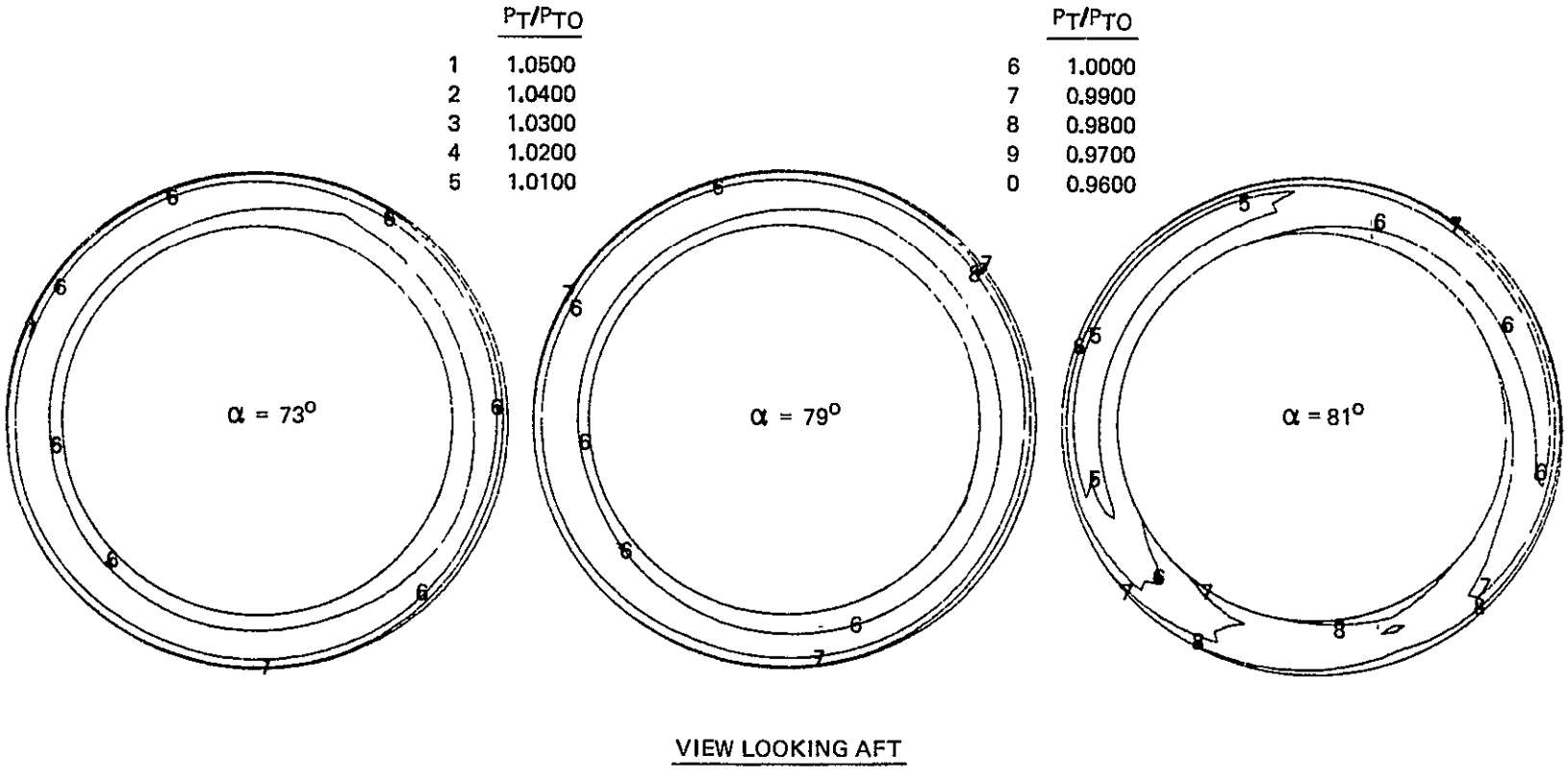

Figure 27· Compressor Face Rake Total Pressure Maps V_o = 45 m/s, WK1A = 100 kg/sm^2

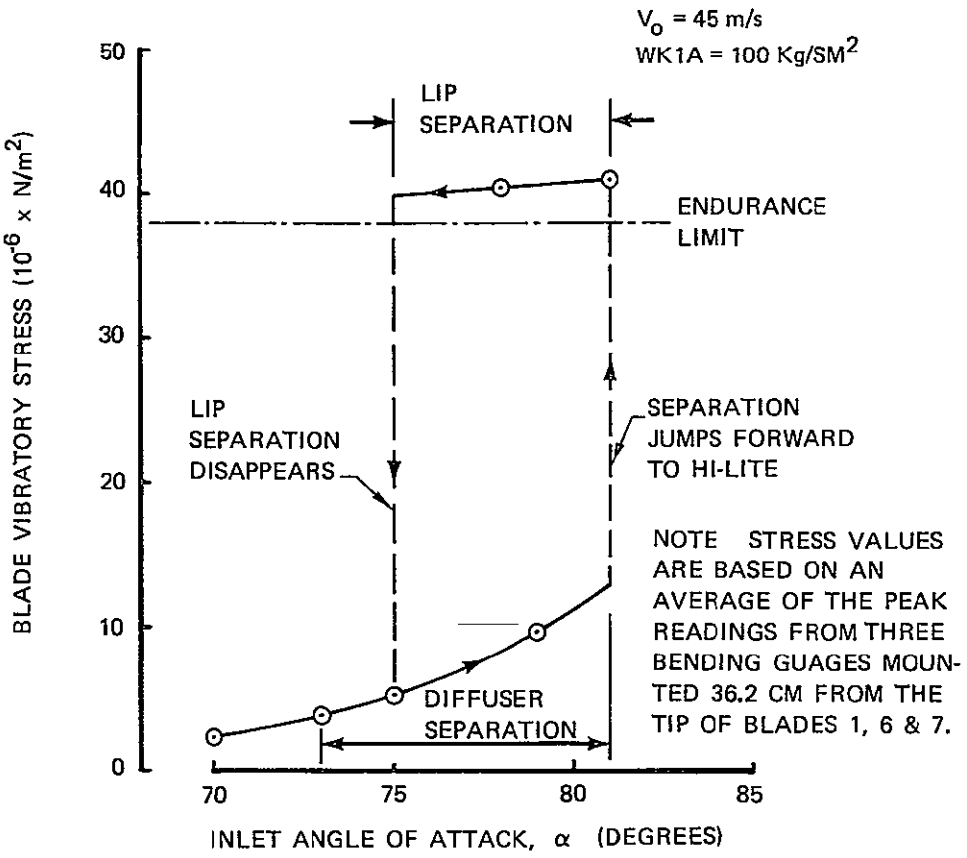

Figure 28. Fan Blade Vibratory Stress During Lip Separation

ORIGINAL PAGE IS
OF POOR QUALITY

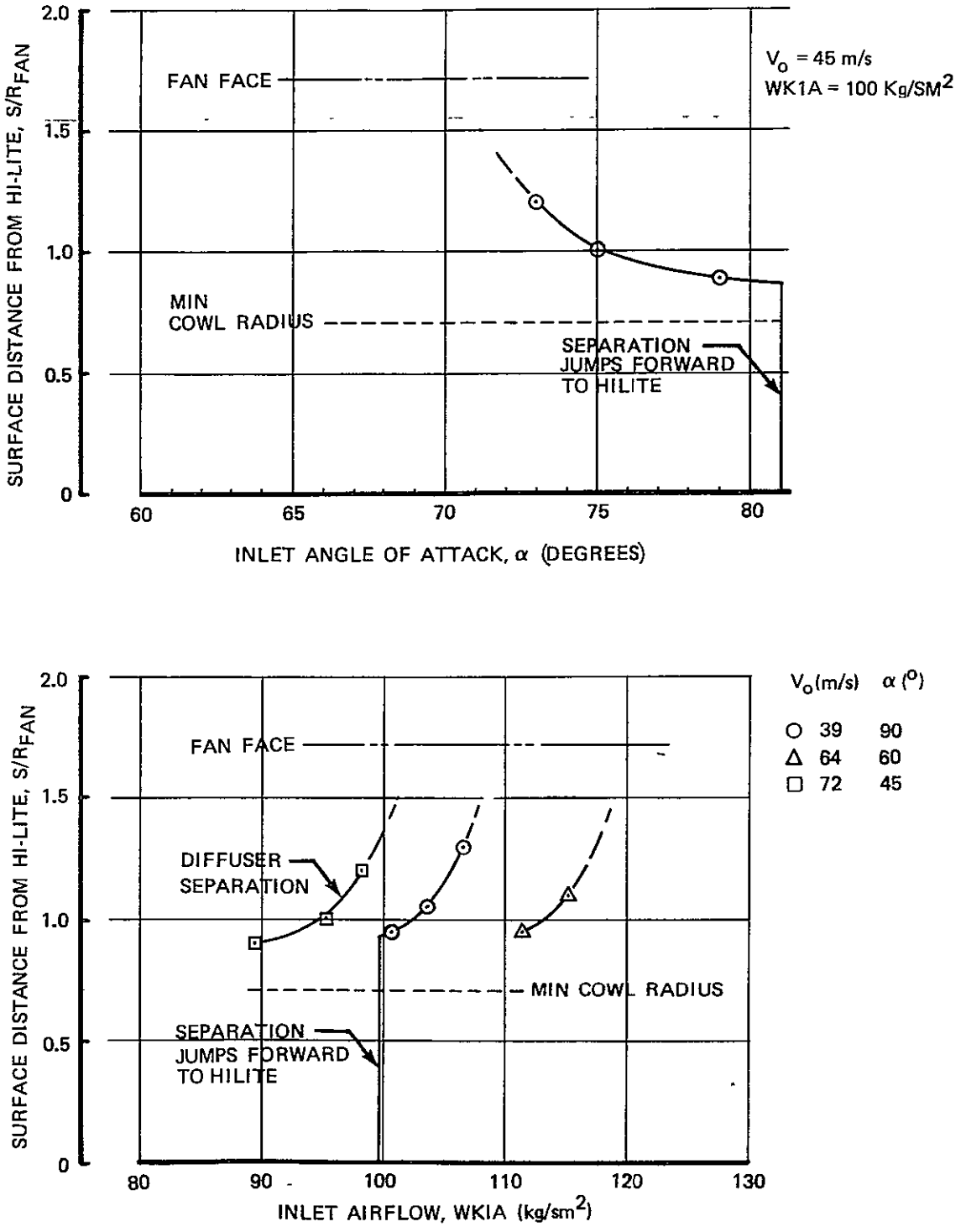

Figure 29. Windward Plane Inlet Station for Leading Edge of Separation

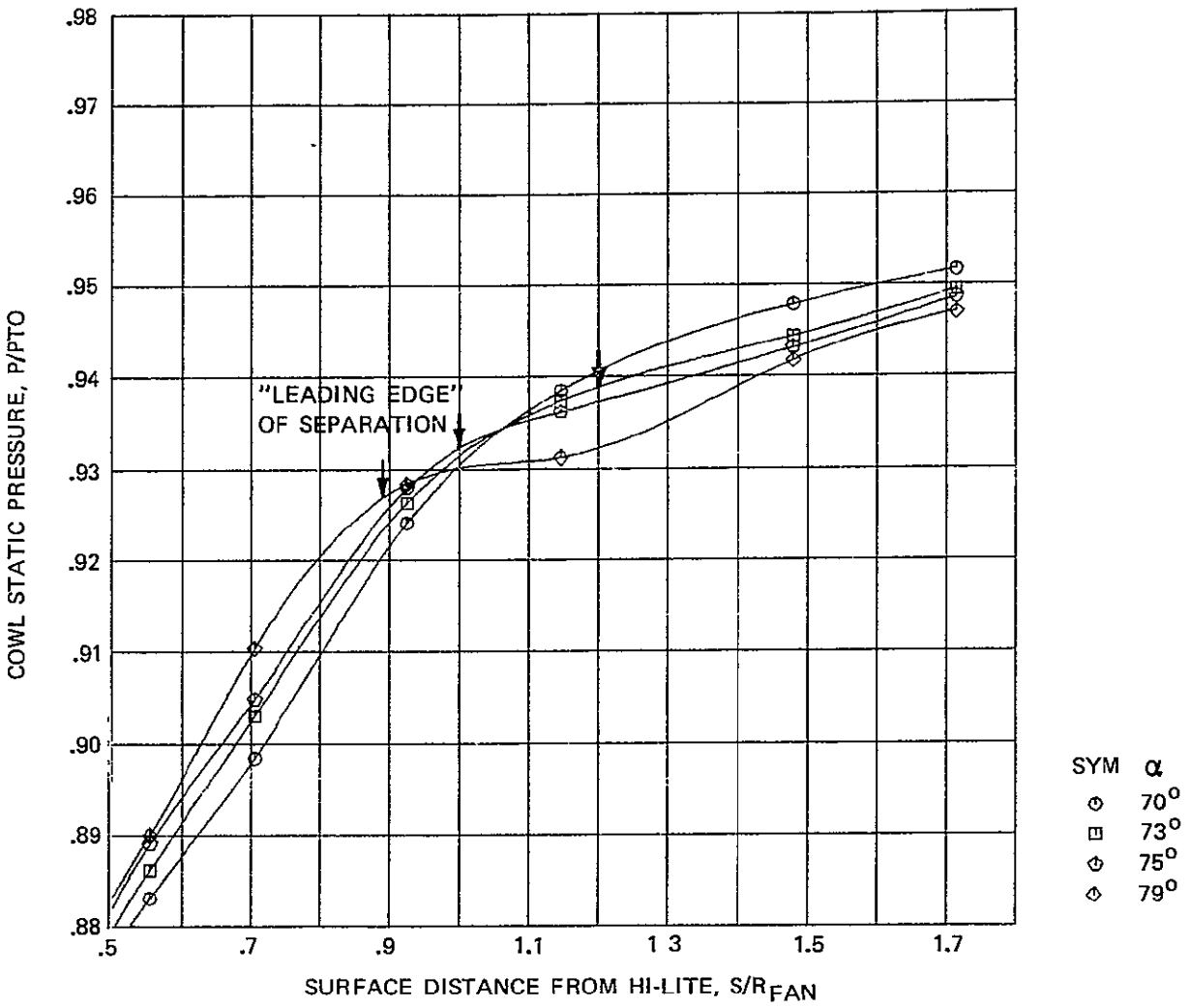

Figure 30. Static Pressure Profiles with Diffuser Separation, V_o = 45 m/s, WKIA = 100 kg/sm^2

ORIGINAL PAGE IS
OF POOR QUALITY

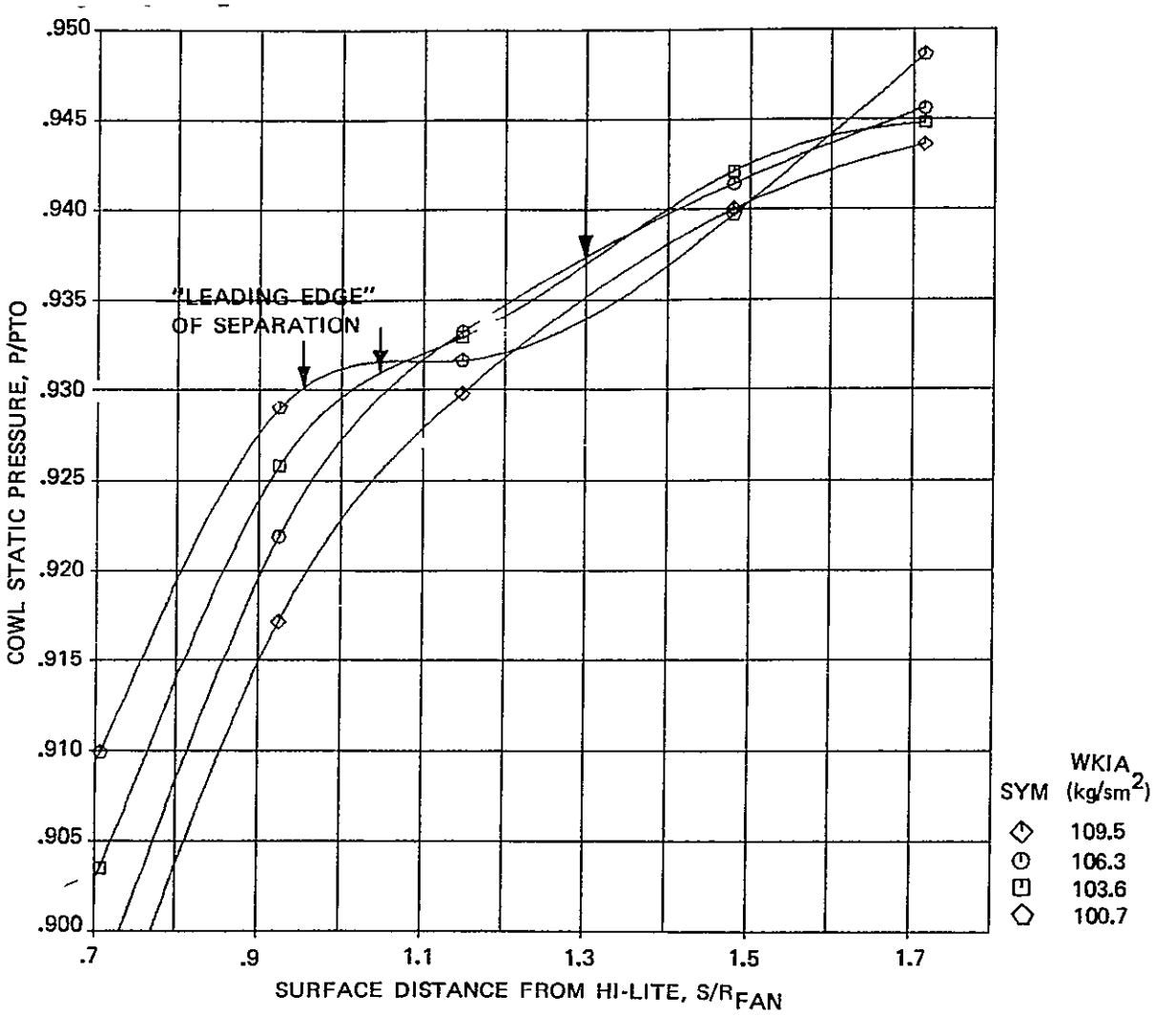

Figure 31. Static Pressure Profiles with Diffuser Separation V_o = 39 m/s, $\alpha = 90^o$

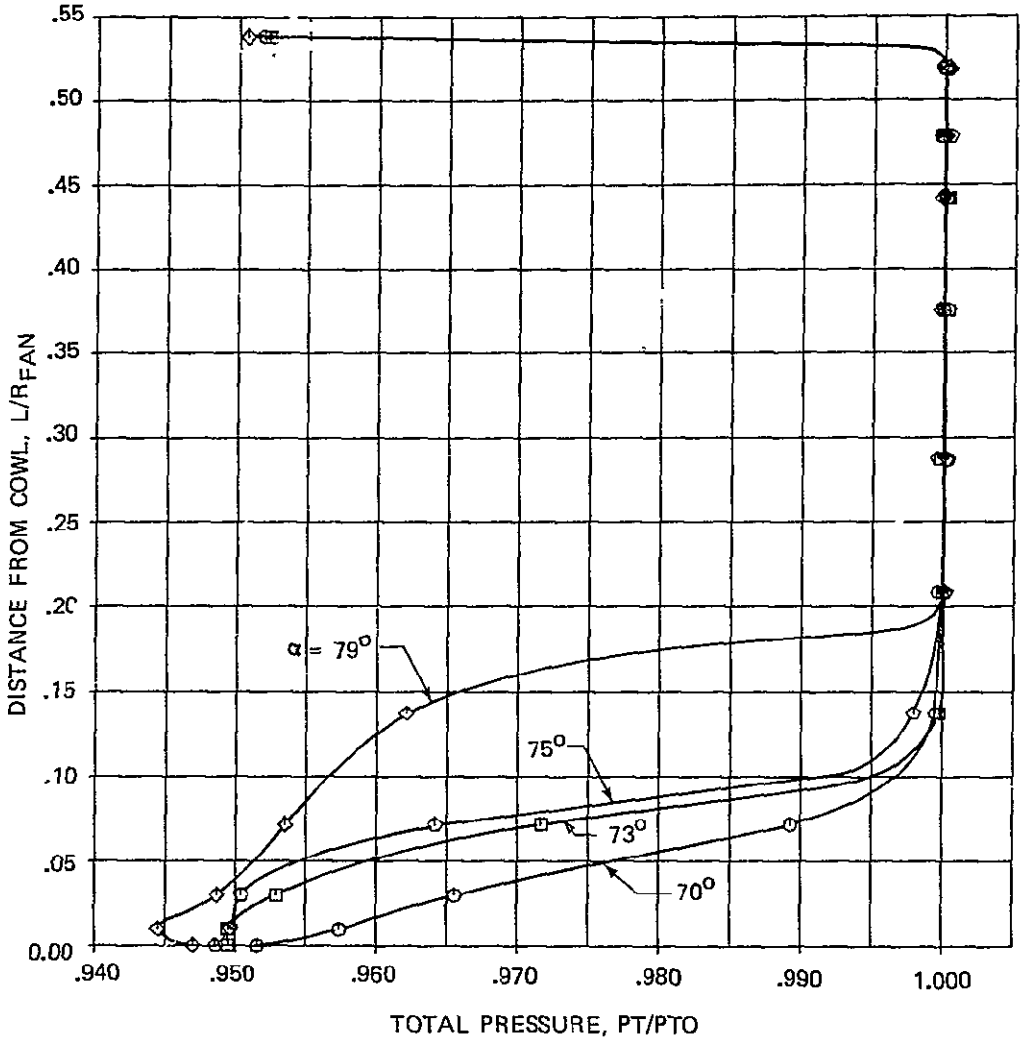

Figure 32. Fan Face Total Pressure Profiles with Diffuser Separation
V_o = 45 m/s, WKIA = 100 kg/sm^2

ORIGINAL PAGE IS
OF POOR QUALITY

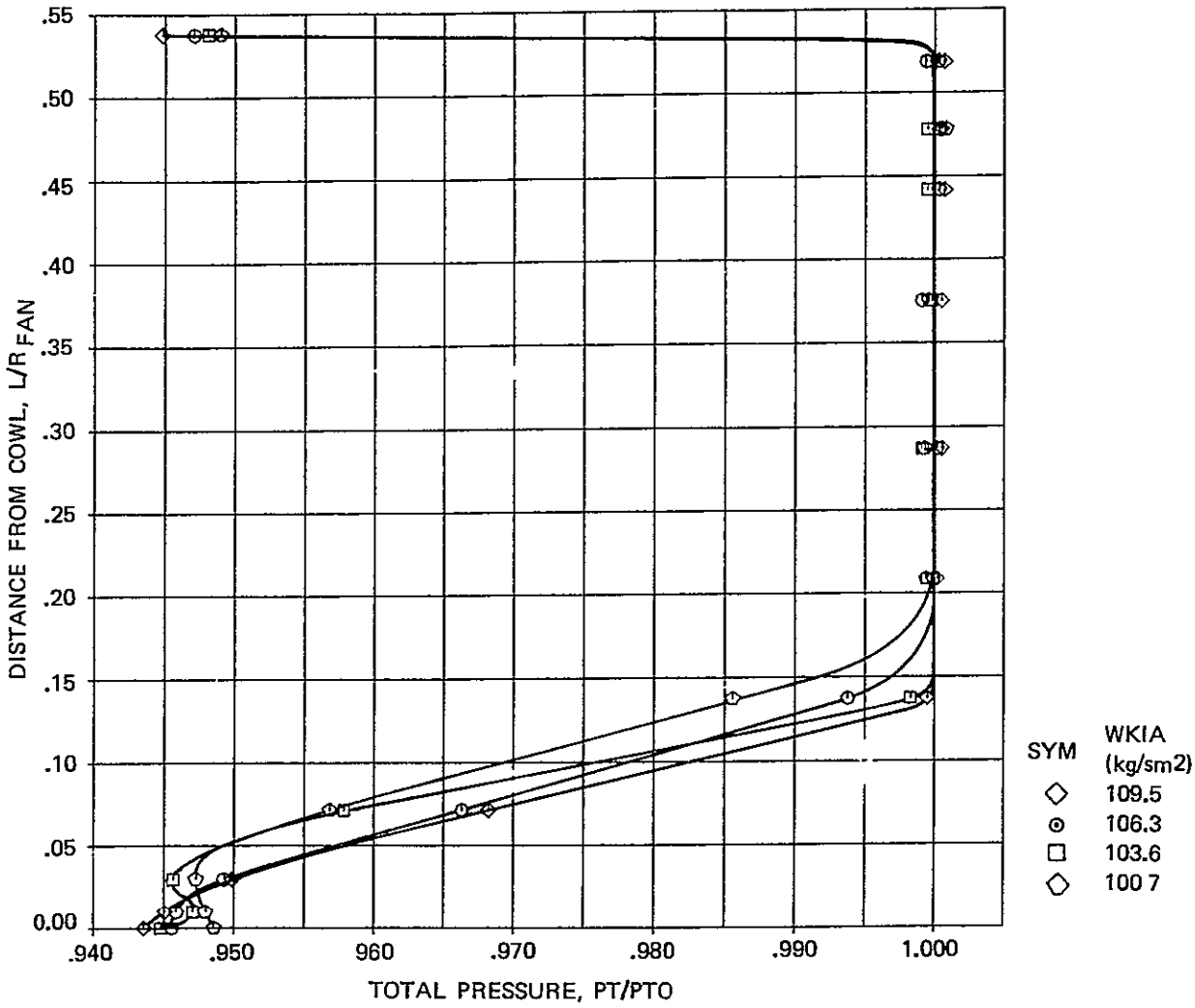

Figure 33. Fan Face Total Pressure Profiles with Diffuser Separation. V_o *= 39 m/s,* $\alpha = 90^o$

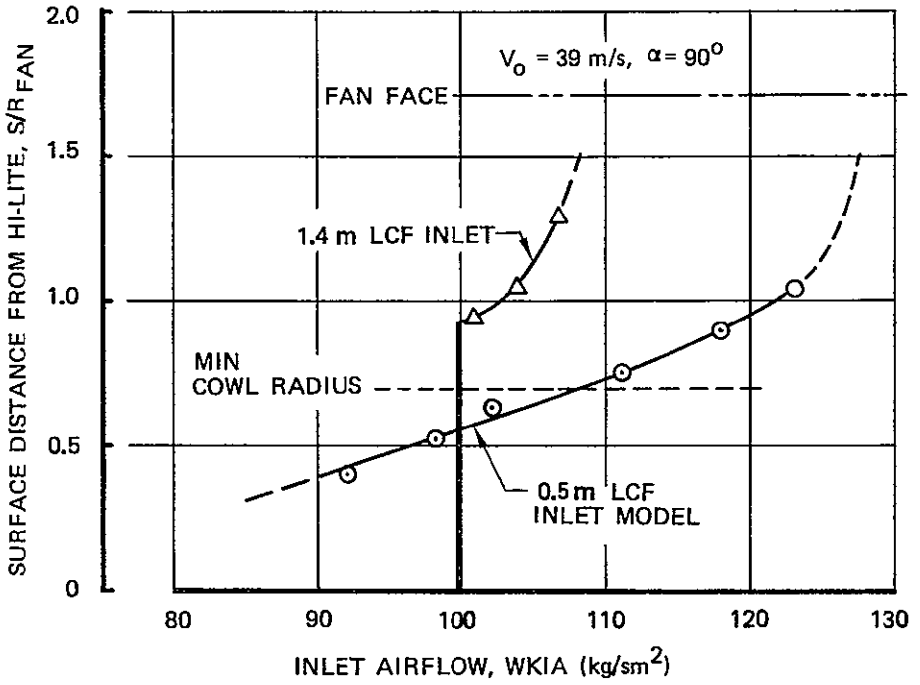

Figure 34. Diffuser Separation Characteristics in Small and Large Scale Inlet Models

ORIGINAL PAGE IS
OF POOR QUALITY

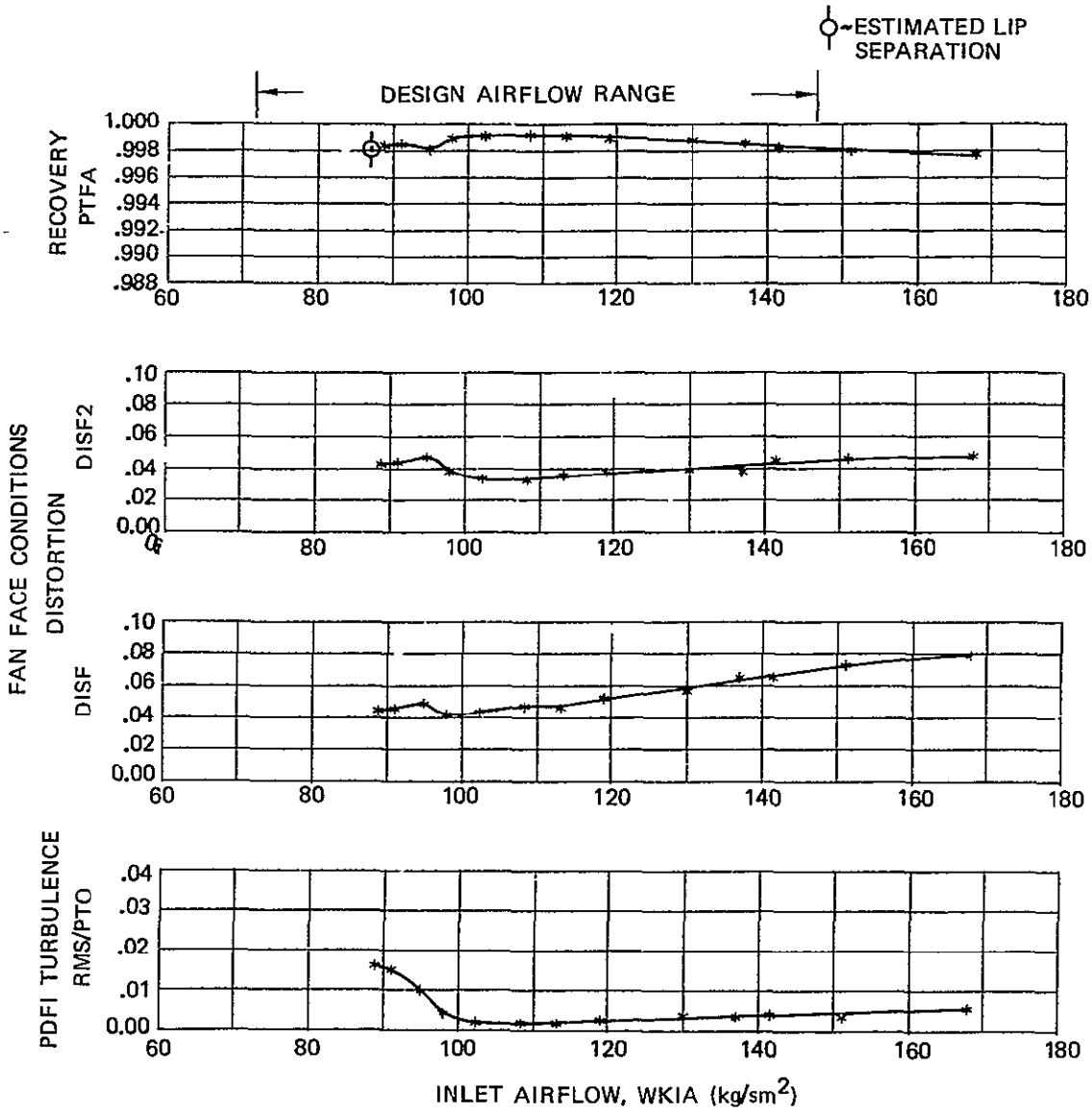

Figure 35. Inlet Performance Characteristics V_o = 72 m/s, α= 45°

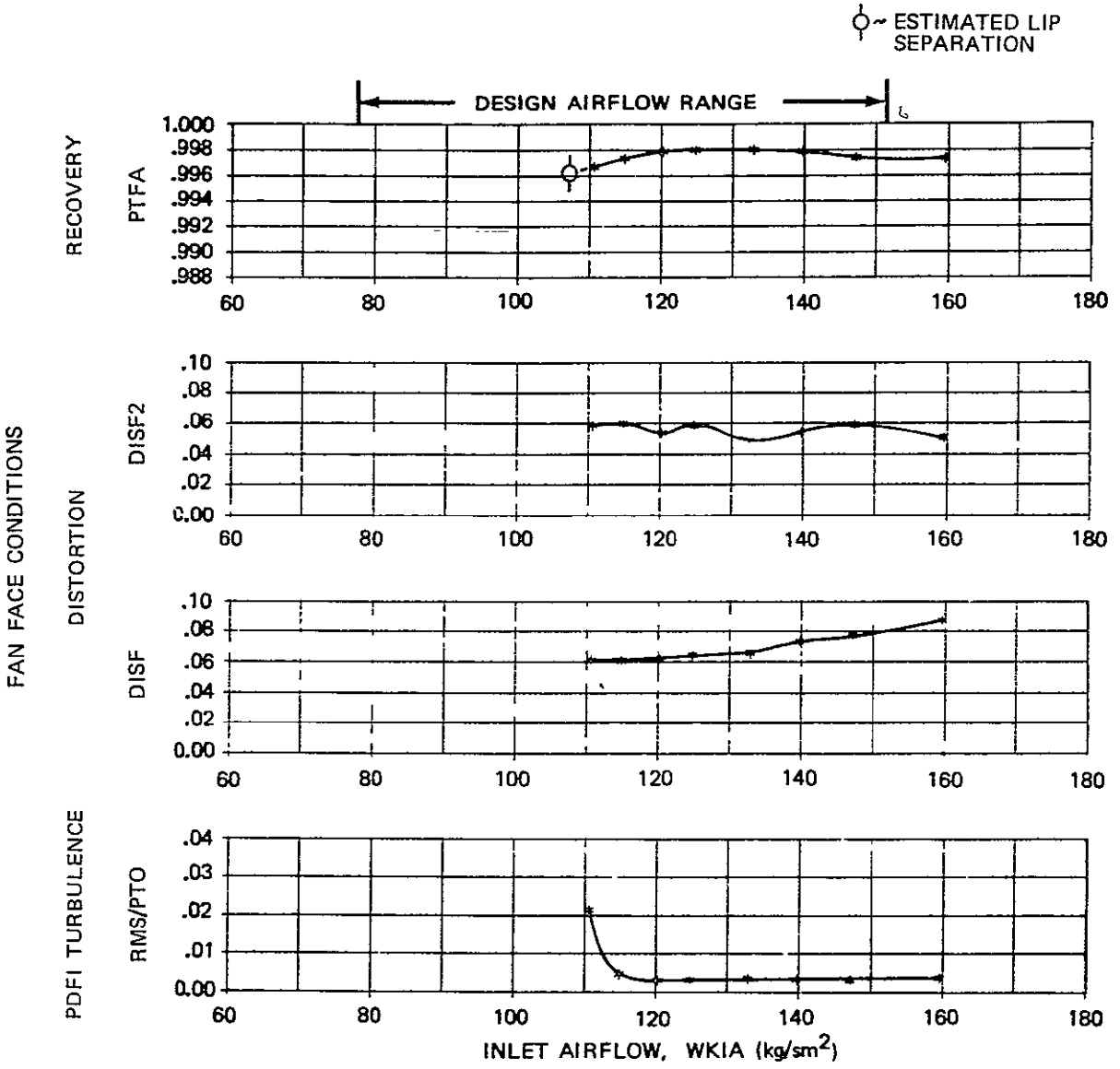

Figure 36. Inlet Performance Characteristics, V_o = 64 m/s, $\alpha = 60^o$

ORIGINAL PAGE IS
OF POOR QUALITY

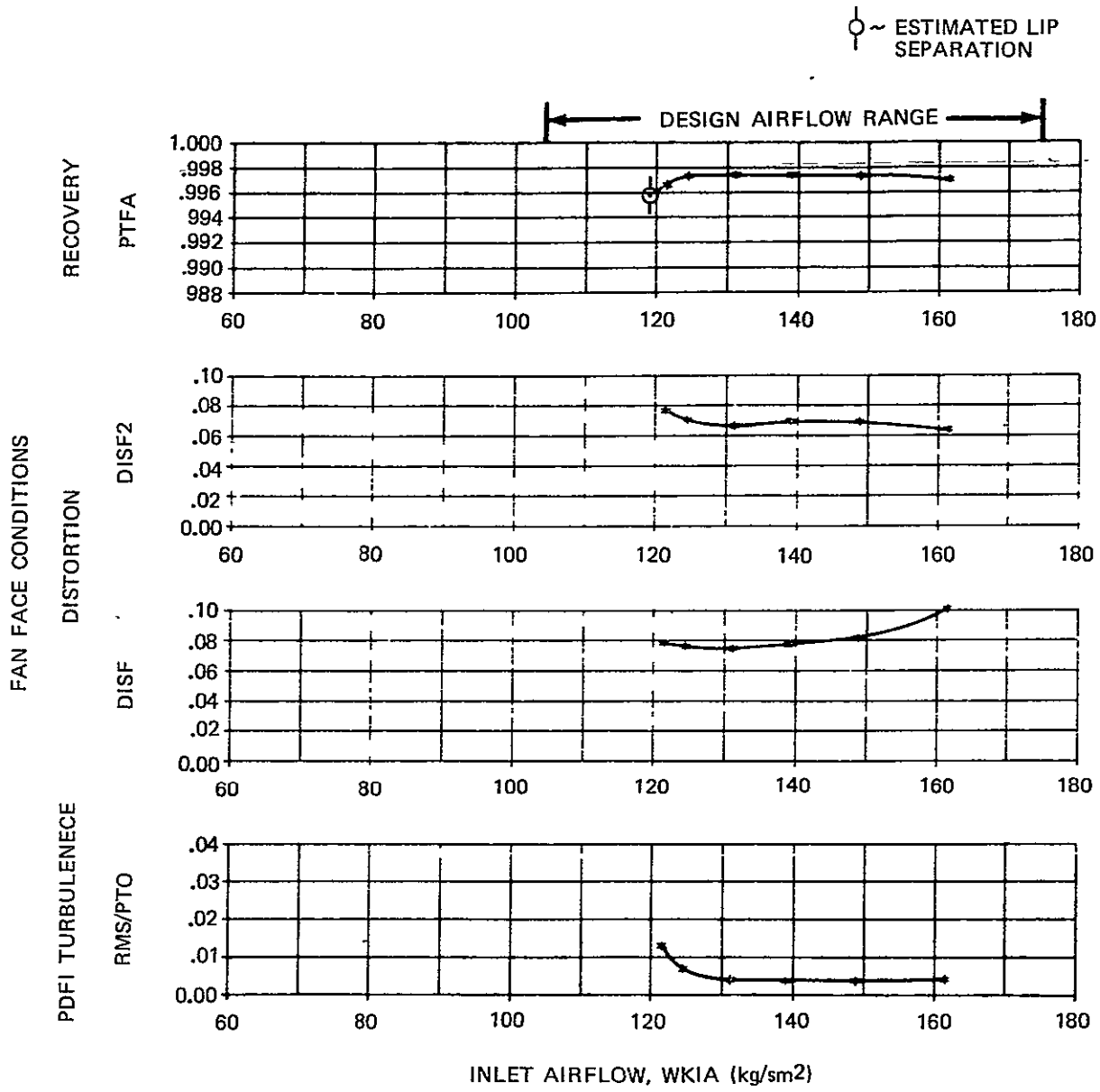

Figure 37. Inlet Performance Characteristics, V_o = 54 m/s, $\alpha = 75^o$

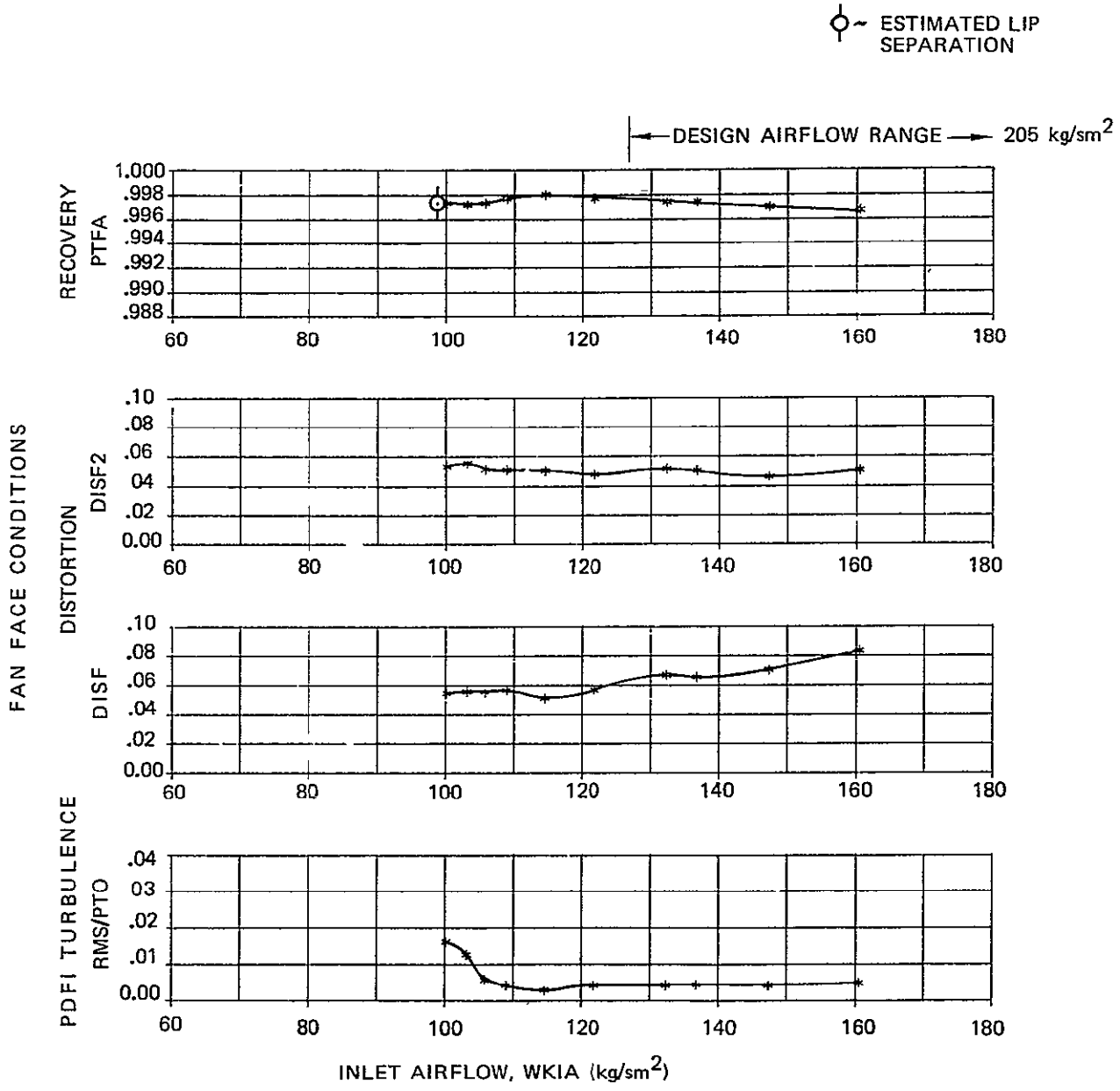

Figure 38. Inlet Performance Characteristics, V_o = 39 m/s, $\alpha = 90^o$

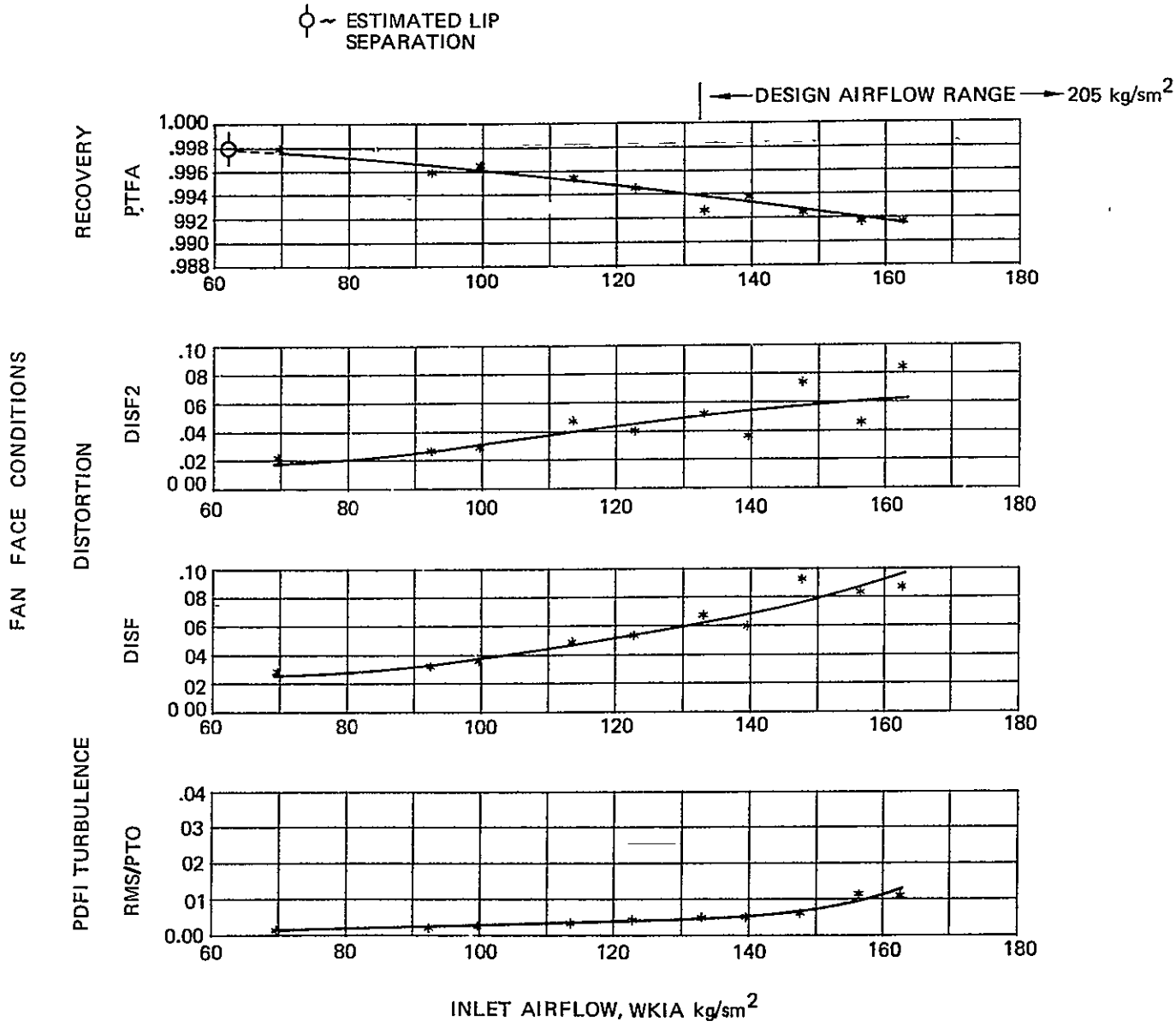

Figure 39. Inlet Performance Characteristics, V_O = 20 m/s, $\alpha = 120^o$

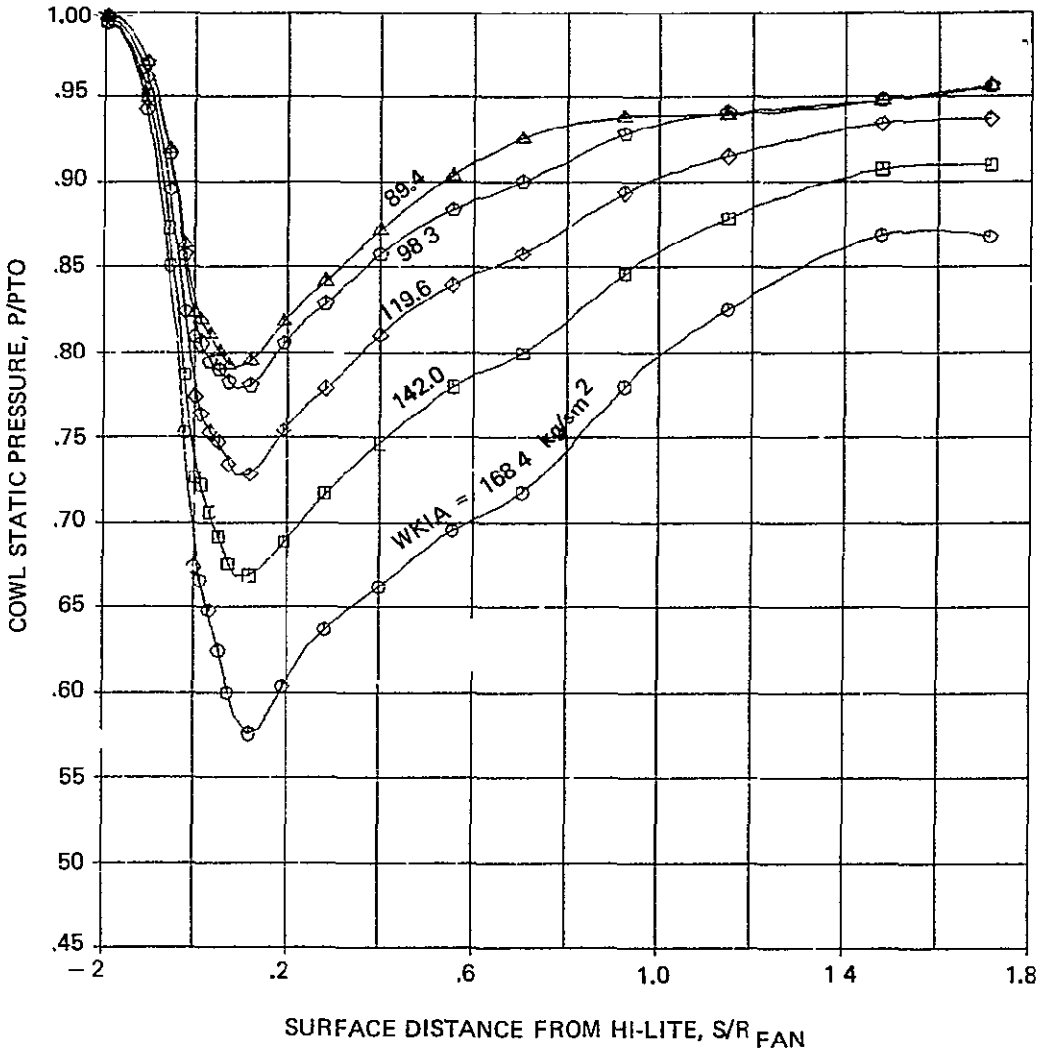

Figure 40. Inlet Static Pressure Profiles, Windward Side, V_o = 72 m/s, $\alpha = 45^o$

ORIGINAL PAGE IS
OF POOR QUALITY

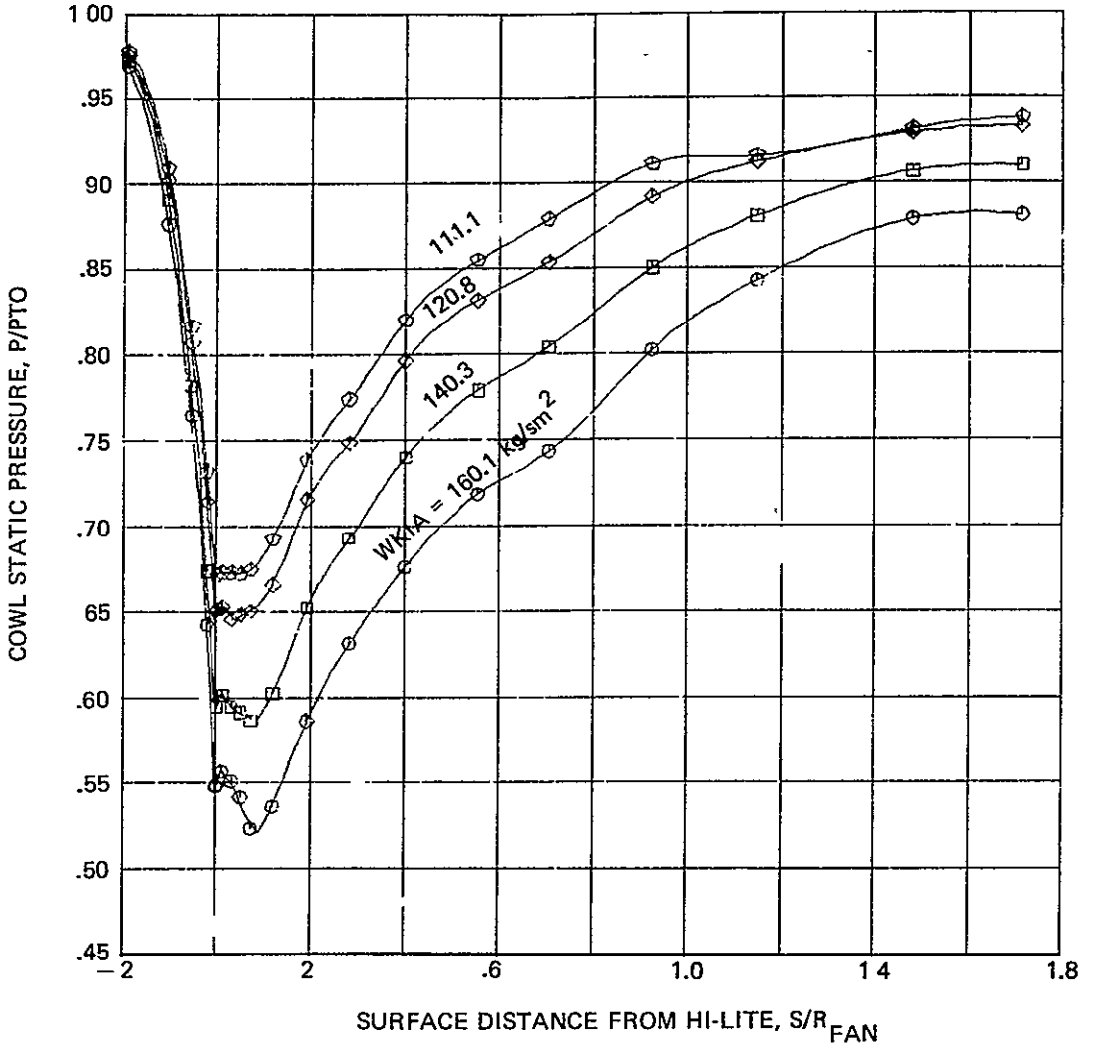

Figure 41. Inlet Static Pressure Profiles, Windward Side, V_o = 64 m/s, $\alpha = 60^o$

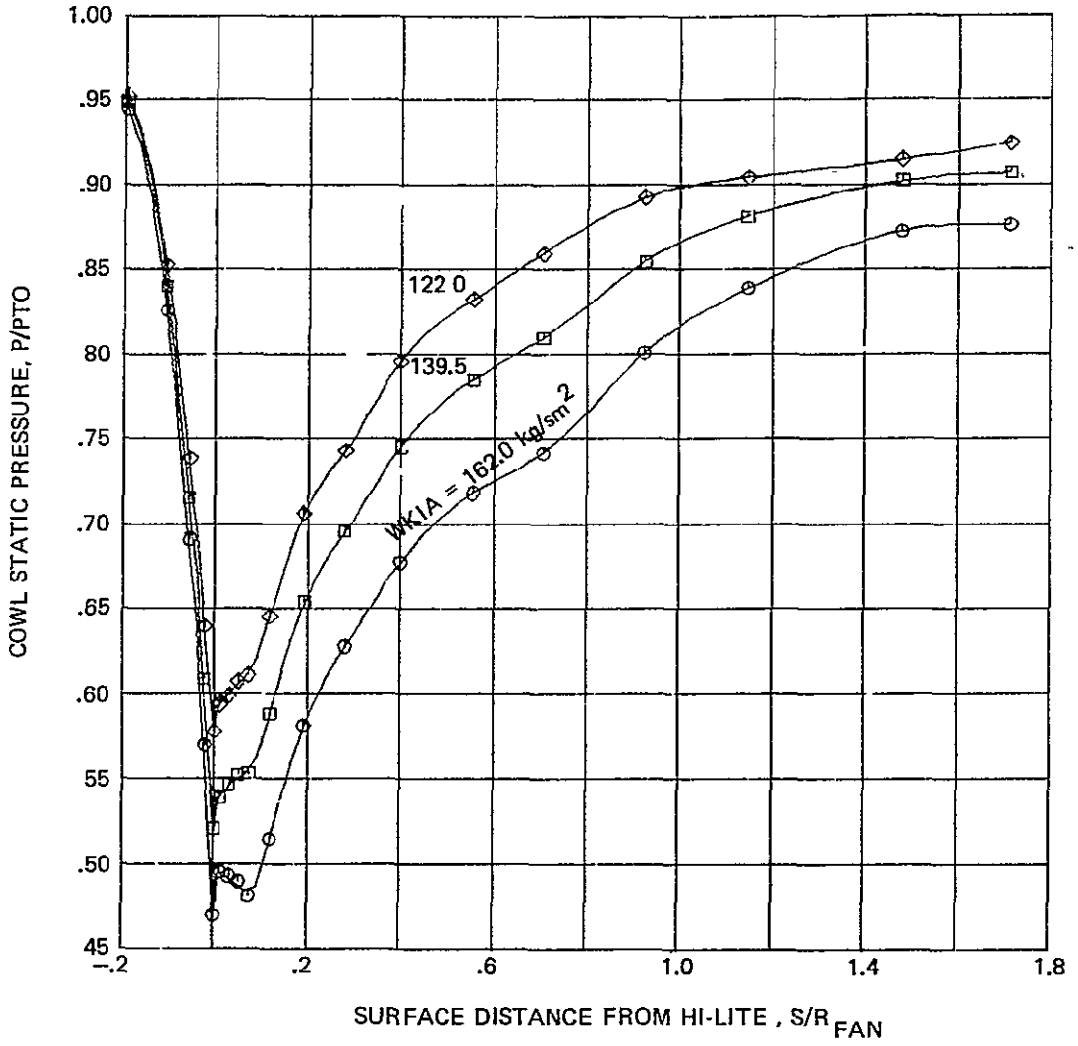

Figure 42. Inlet Static Pressure Profiles, Windward Side, V_o = 54 m/s, $\alpha = 75^o$

ORIGINAL PAGE IS
OF POOR QUALITY

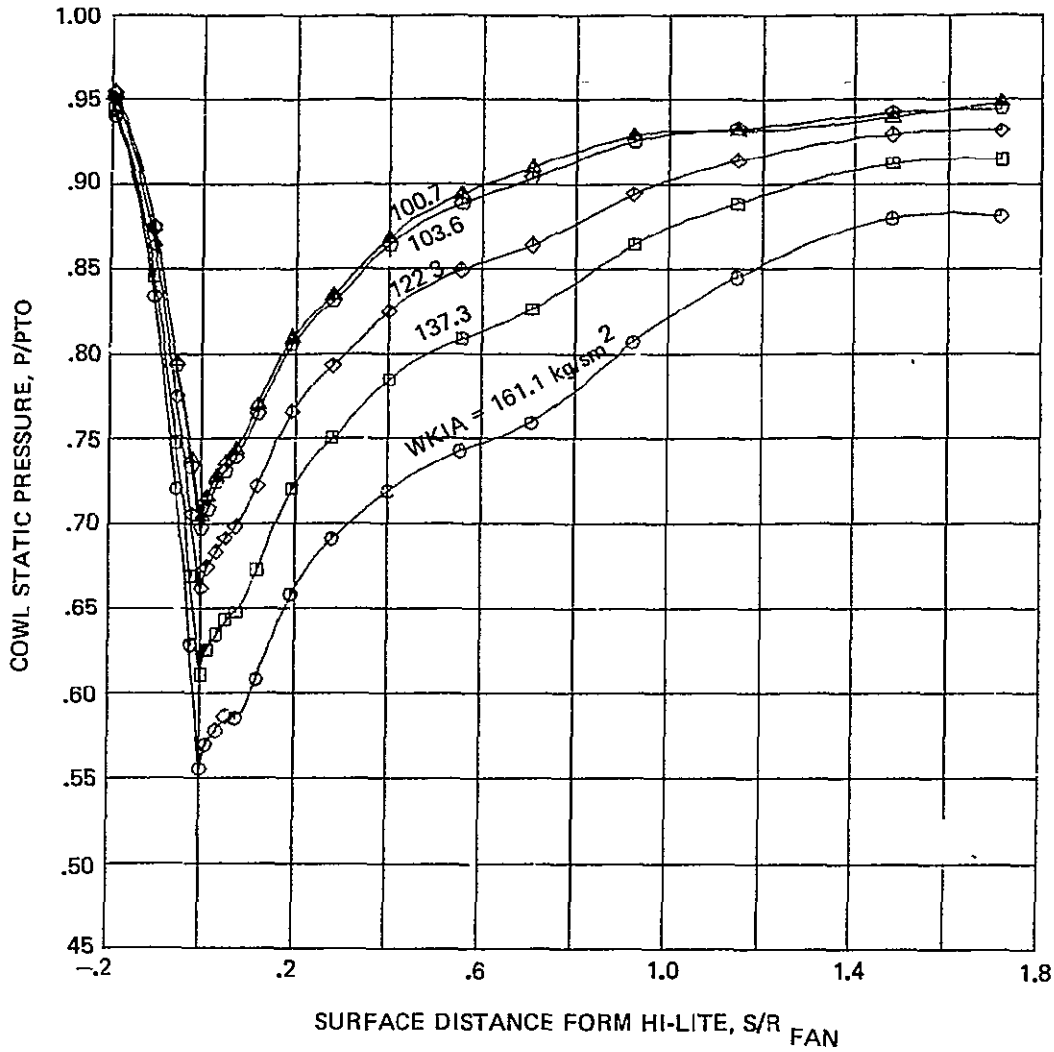

Figure 43. Inlet Static Pressure Profiles, Windward Side, V_o = 39 m/s, $\alpha = 90^o$

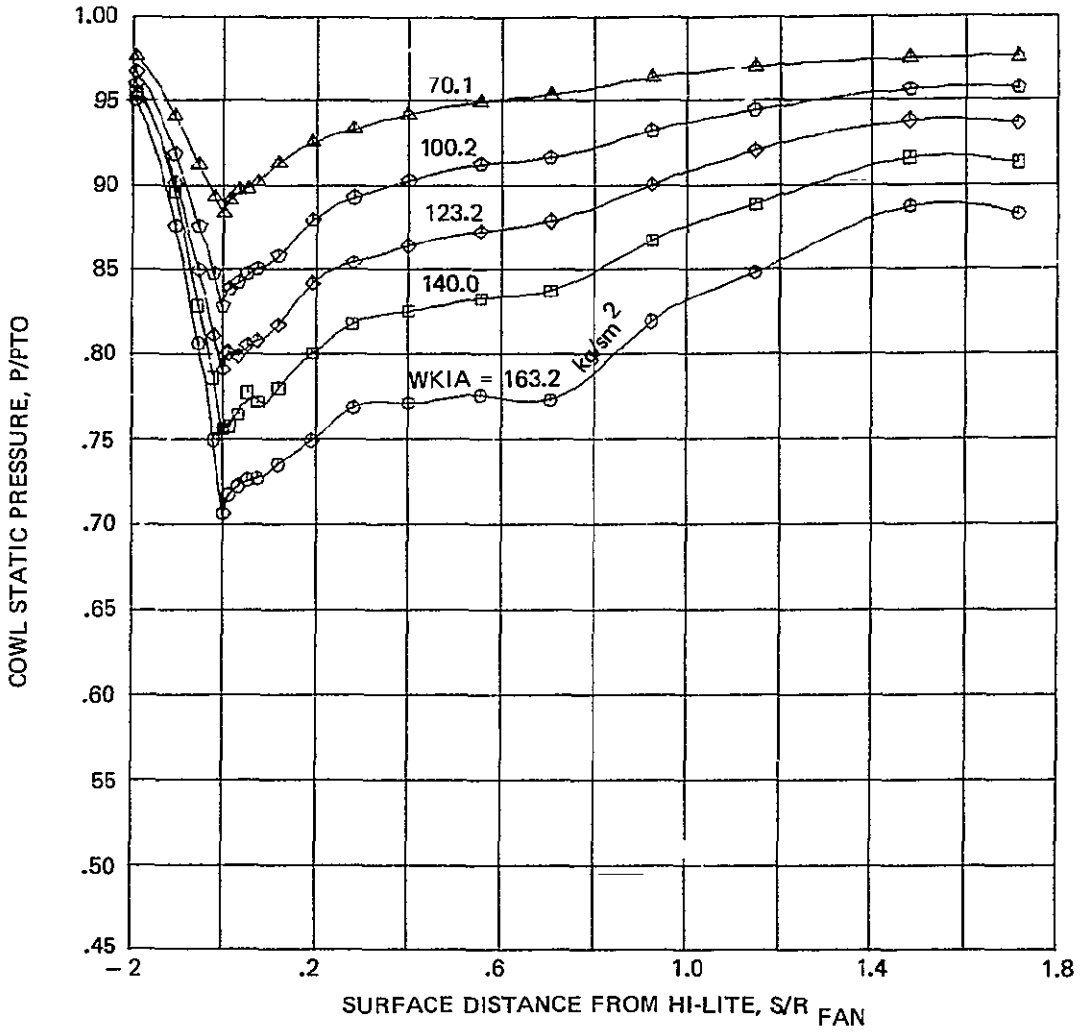

Figure 44. Inlet Static Pressure Profiles. Windward Side, V_o = 20 m/s, α= 120°

ORIGINAL PAGE IS
OF POOR QUALITY

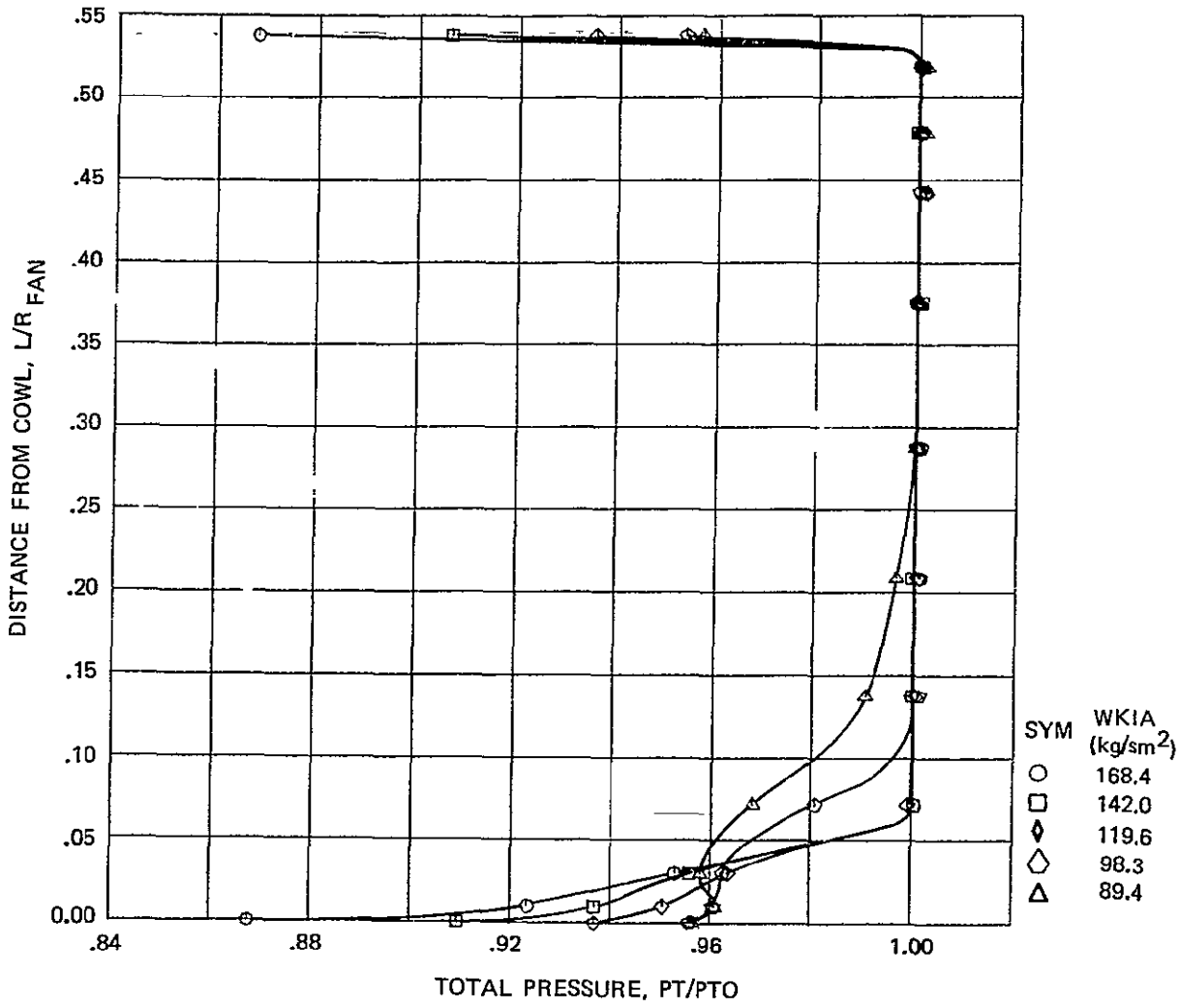

Figure 45. Fan Face Total Pressure Profiles, Windward Side Rake, V_0 = 72 m/s, α= 45°

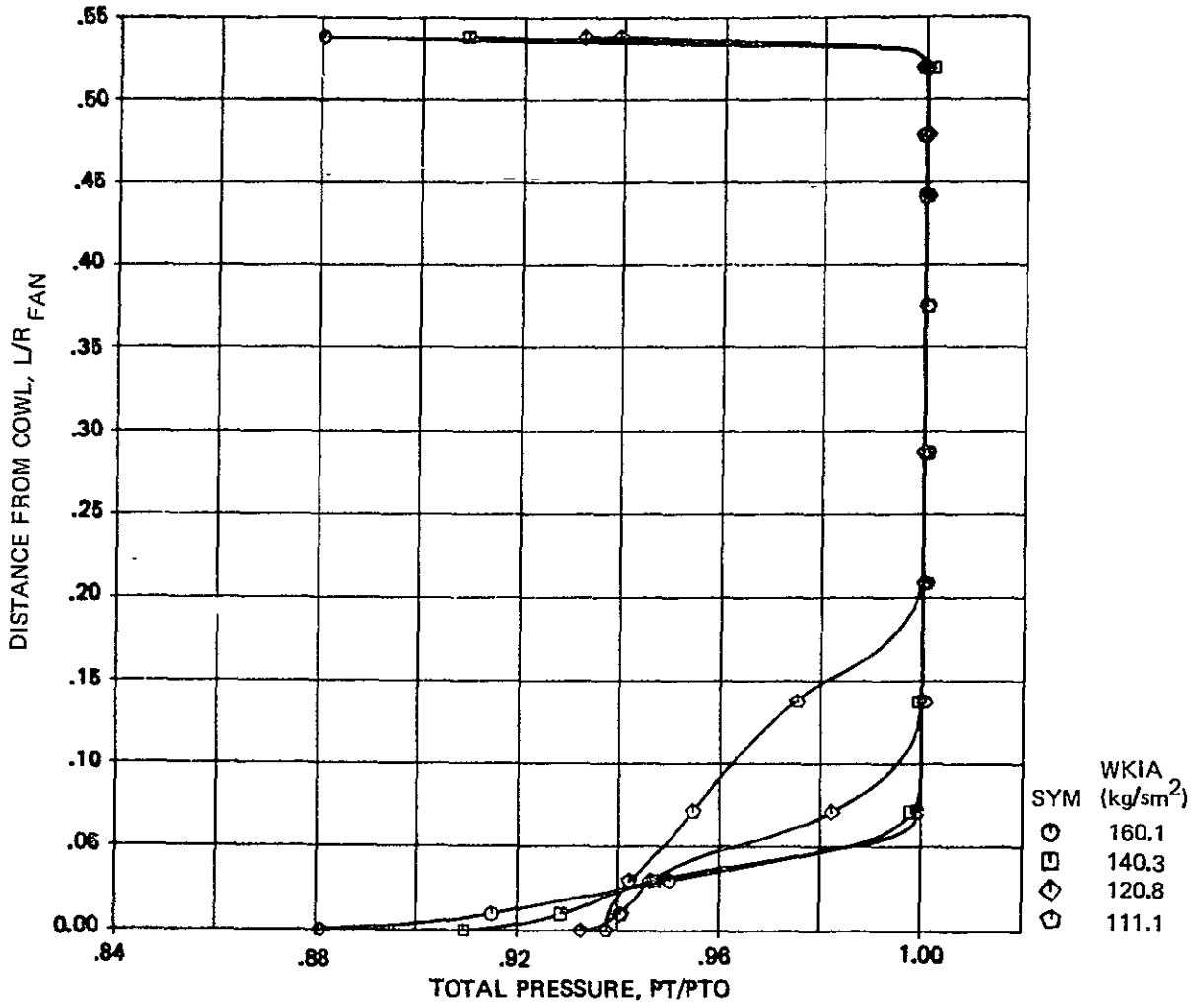

ORIGINAL PAGE IS
OF POOR QUALITY

Figure 46. Fan Face Total Pressure Profiles, Windward Rake, V_o = 64 m/s, $\alpha = 60^o$

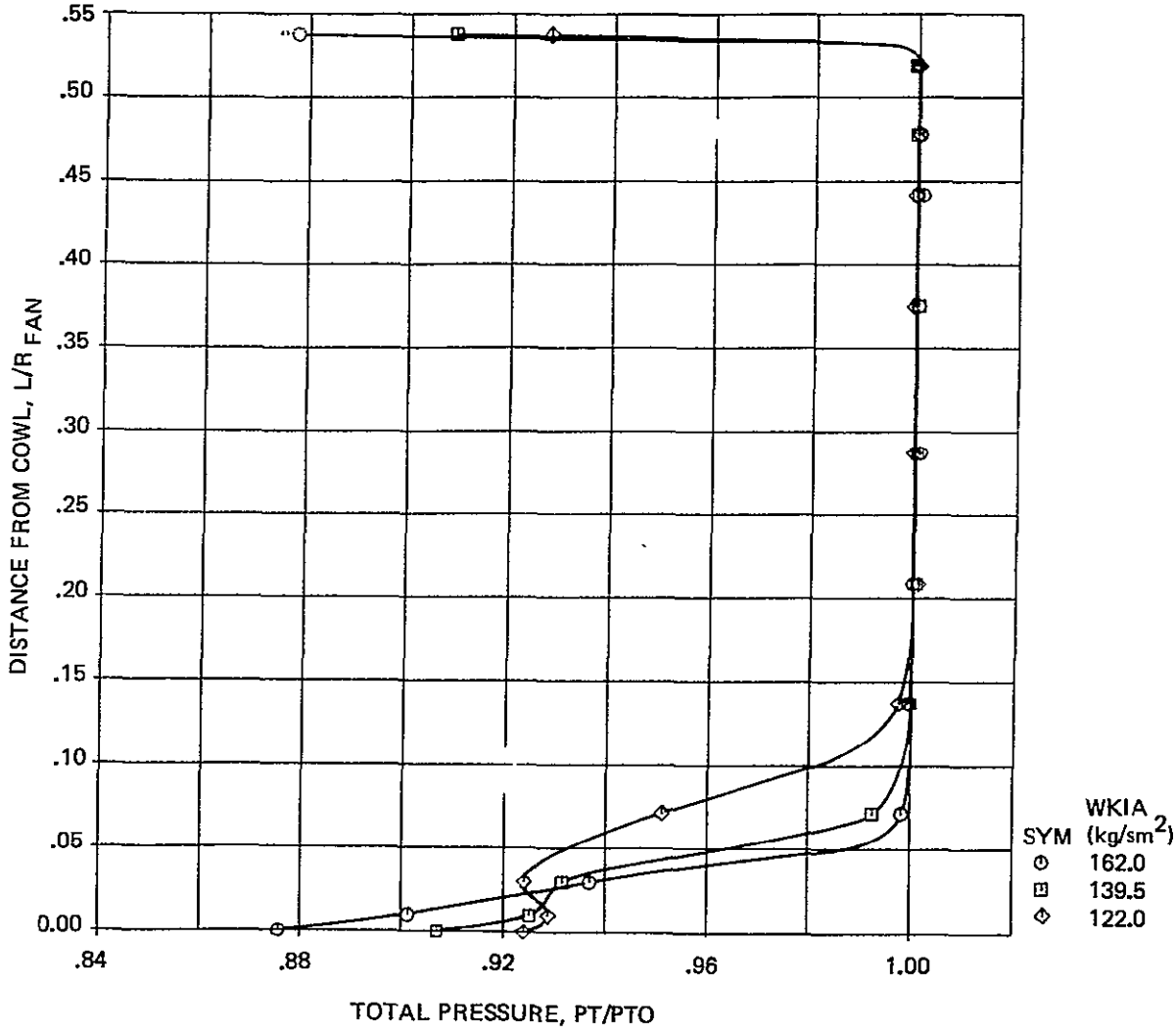

Figure 47. Fan Face Total Pressure Profiles, Windward Rake, V_o = 54 m/s, $\alpha = 75^o$

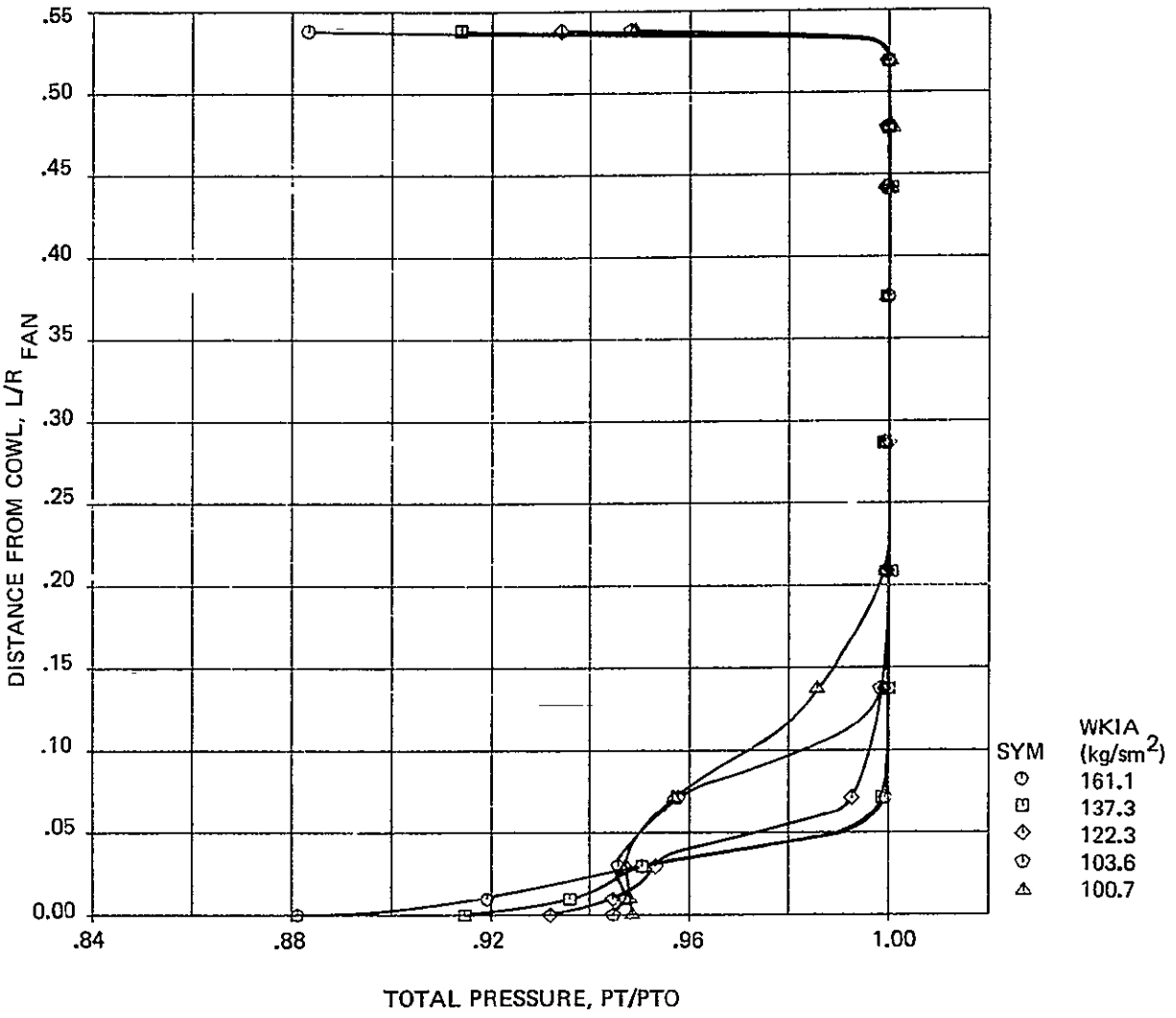

Figure 48. Fan Face Total Pressure Profiles, Windward Rake, V_o = 39 m/s, $\alpha = 90^o$

ORIGINAL PAGE IS
OF POOR QUALITY

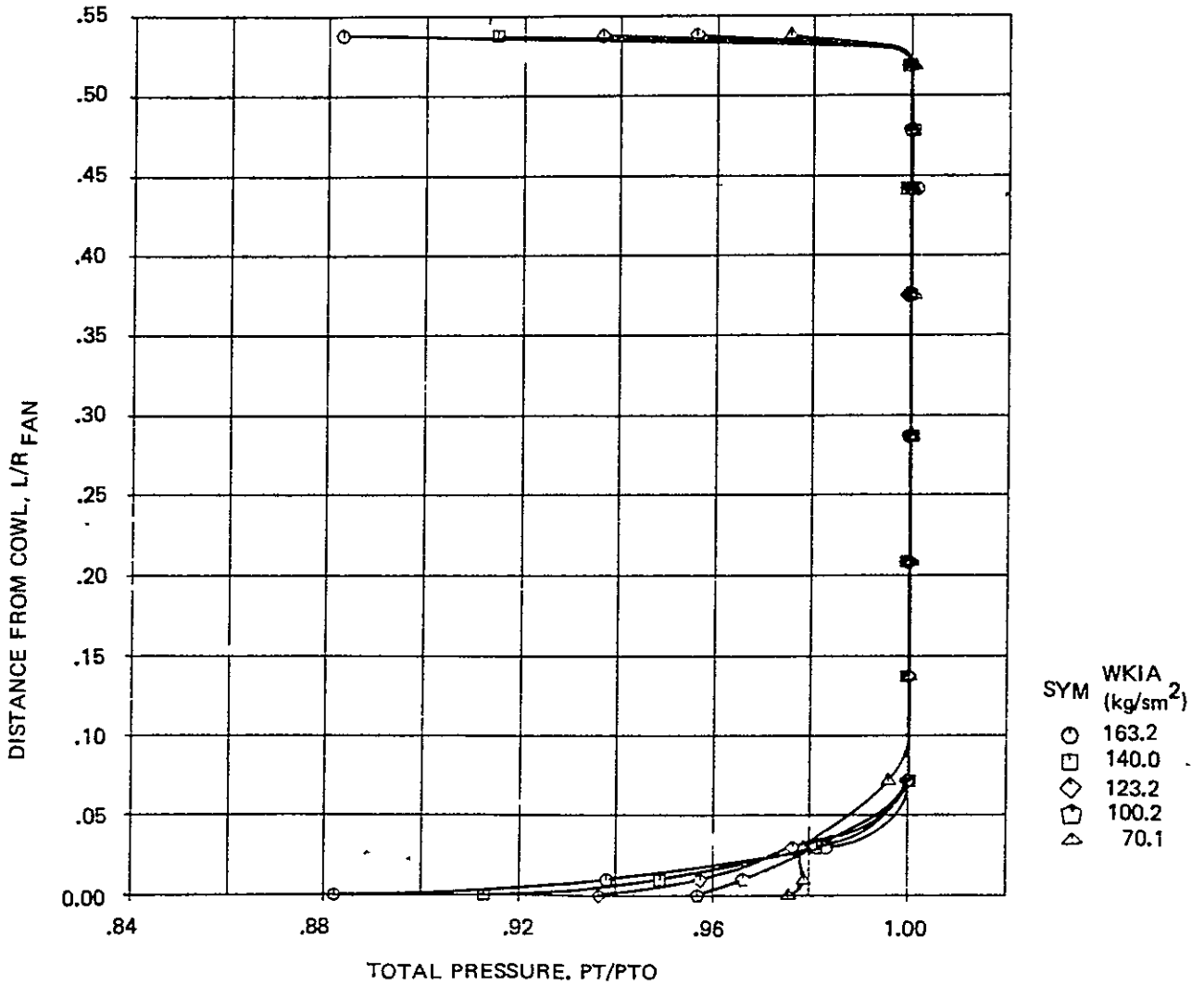

Figure 49. Fan Face Total Pressure Profiles, Windward Rake
V_o = 20 m/s, $\alpha = 120^o$

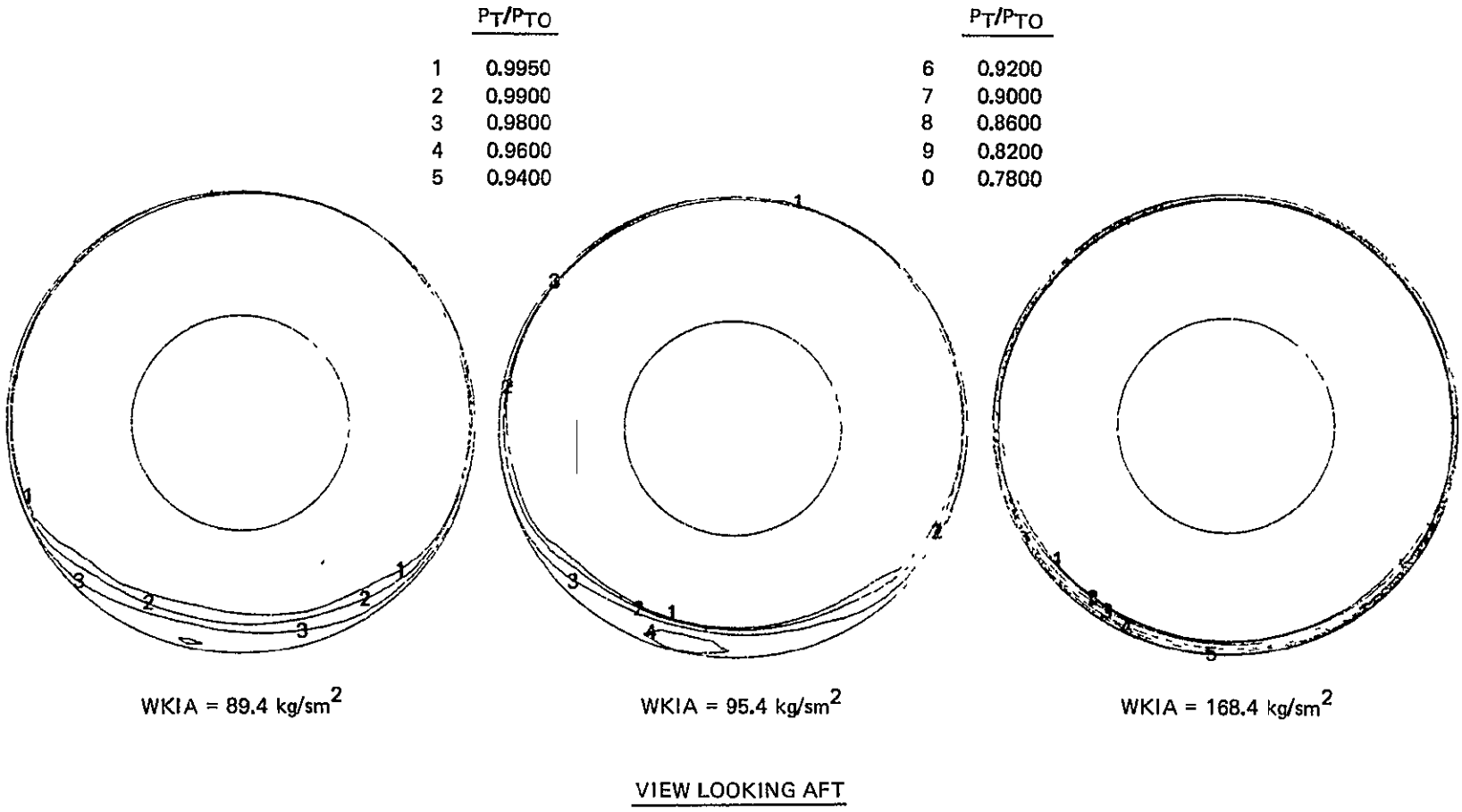

Figure 50. Fan Face Total Pressure Maps. V_O *= 72 m/s,* α *= 45°*

Figure 51. Fan Face Total Pressure Maps. V_o = 64 m/s, $\alpha = 60^o$

ORIGINAL PAGE IS
OF POOR QUALITY

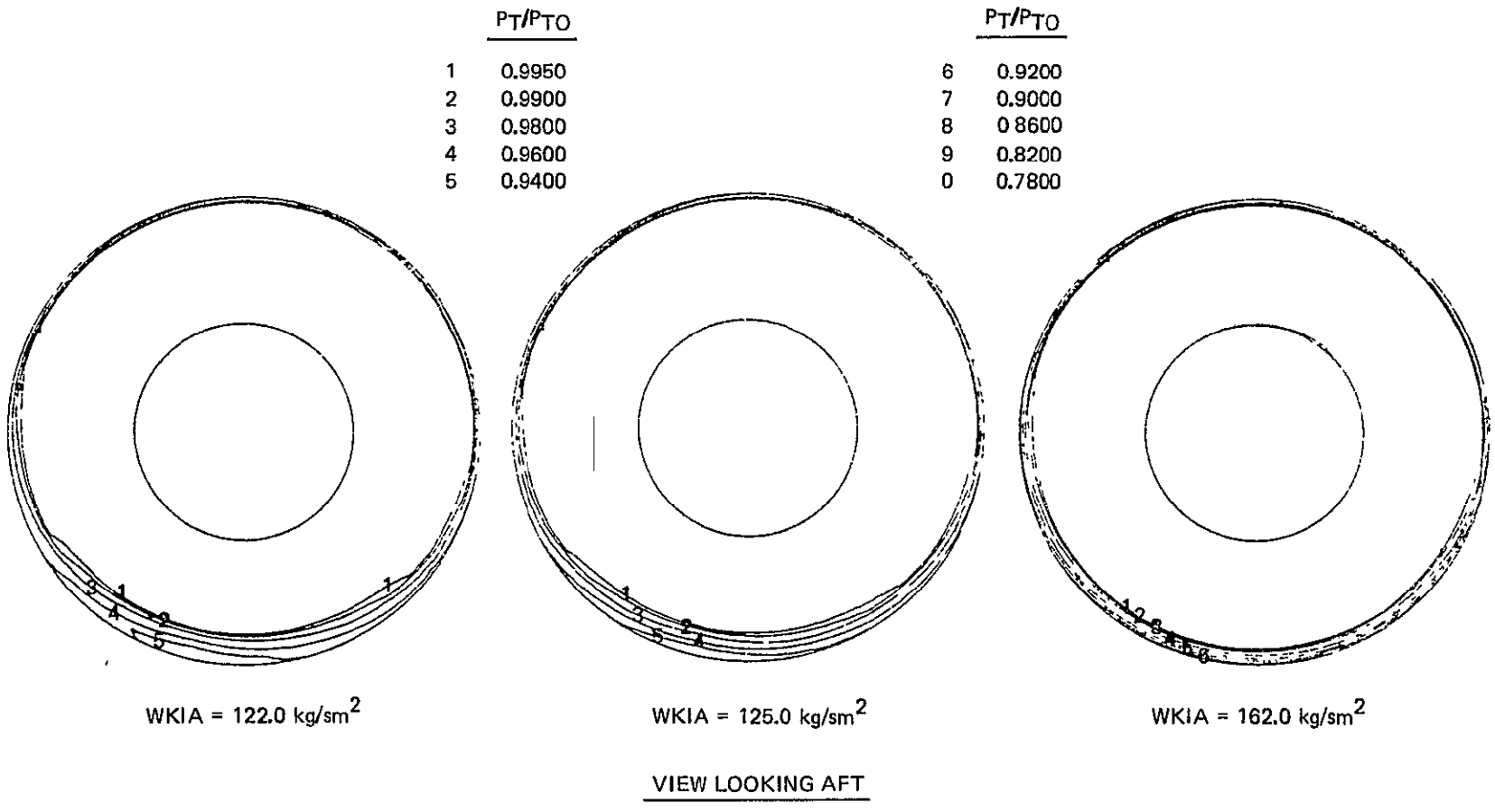

Figure 52. Fan Face Total Pressure Maps. V_o = 54 m/s, $\alpha = 75^o$

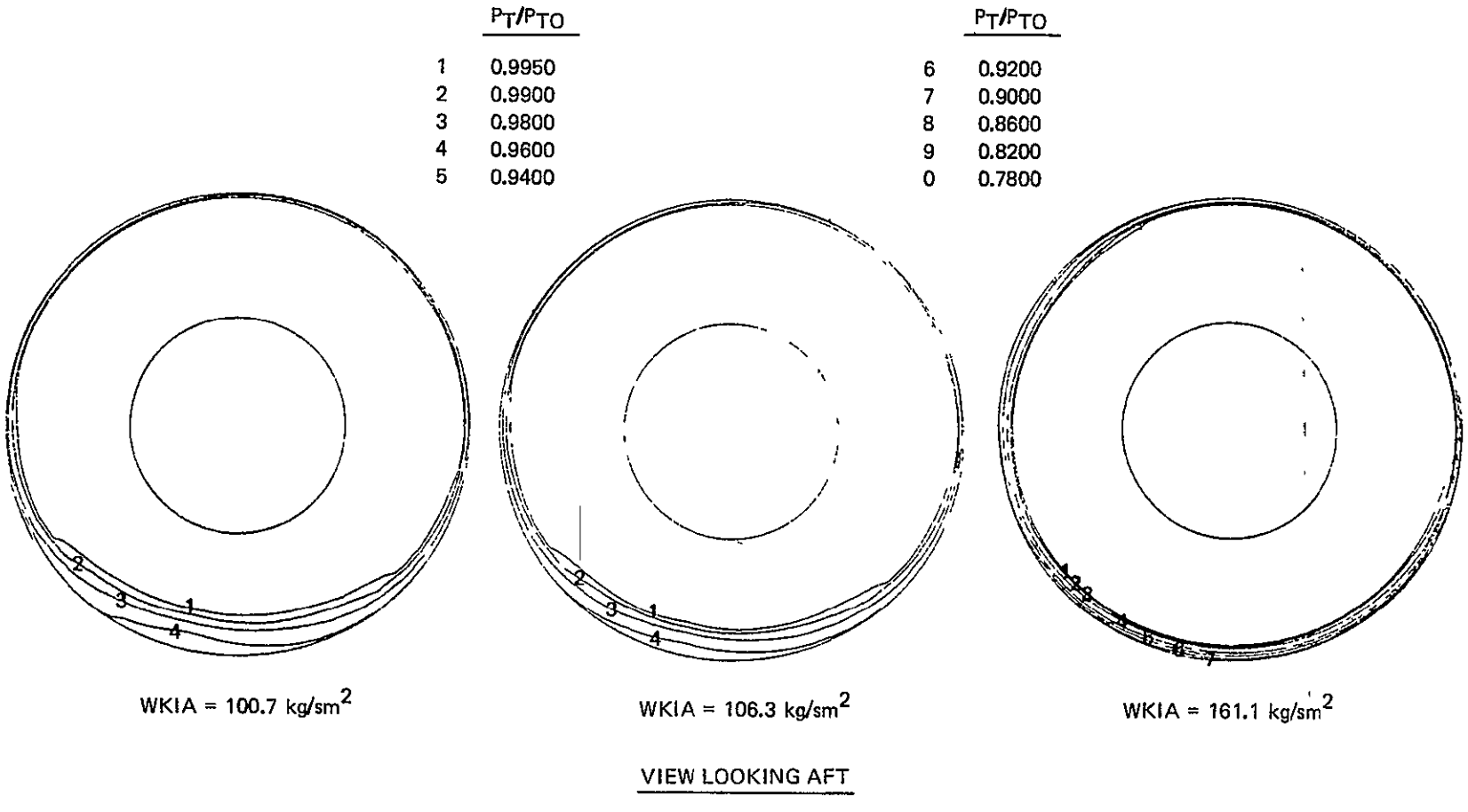

Figure 53. Fan Face Total Pressure Maps. V_o *= 39 m/s,* α *= 90°*

ORIGINAL PAGE IS
OF POOR QUALITY

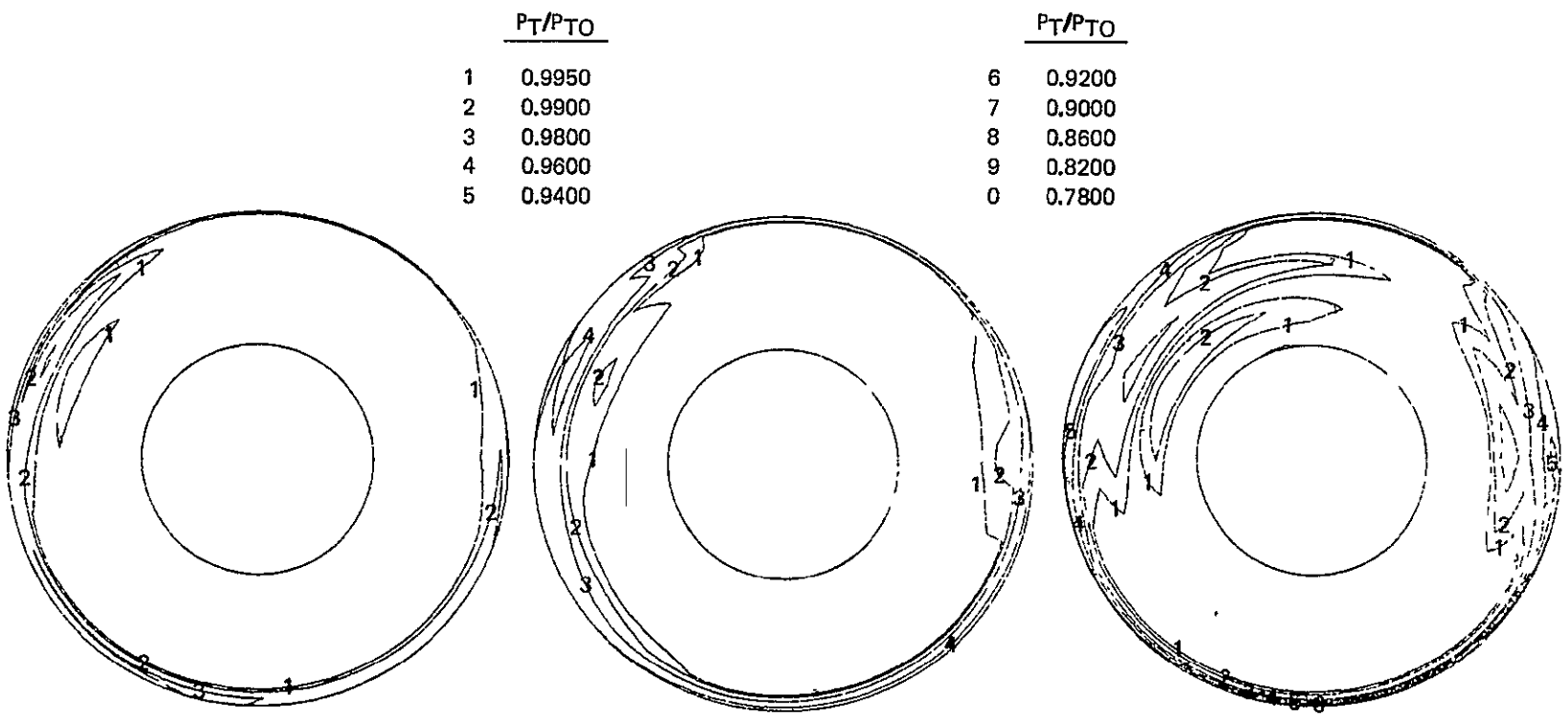

Figure 54. Fan Face Total Pressure Maps V_o *= 20 m/s,* α *= 120°*

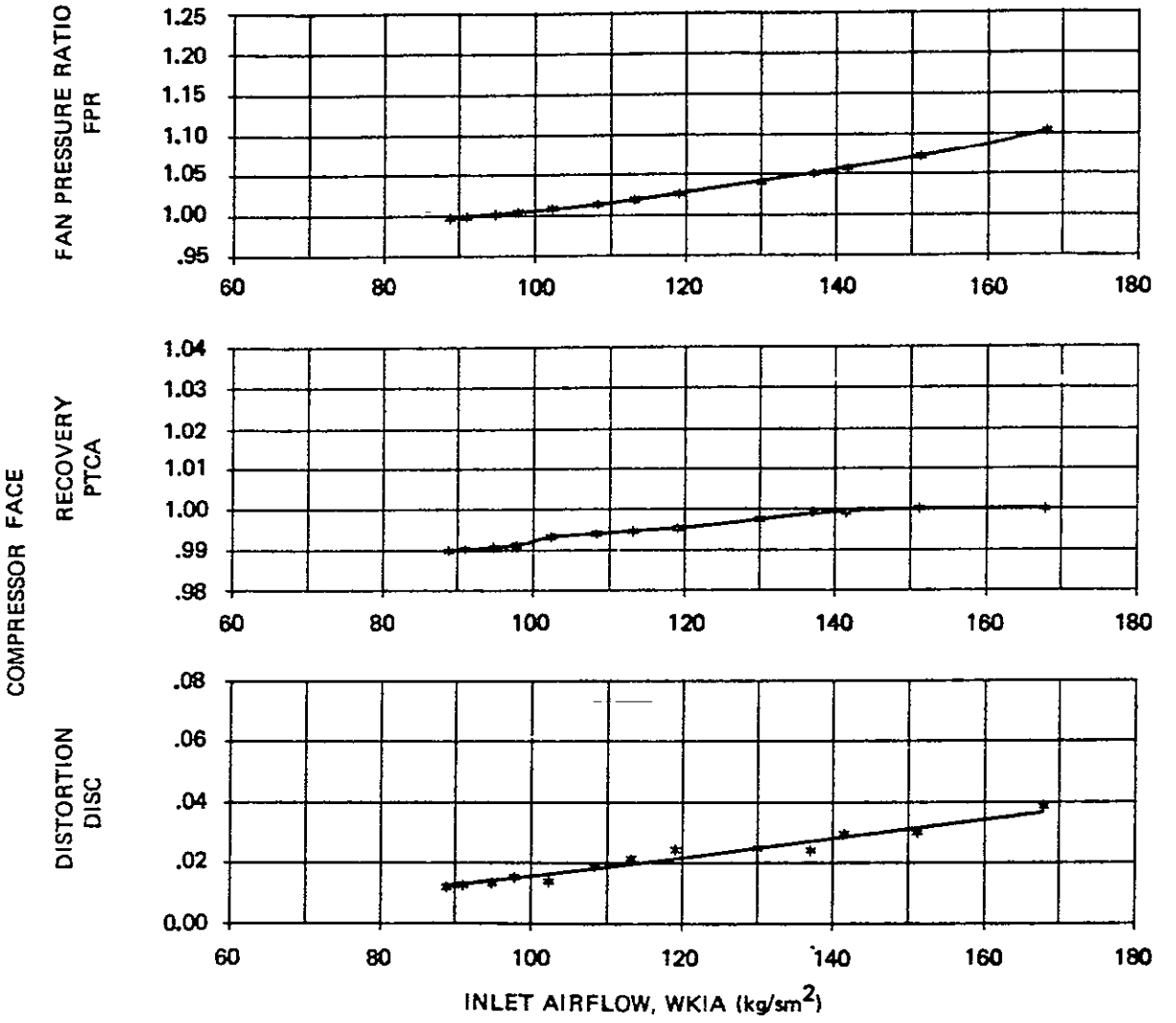

Figure 55. Engine Performance Characteristics, V_o = 72 m/s, $\alpha = 45^o$

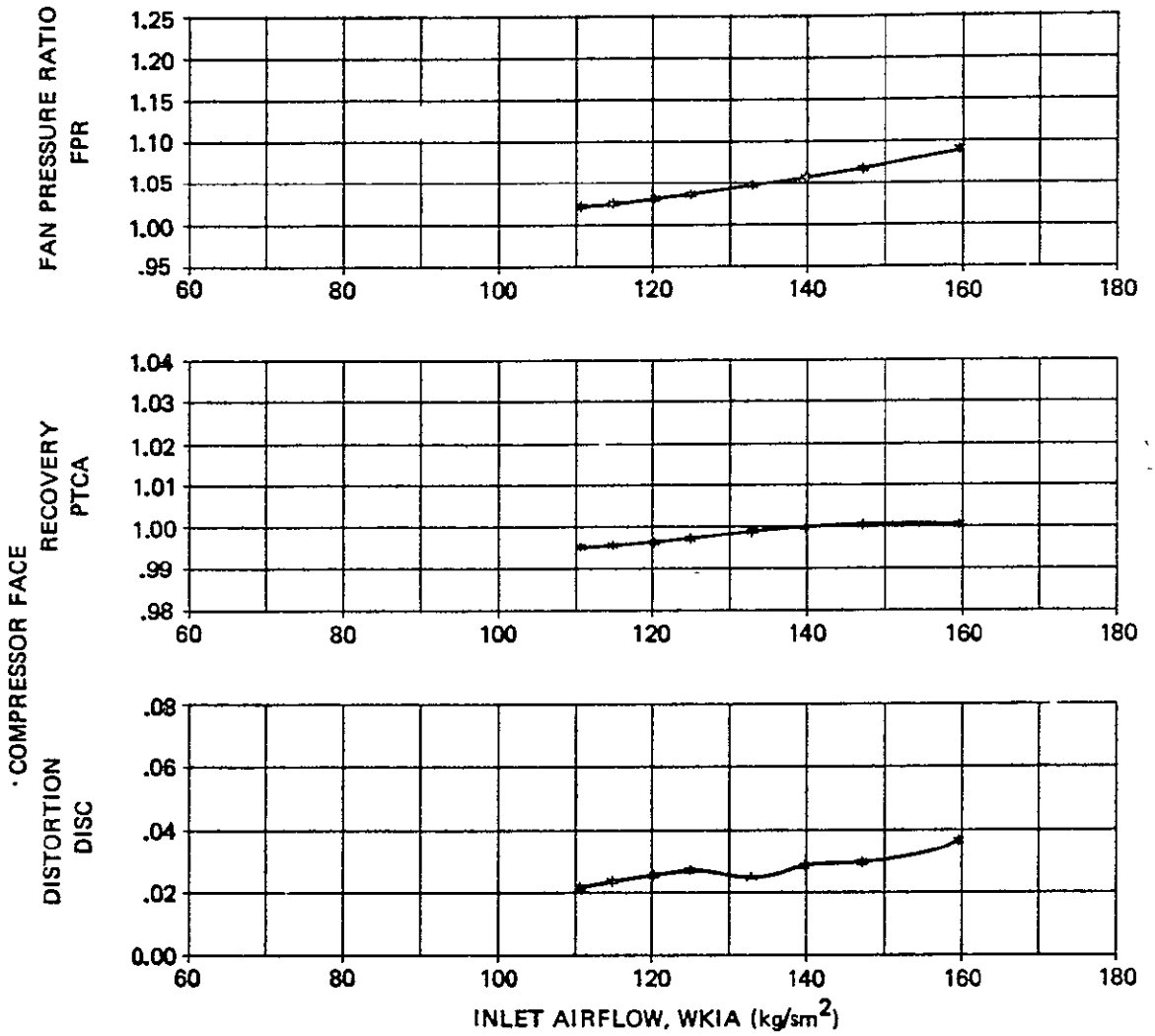

Figure 56. Engine Performance Characteristics, V_o = 64 m/s, $\alpha = 60^o$

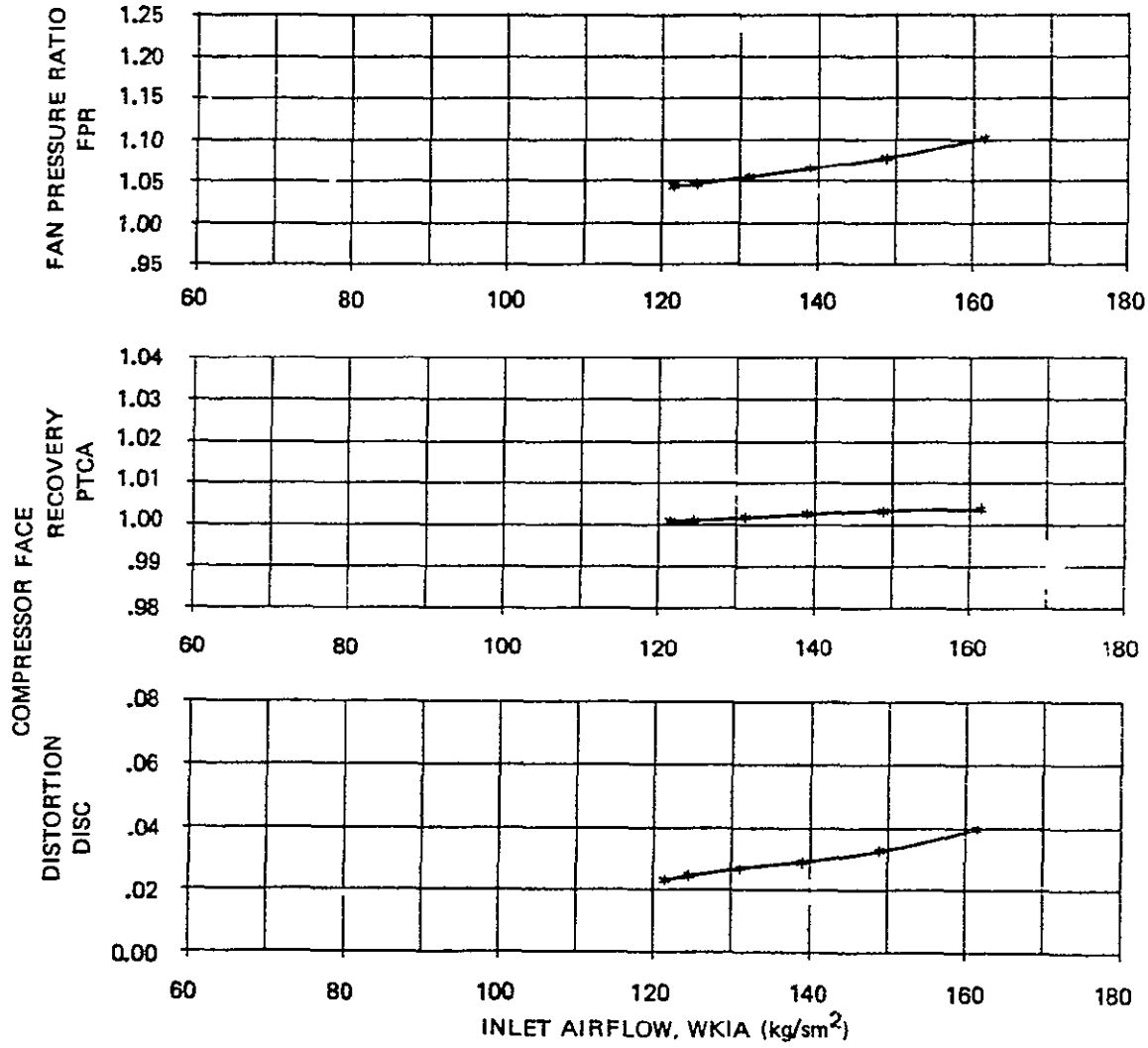

Figure 57. Engine Performance Characteristics, V_o = 54 m/s, $\alpha = 75^o$

ORIGINAL PAGE IS
OF POOR QUALITY

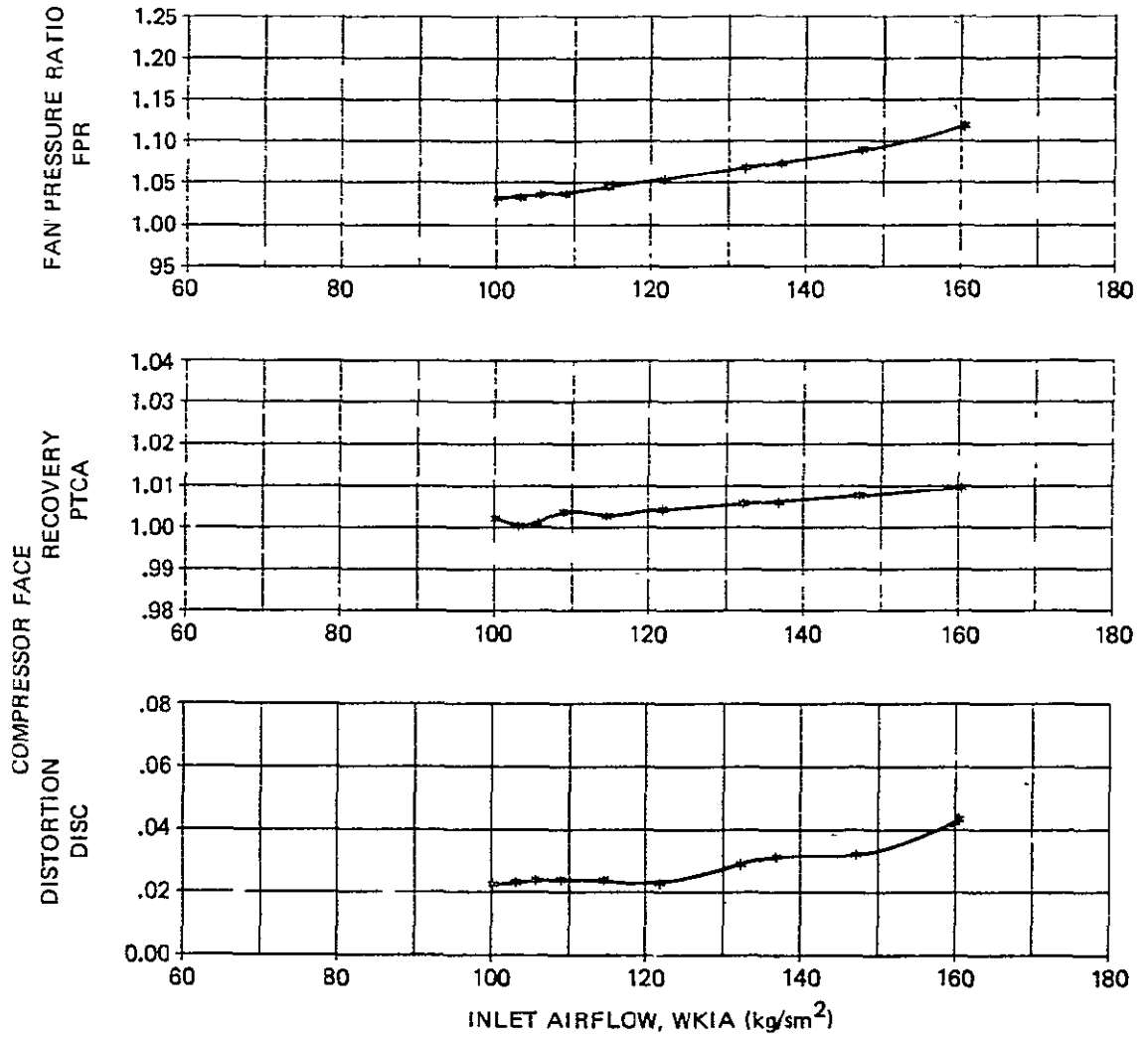

Figure 58. Engine Performance Characteristics, V_o = 39 m/s, $\alpha = 90^o$

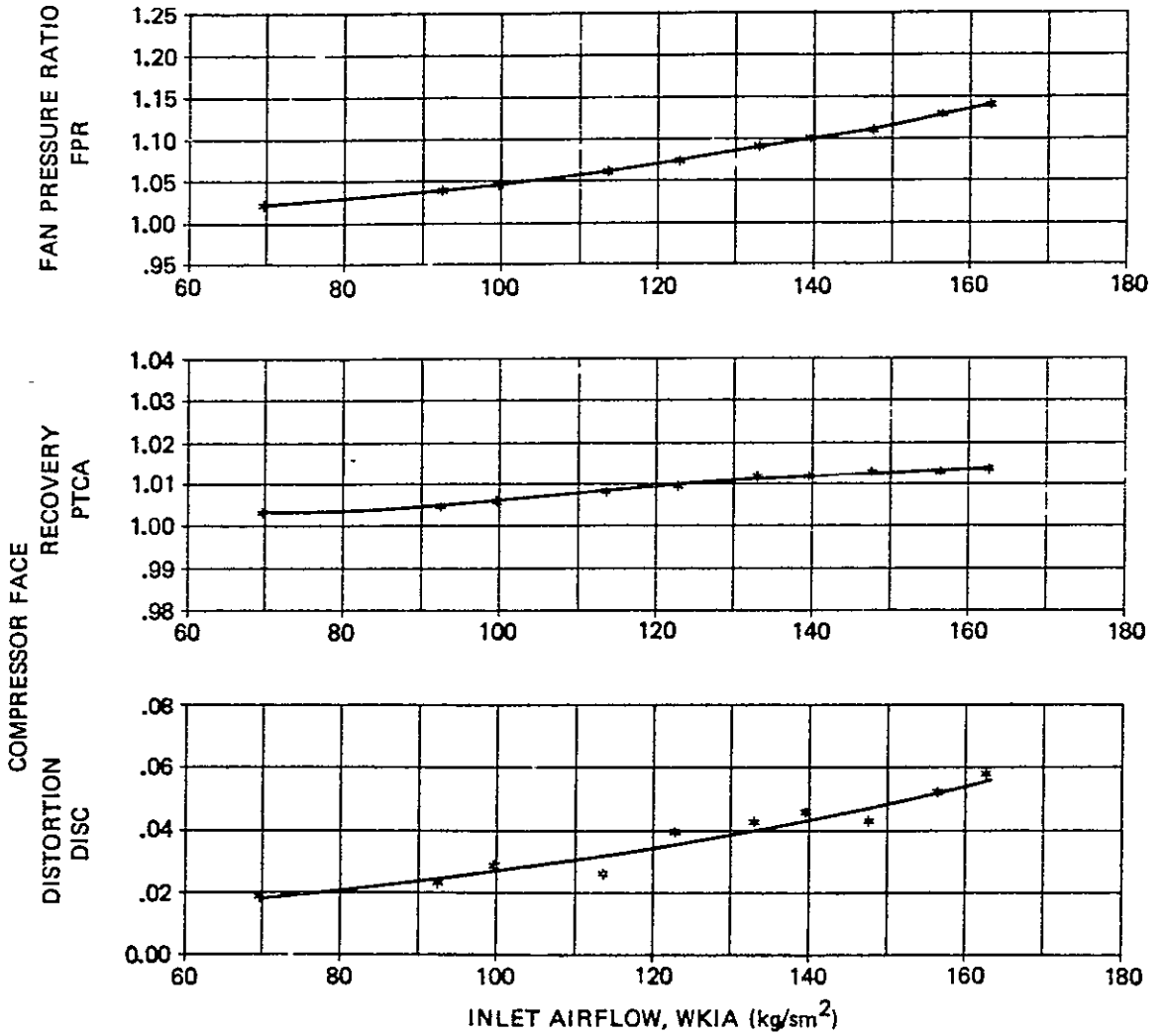

Figure 59. Engine Performance Characteristics, V_o = 20 m/s, $\alpha = 120^o$

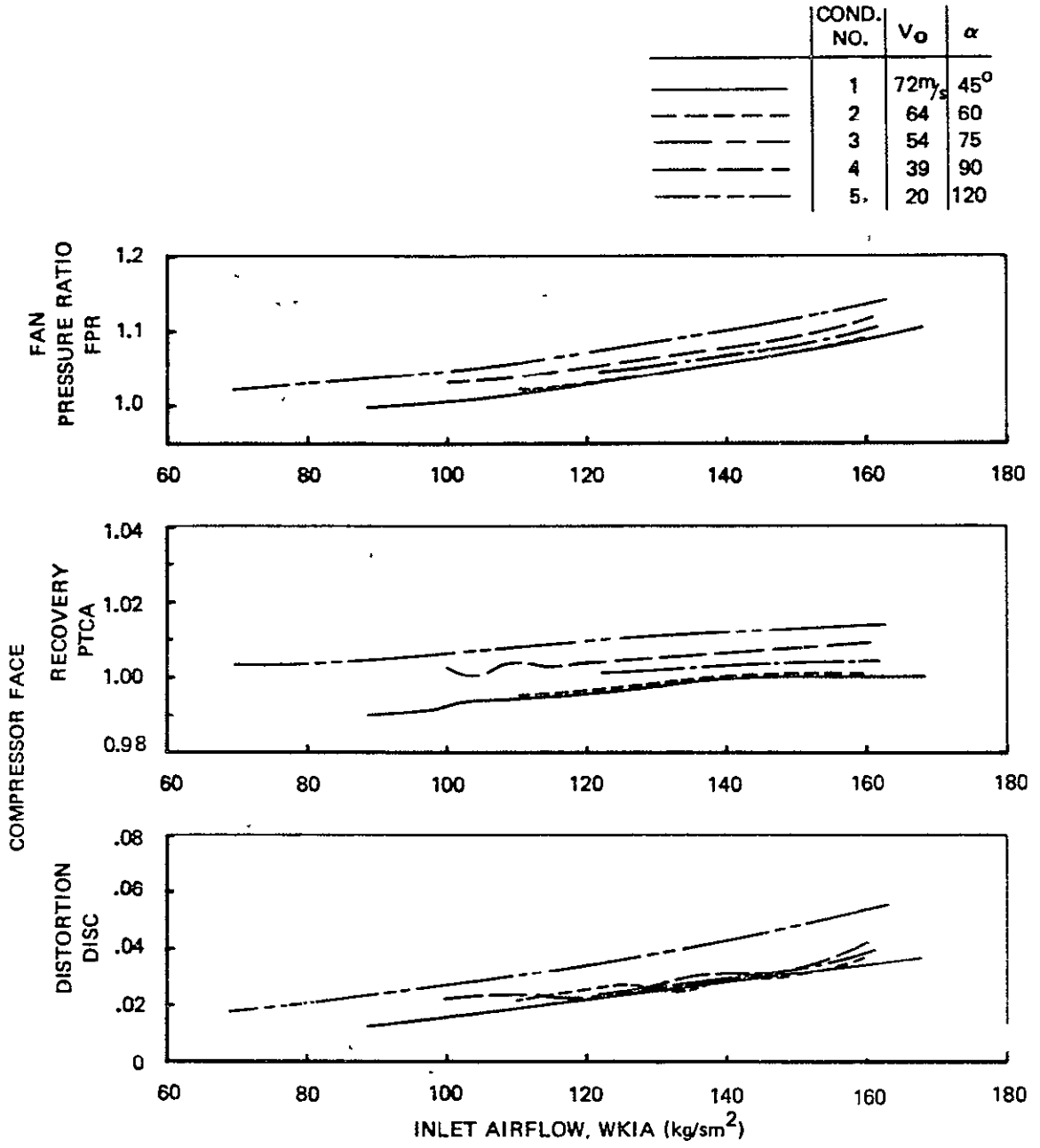

Figure 60. Engine Performance Characteristics At Design Conditions

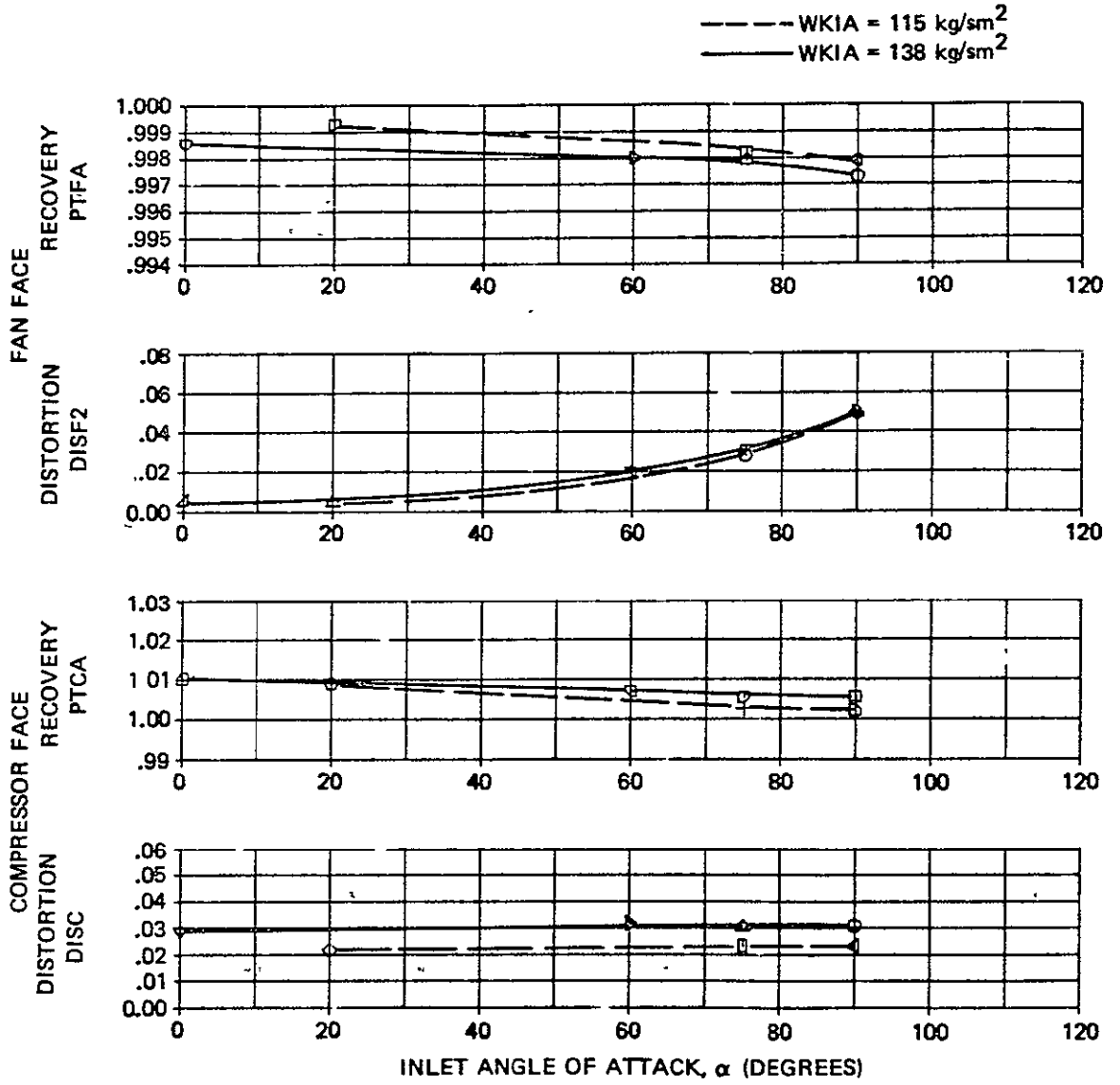

Figure 61. Effects of Angle of Attack on Inlet and Core Engine Performance V_o = 39 m/s

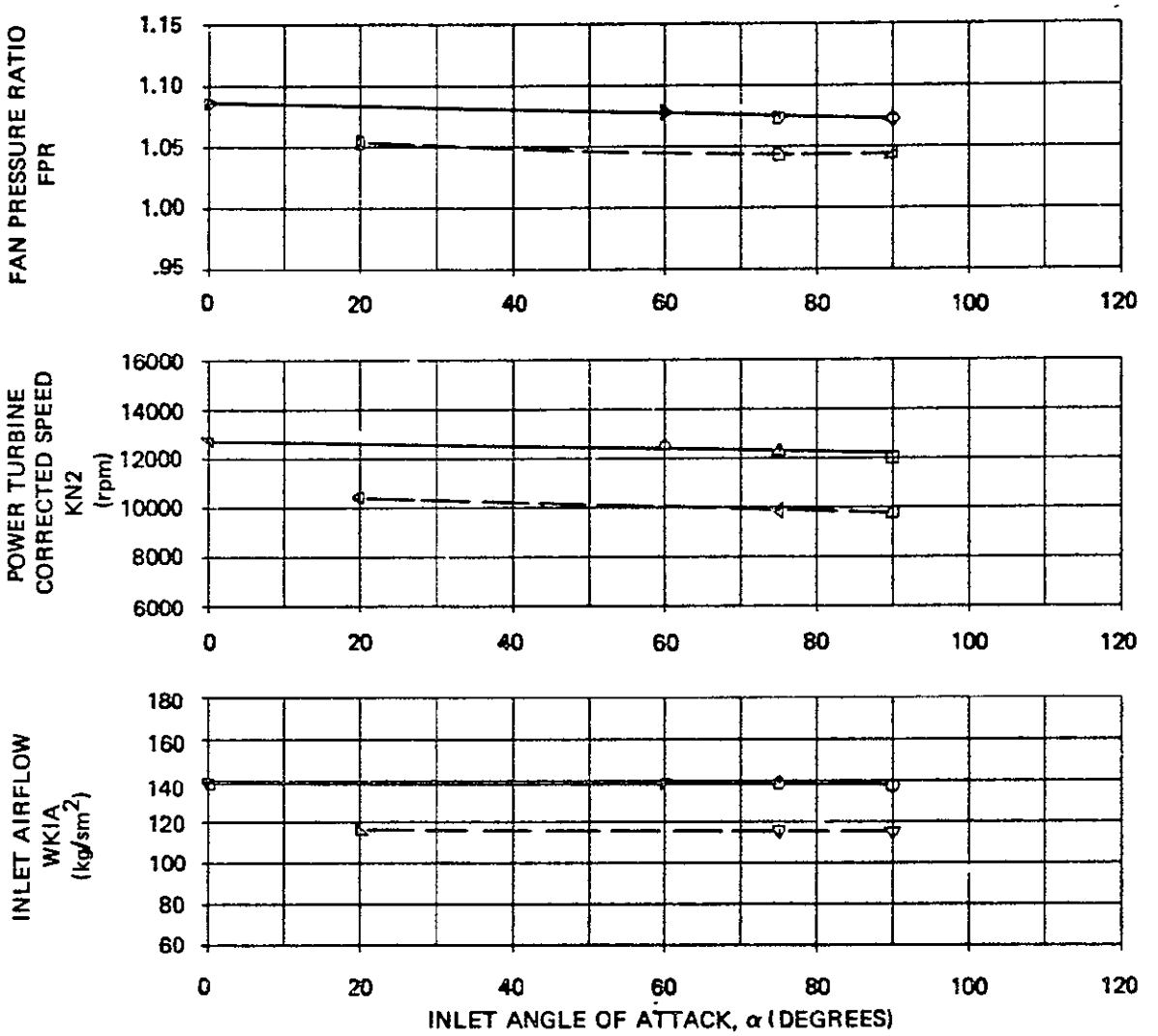

Figure 62. Effect of Angle of Attack on Fan Operation, V_o = 39 m/s

ORIGINAL PAGE IS
OF POOR QUALITY

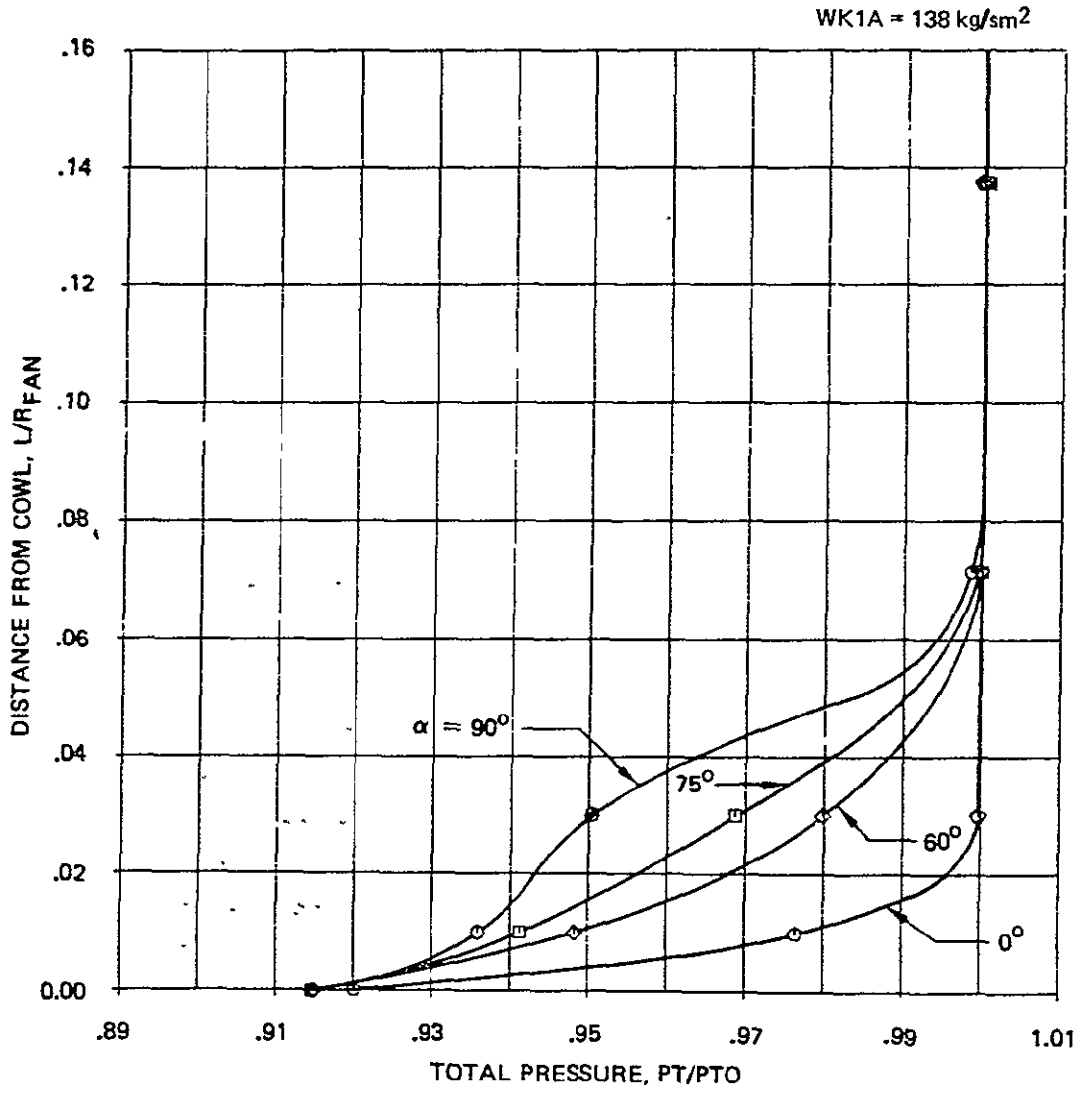

Figure 63. Effects of Angle of Attack on Windward Fan Face Rake Total Pressure Profile, V_o = 39 m/s

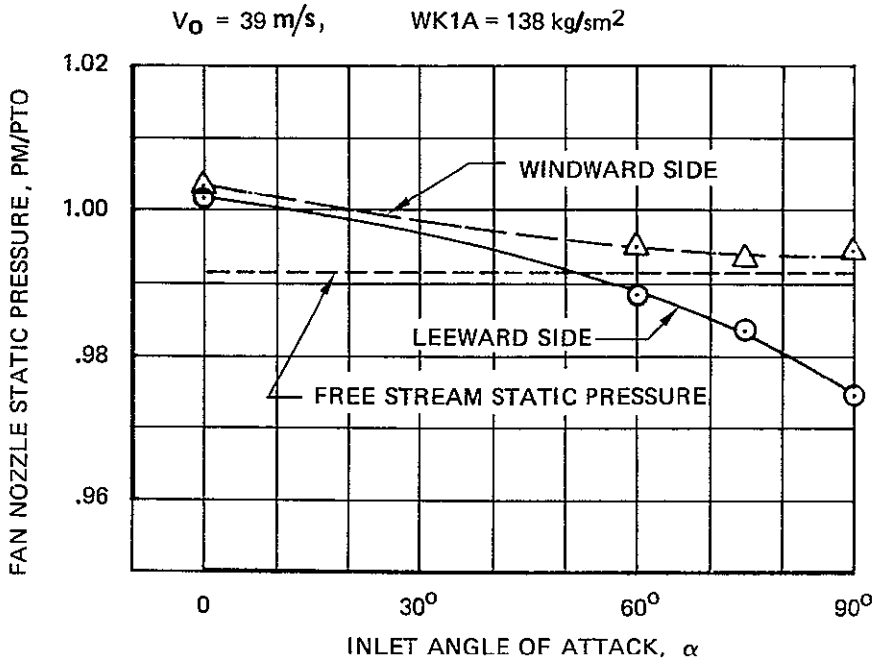

Figure 64. Fan Nozzle Static Pressure Versus Inlet Angle of Attack

ORIGINAL PAGE IS
OF POOR QUALITY

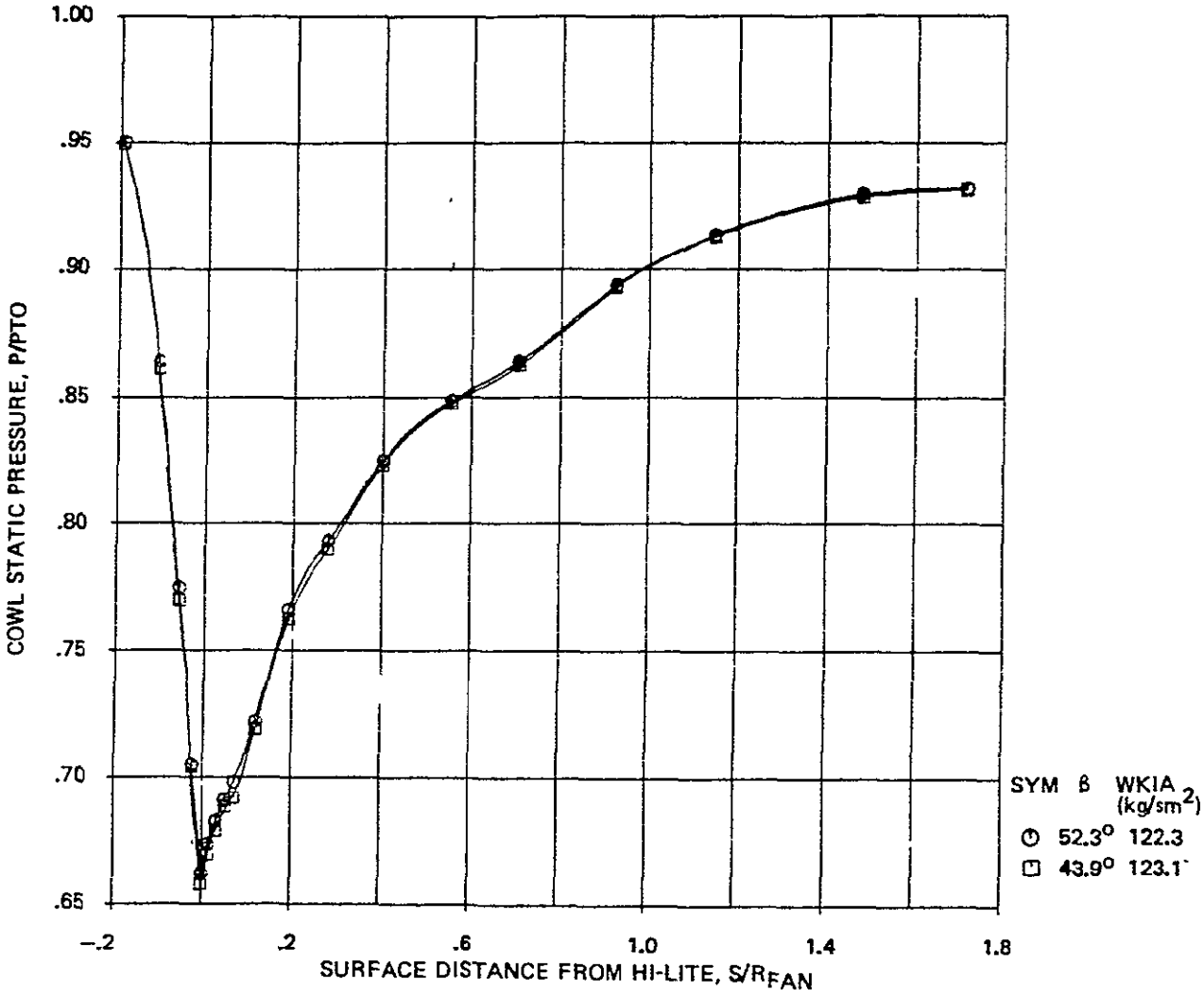

Figure 65. Windward Cowl Static Pressure Profiles with Different Fan Blade Angles, V_o = 39 m/s, $\alpha = 90^o$

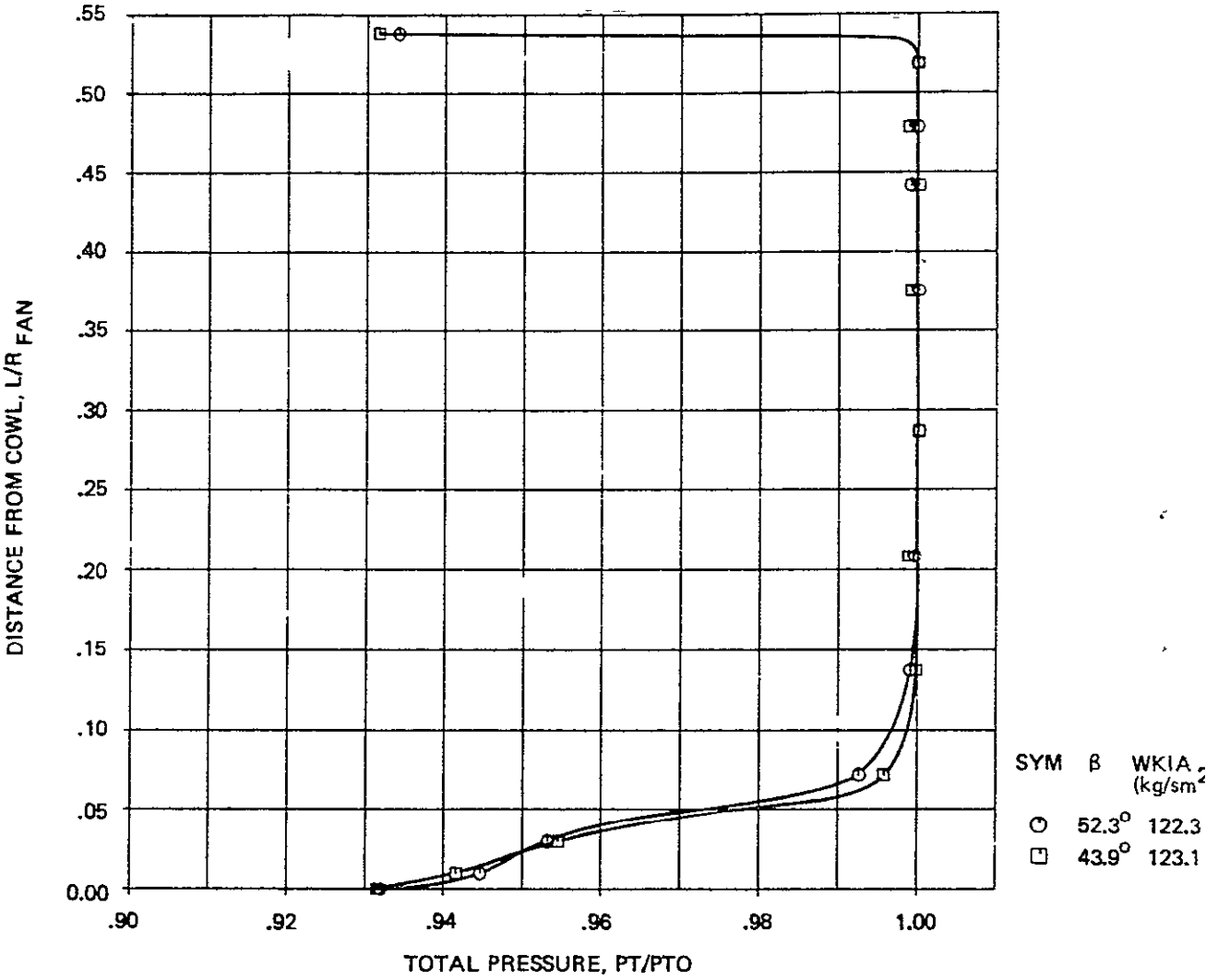

Figure 66. Windward Fan Face Rake Total Pressure Profiles With Different Fan Blade Angles V_o = 39 m/s, $\alpha = 90^o$

ORIGINAL PAGE IS
OF POOR QUALITY

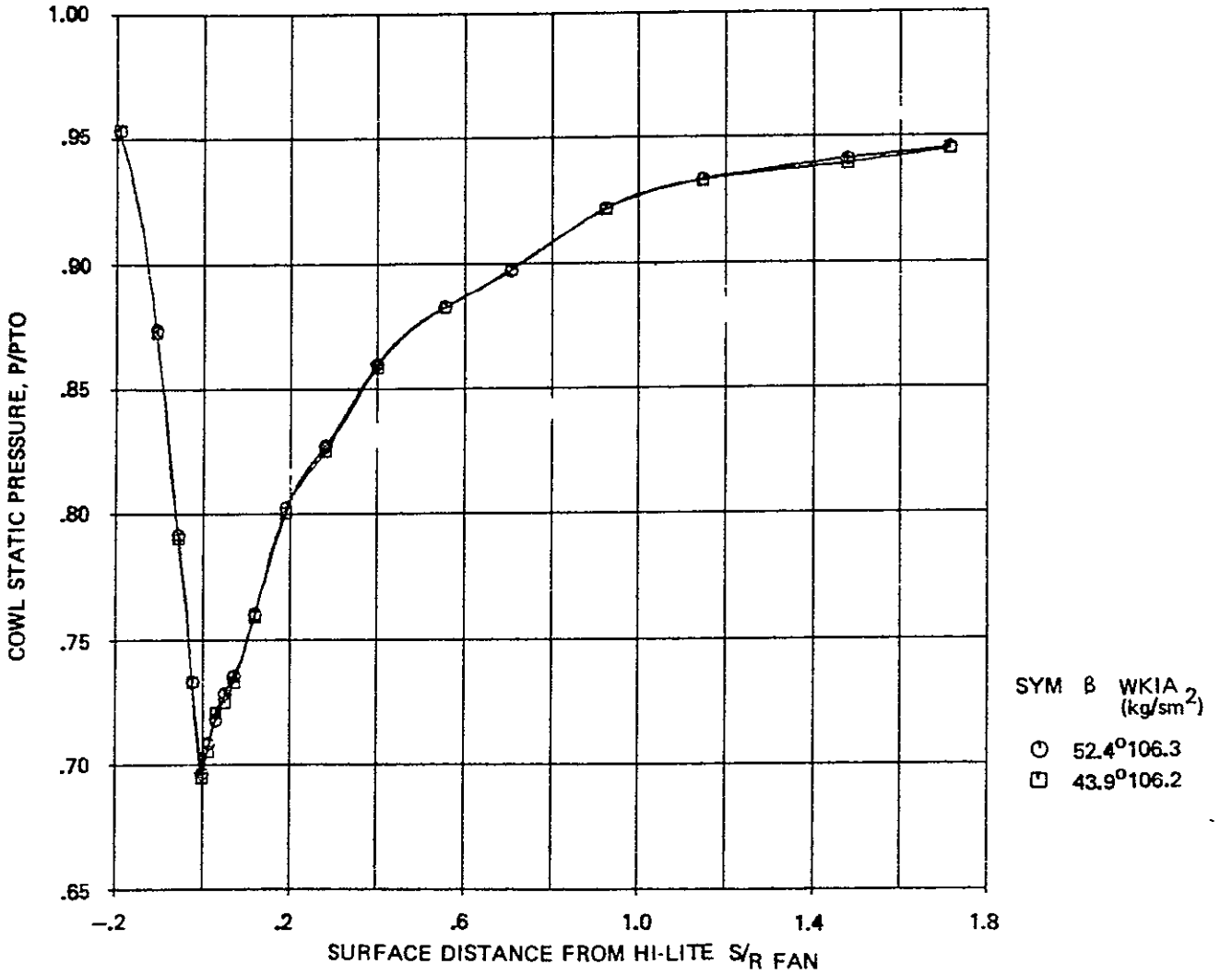

Figure 67. Windward Cowl Static Pressure Profiles Near On-set of Diffuser Separation With Different Fan Blade Angles. V_o *= 39 m/s,* $\alpha = 90^o$

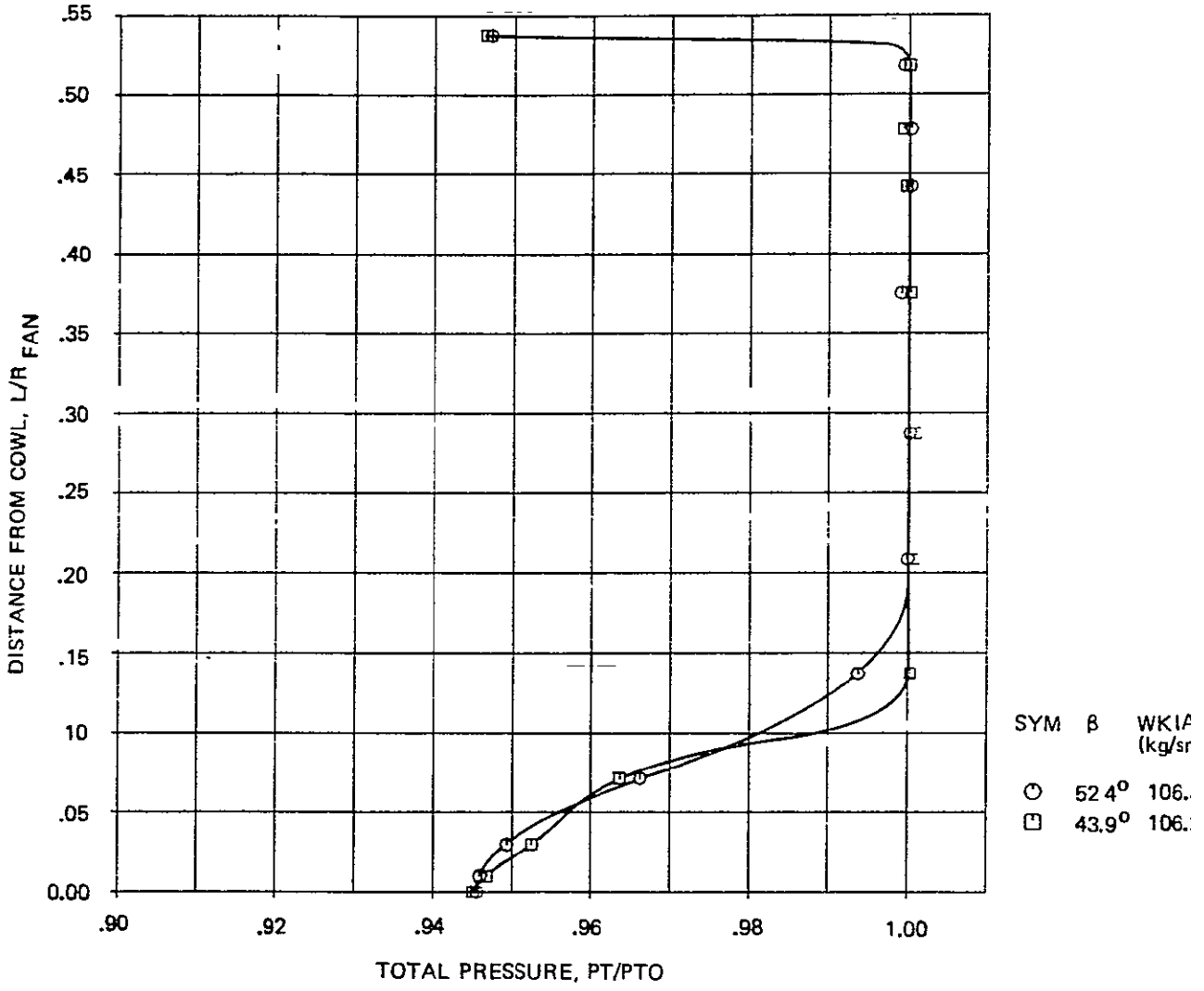

Figure 68. Windward Fan Face Rake Total Pressure Profiles Near On-Set of Diffuser Separation With Different Fan Blade Angles. V_o = 39 m/s, $\alpha = 90^o$

ORIGINAL PAGE IS
OF POOR QUALITY

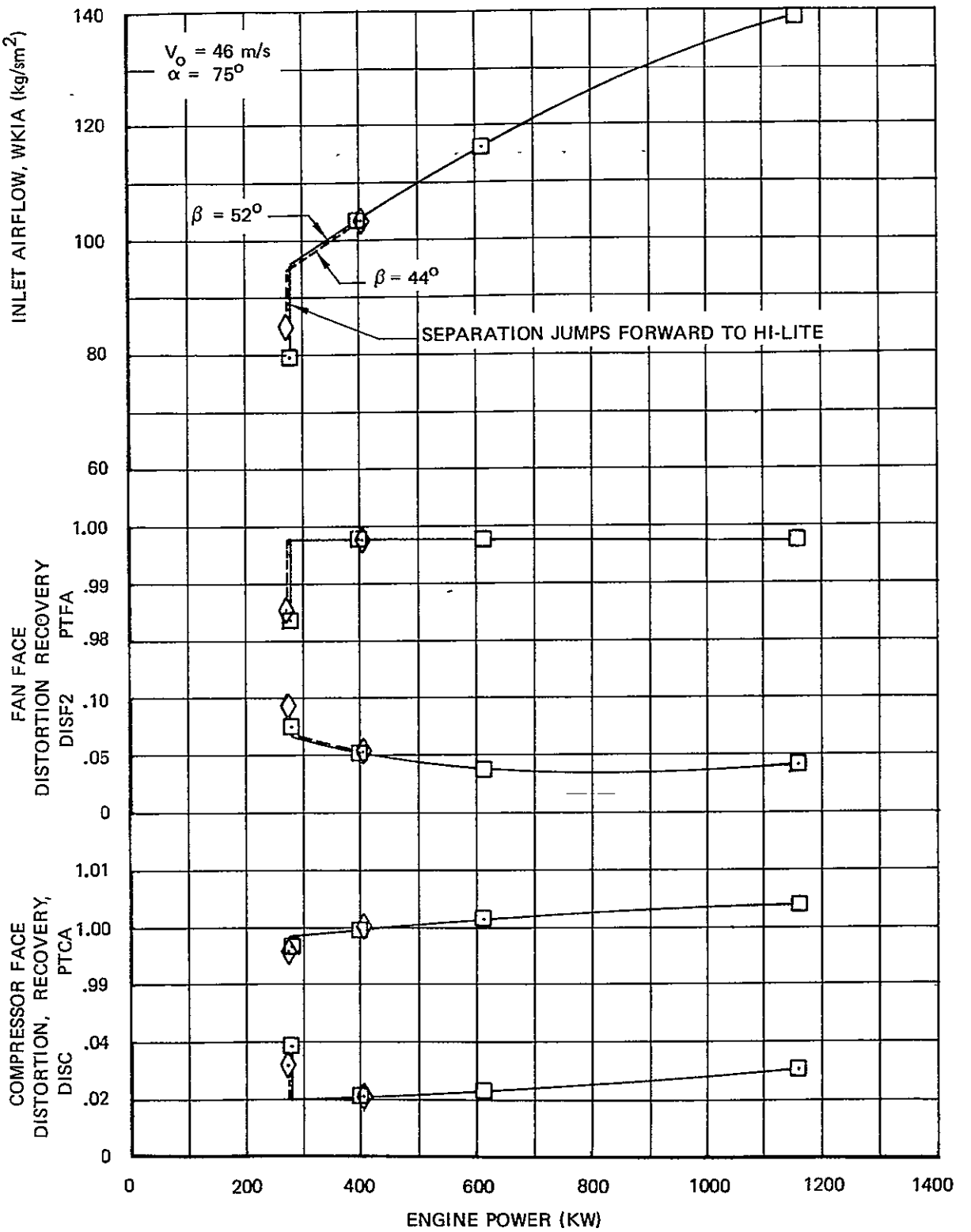

Figure 69. Lip Separation with Different Fan Blade Angles

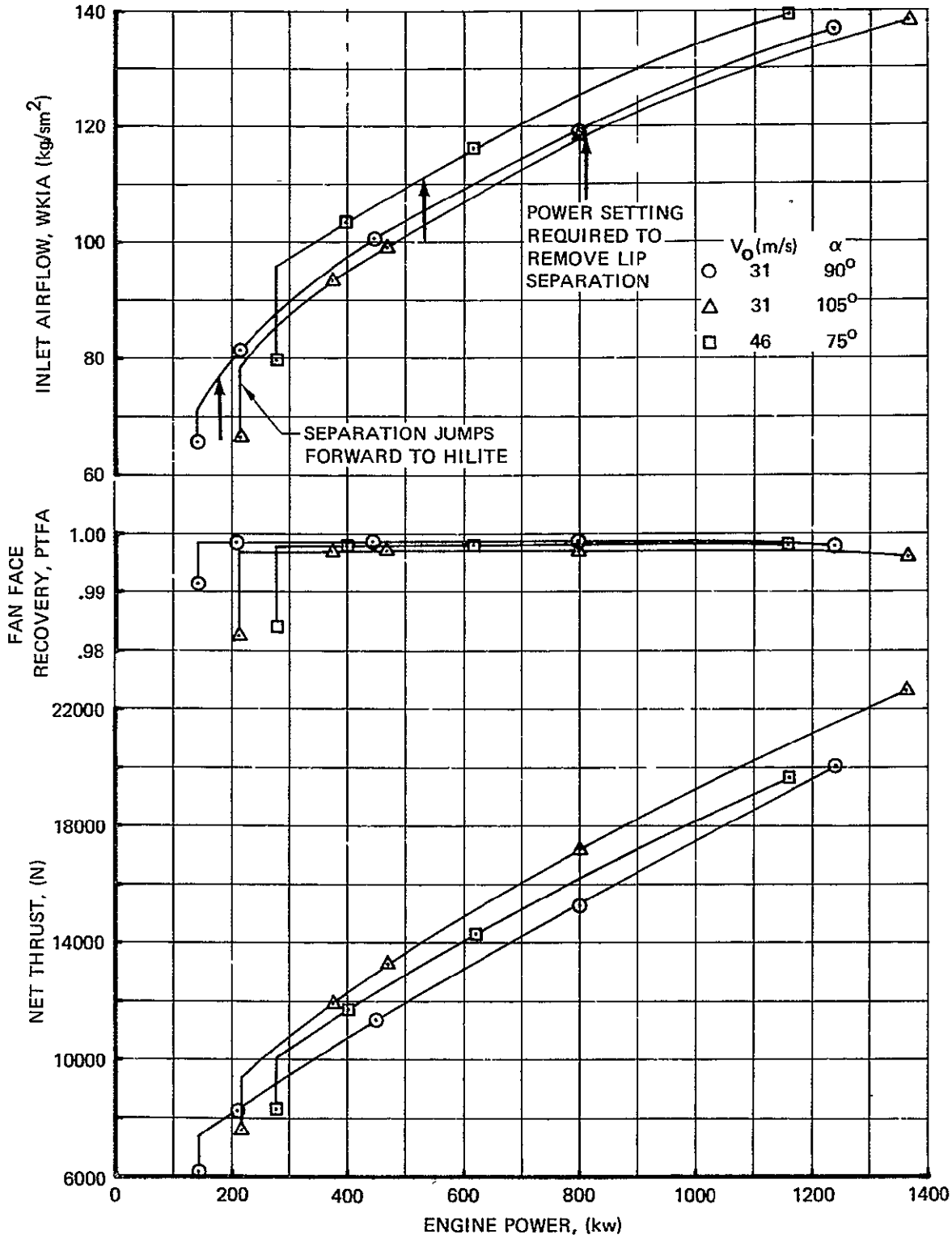

Figure 70. Effect of Lip Separation On Inlet Airflow And Nacelle Net Thrust

ORIGINAL PAGE IS
OF POOR QUALITY

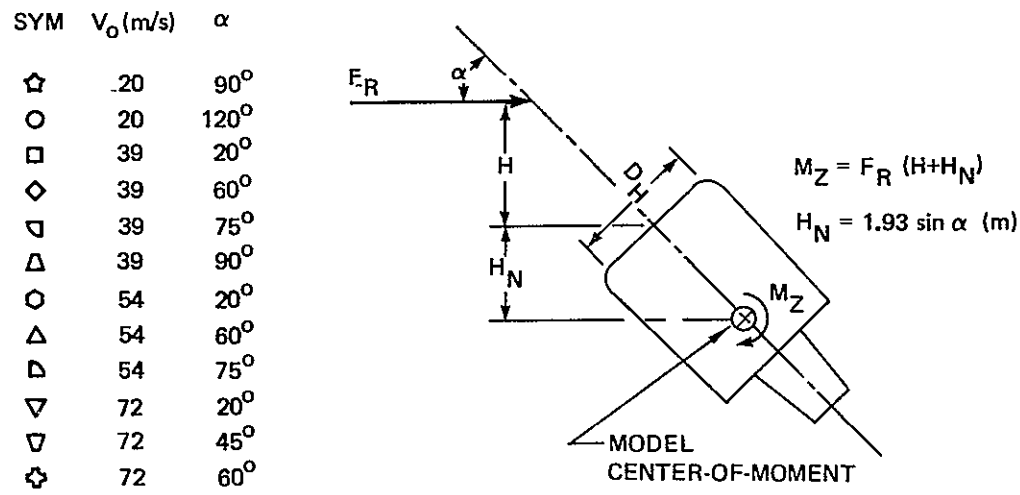

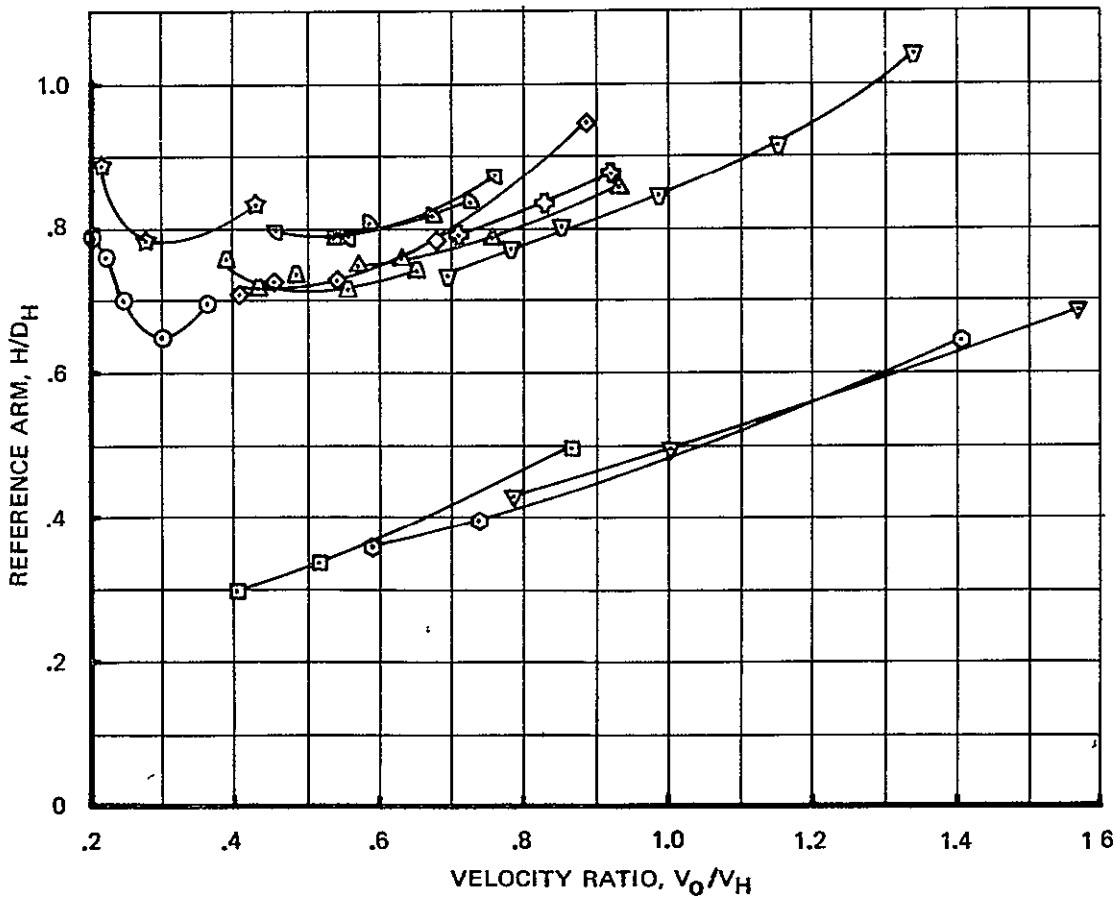

Figure 71. Nacelle Pitching Moment Using Test Model Center-of-Moment As Reference Center

SYM	V_o (m/s)	α
☆	20	90°
○	20	120°
□	39	20°
◇	39	60°
▽	39	75°
△	39	90°
○	54	20°
△	54	60°
▷	54	75°
▽	72	20°
▽	72	45°
✿	72	60°

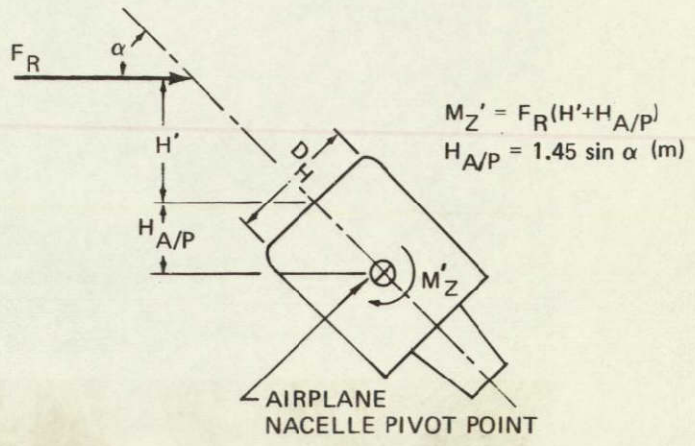

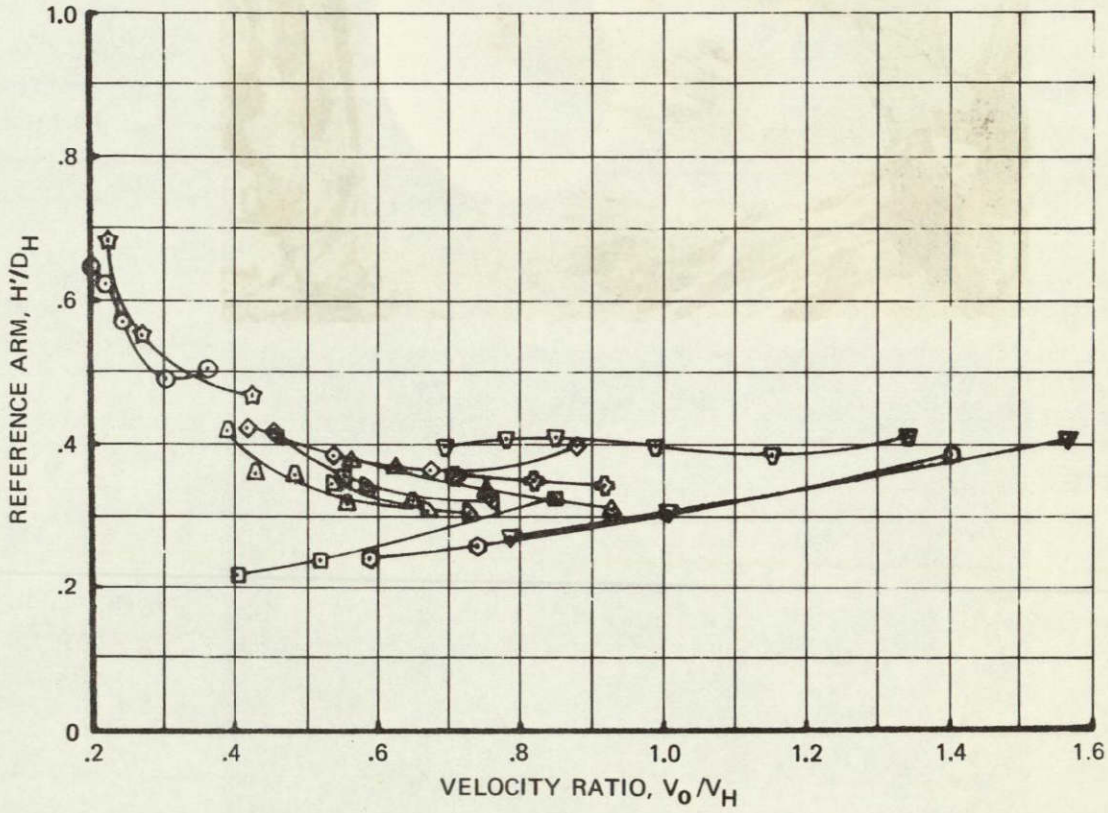

ORIGINAL PAGE IS
OF POOR QUALITY

Figure 72. Nacelle Pitching Moment Using Airplane Nacelle Pivot Point As Reference Center

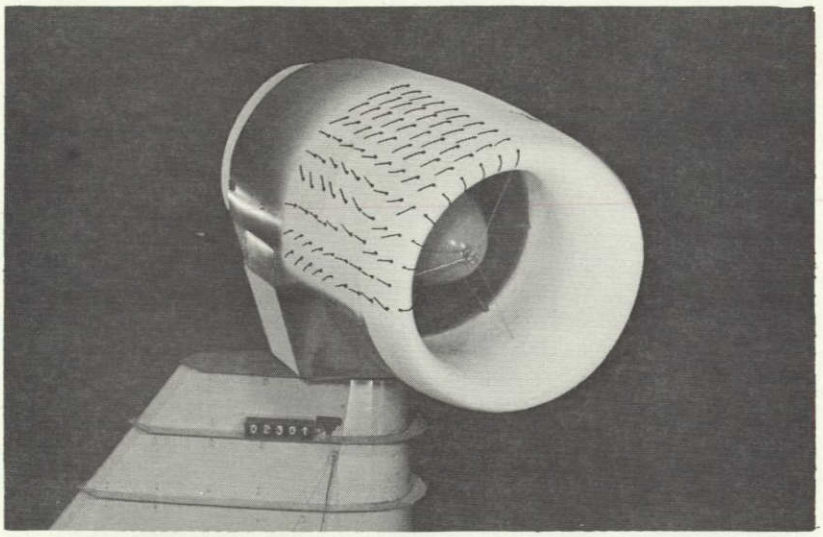

V_o/V_H = .330
F_R = 5550 N
F_S = 5216 N

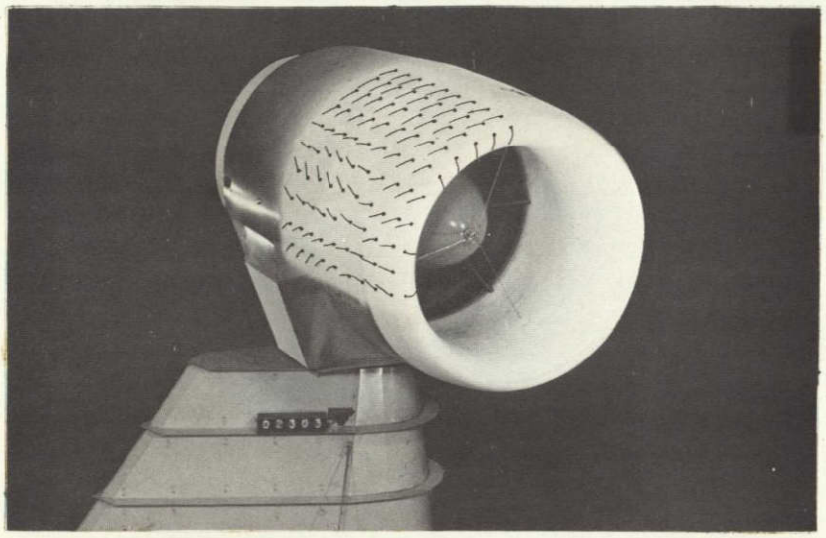

V_o/V_H = .482
F_R = 3844 N
F_S = 4491 N

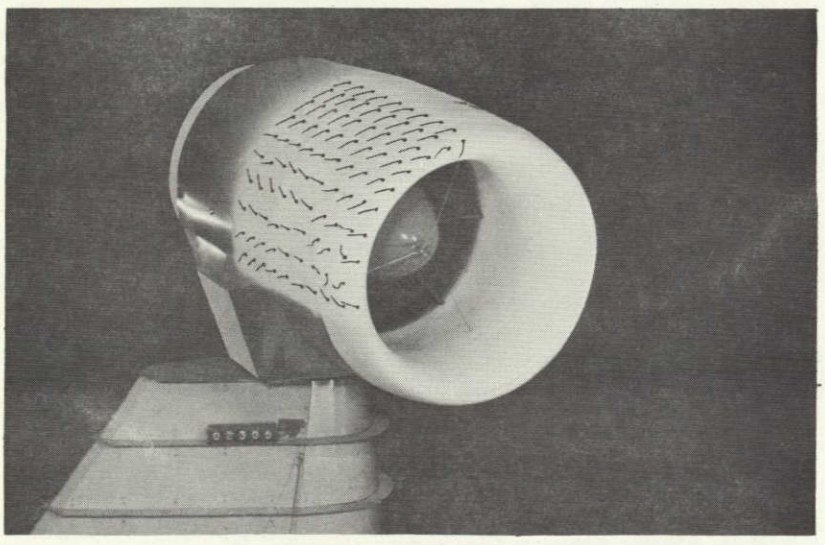

V_o/V_H = .718
F_R = 2615 N
F_S = 4566 N

V_o = 31 m/s
α = 75°

Figure 73. Photographs of Model During Angle-of-Attack Operation

ORIGINAL PAGE IS
OF POOR QUALITY

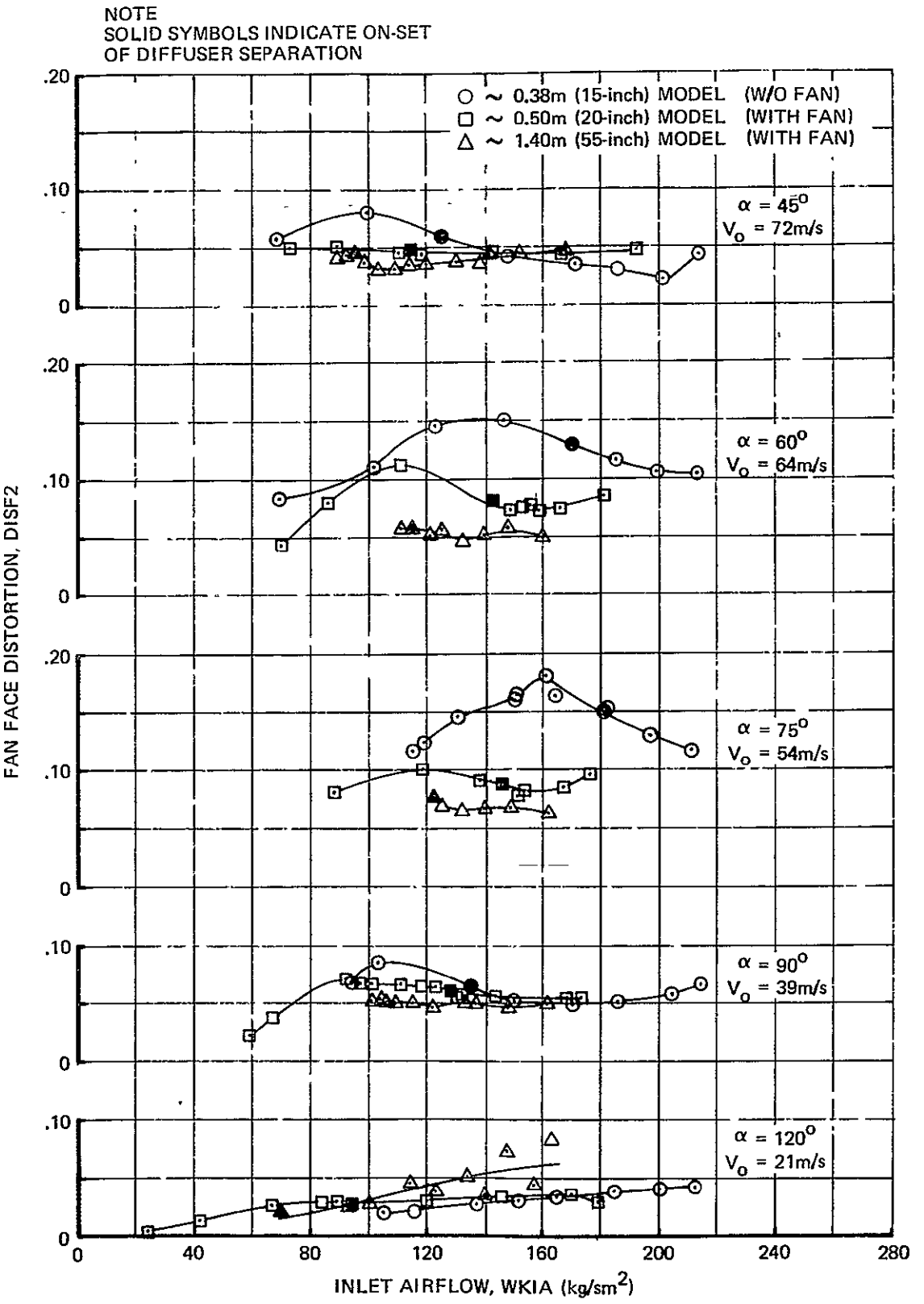

Figure 75. *Fan Face Distortion At Design Conditions For Three Different Scale Models of the LCF Inlet*

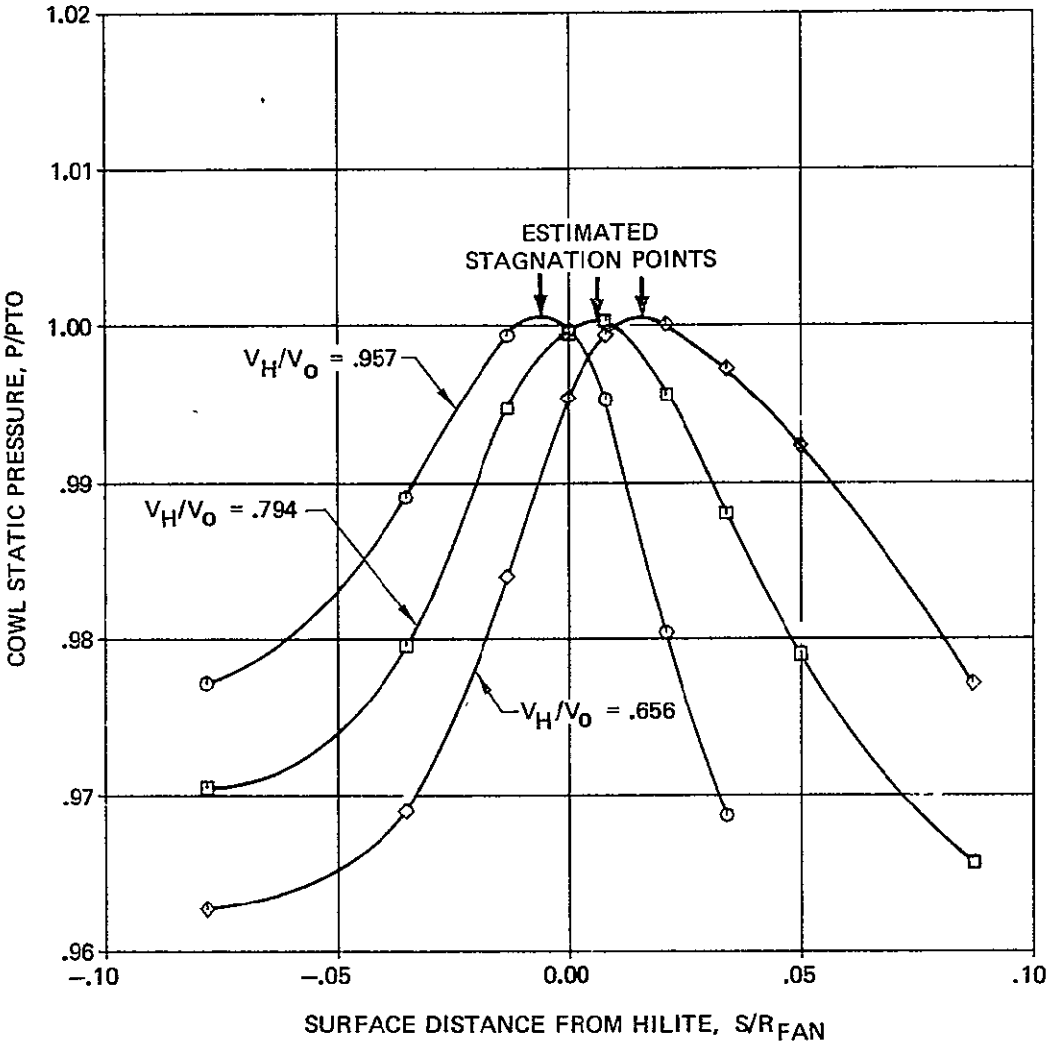

Figure 76. Static Pressure Distributions On Upper Cowl Lip V_o = 72 m/s, $\alpha = 0^o$

ORIGINAL PAGE IS
OF POOR QUALITY

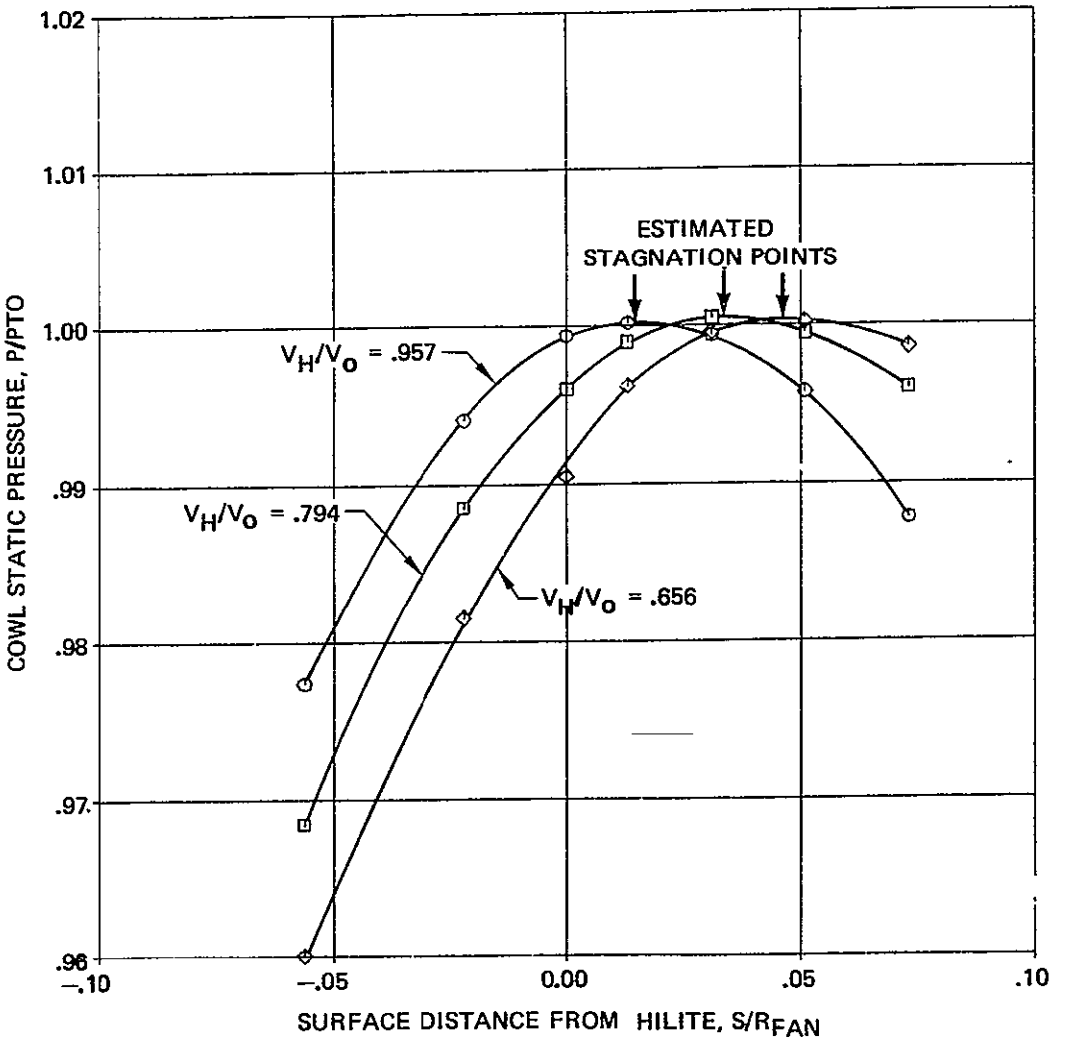

Figure 77. Static Pressure Distributions on Lower Cowl Lip. V_o = 72 m/s, $\alpha = 0^o$

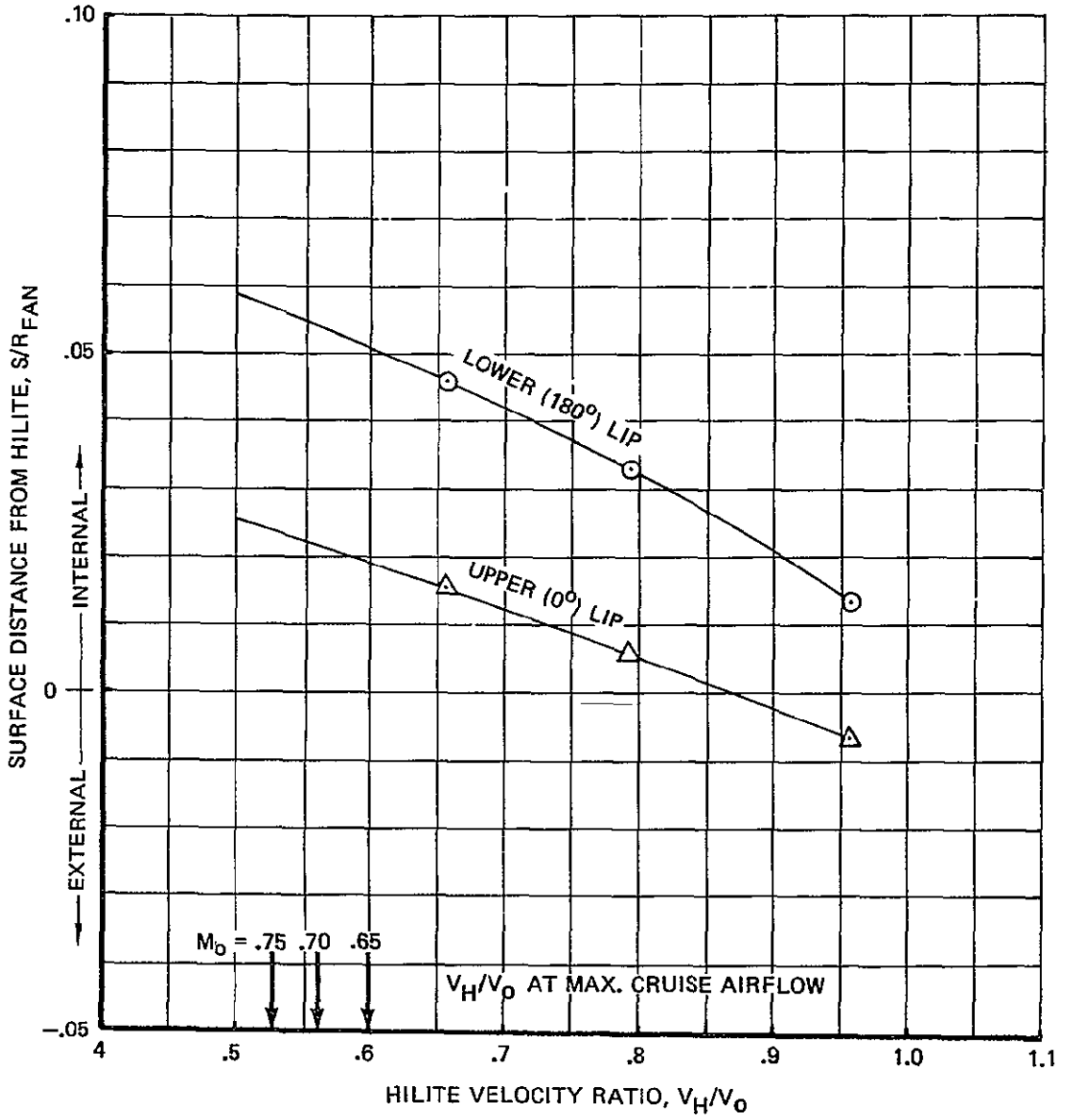

Figure 78. Stagnation Points On Upper and Lower Cowl Lip at 0° Angle of Attack

ORIGINAL PAGE IS
OF POOR QUALITY

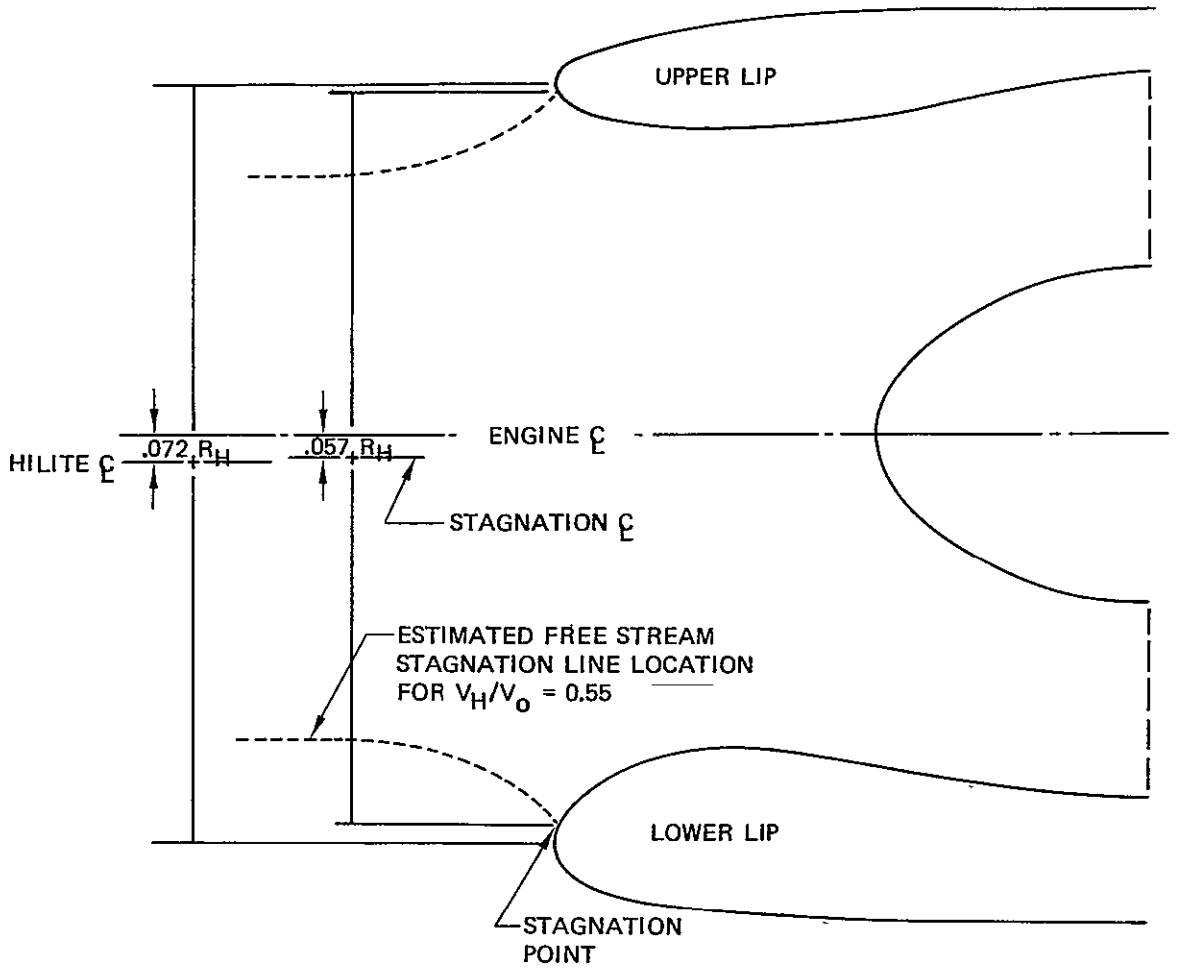

Figure 79. Off-set of Stagnation Plane From Engine Centerline at 0^o Angle of Attack